Modeling and Evaluation of New Collimator Geometries in SPECT

Modellering en evaluatie van nieuwe collimatorgeometrieën in SPECT

Lara da Rocha Vaz Pato

Promotoren: prof. dr. S. Vandenberghe, prof. dr. R. Van Holen
Proefschrift ingediend tot het behalen van de graad van
Doctor in de ingenieurswetenschappen: biomedische ingenieurstechnieken

Vakgroep Elektronica en Informatiesystemen
Voorzitter: prof. dr. ir. R. Van de Walle
Faculteit Ingenieurswetenschappen en Architectuur
Academiejaar 2015 - 2016

UNIVERSITEIT
GENT

ISBN 978-90-8578-922-2
NUR 954
Wettelijk depot: D/2016/10.500/54

Department of Electronics and Information Systems
Faculty of Engineering and Architecture
Ghent University

MEDISIP
IBiTech - iMinds
Campus UZ
De Pintelaan 185, Ingang 36 (Blok B)
9000 Ghent
Belgium

Promotors:
Prof. dr. Roel Van Holen
Prof. dr. Stefaan Vandenberghe

Board of examiners:
Prof. dr. Gert De Cooman, Ghent University, chairman
Prof. dr. Bart Goossens, Ghent University, secretary
Prof. dr. Yves D'Asseler, Ghent University
Prof. dr. Greta Seng Peng Mok, University of Macau, China
Dr. Kathleen Vunckx, KU Leuven, Belgium
Dr. Karel Deprez, Molecubes, Ghent, Belgium

This work was funded by a PhD Fellowship from the Research Foundation Flanders (FWO).

Acknowledgements

OK, let's face it, doing a PhD is not all rainbows and butterflies. You are working on a very specific subject for several years, and most of the things you do will fail, over and over again, and you just have to deal with it. You have to persevere, find out where the problems are, try different things... Until something finally works! And then you advance human knowledge. Just a tiny bit, but it's something, and it has your name on top of it! And that's why we do it.

Often times I found myself wondering what I was doing, why I was doing it, and if there was anyone in the world who cared... Well, some people cared, and it is to those that I want to send a huge thank you from the core of my being!

First of all I thank my supervisors, **Roel** and **Stefaan**, without whom none of this would have been possible. They gave me the chance to work on something that I had never studied before (coming from pure physics), the tools to learn new skills, and the freedom to choose my own path of research. My experience at the MEDISIP research group has been incredibly diverse and valuable, and opened a lot of doors in my future, and for that I am very grateful. Whenever I knocked on **Roel**'s door with a question, he would find some time to help me, never losing his patience and often giving me fresh ideas to work on. His guidance was the biggest factor in the successful conclusion of my PhD. **Stefaan** was also available whenever I needed, and always gave an interesting perspective to my work. This also helped me a lot in my research, and especially in improving my papers before submission.

Secondly, I need to thank my fellow slav... *ahem*, I mean colleagues, from MEDISIP. I always felt at home in their wonderful nerdiness! I will SO miss our lunch-time discussions about life, the Universe, international politics, artificial intelligence, and how to accomplish the perfect murder... The first person I need to thank is **Bert**, who, on top of being an excellent, versatile researcher is an amazing teacher and mentor (I always envied how successful his master thesis students were!). In the first 2 years of my PhD he helped me tremendously in understanding the reconstruction code he developed, as well as many other computer-related things (in which I am embarrassingly ignorant)... This made a huge difference in how fast I advanced in my PhD, and I really appreciate all the patience he had with my often basic questions interrupting his work. Next I need to thank **Karel**, with whom I had the pleasure to collaborate on a paper. It was very easy to work with him and I learned a lot. He always gave me interesting and very relevant comments about my work, and I am grateful that he accepted to be part of my PhD jury. **Karen** was also a great support throughout my PhD, both with my research and on a personal level. Her advice was always well thought out and her attitude an inspiration to me (I wish I'll have her courage one day!). **Tiziana** was not very long at MEDISIP, but her impact on me was quite profound. Her hard work and perseverance through difficult situations made me look at life differently, and I really identified with her as a person. It was also her work that strengthened my second paper and got it so easily accepted. **Radek** is probably the person who understands me the most in the group, having started his PhD at about the same time as me. We had a lot of laughs together. **Carmen**, who I admire for having the most diverse hobbies of anyone I know, has also been there for most of my PhD. She was a great companion not only at work but in traveling, partying... **Faruk** was a huge time-saver in my PhD: he guided me in GATE, and sent me lots of his own code to help me automate many tasks. But most importantly, he was a great friend, always willing to go out of his way to help someone. **Nathalie**, fearless and adventurous, kept the team spirit alive at MEDISIP, by organizing and livening up countless get–togethers and parties. She was a driving force behind the MEDISIP Ladies' Nights, which were so much fun (and allowed us to get an update on all the gossip)! She was also a tremendous help in the practicalities of finishing this PhD. **Shandra** also contributed a lot for our group bond, even after she left UGent, with parties, trips, sports activities, board game nights... **Victoria** is incredibly sweet and like me is not embarrassed to dance any time of the day or night. We had great moments together (including the infamous "dancing on the table" incident). **Willeke** always had a smile on her face and never hesitated to shift the group conversations to English so I could more easily participate. **Ester** and **Stijn** have been my office and lunch mates for the last period of my PhD, so they were the first to know and give me advice on the latest developments (i.e. gossip) in my life. They started our weekly Coffee Breaks, and there we were joined by **Gwennaelle**, **Jens**, **Paulo**, **Thibault** and **Kim** to finally understand and discuss what the hell each of us is doing in our research. **Saskia** and **Inge** have been invaluable to me and to MEDISIP, by taking care of most administrative tasks and many other things. Whenever I had a question or request they made sure it was answered as fast as possible, even if this meant several e-mails and phone calls. They also organized many great group events which will remain in my memory. And lastly, all my other colleagues who have enriched my journey: **Benedicte**, **Chris**, **Enrico**, **Ewout**, **Gregor**, **Hendrik**, **Kasper**, **Katya**, **Margo**, **Pieter Mollet**, **Pieter Van Mierlo**, **Roma**, **Samuel**, **Scharon**, **Sinem**, **Syed** and **Vincent** (and I'm sorry if I forgot anyone!).

I also thank the many other scientists, research groups and organizations that have been a part of my PhD experience. In particular, I'd like to mention our university flat-mates from **bioMMeda** and the many interesting researchers I met at the IEEE NSS/MIC conferences. I also cannot forget **FWO** (Research Foundation Flanders), for funding my research, as well as **Ghent University** and the **Doctoral Schools**, for offering me the opportunity to do courses and training in many non-research areas.

I am very grateful to **Belgium** and **Ghent**, for all the amazing opportunities I've had to learn and grow, which more than made up for all the rain and snow. I will hold dearly my experience with **TEDxGhent** and **CoderDojo**, and all the passionate people I've met there. I also made some good friends here who made me think about things other than work, namely **Ludmilla**, **Marta**, **Beatriz**, **Evelien**, **Diana** and **Anna-Luise**.

My boyfriend **Matthias**, the coolest, sweetest, most talented person I've ever met (yes I actually checked everyone and compared them to him), has given me unconditional support and helped me on so many levels... He made things so much easier, thank you thank you thank you!

I have also received a lot of support from my best friends in Portugal, **Sara** and **Telma**, who I've known for half of my life but who never cease to surprise me.

And last but not least, I owe a lot to my family, who have always been by my side and respected my choices in life. First of all **my sister Madalena**, who has been my life-long companion, through laughs and tears, through love and hate, the person in the world who I know I can always count on. **My mother** has been my greatest role model, showing me the value of your word and principles, and how much you can accomplish with your drive. **My father** has been dedicated and caring, selfless to a fault, sometimes giving me more freedom than I deserved. And then there are my grandparents, aunts/uncles and cousins, who I miss now much more than when I was living closer.

Thank you all so much! I wish you all the best! Follow your gut, what makes you happy, and not what you think you're supposed to be or do. You are the one living your life, you are the one expert in the world at that. And if you dream of doing something, start working towards it right now, no excuses!

Lara
August 2016
Ghent, Belgium

"Who looks outside, dreams; who looks inside, awakes."

Carl Gustav Jung

Table of Contents

Table of Contents i

List of Figures v

List of Tables xiii

List of Acronyms xv

English Summary xxi

Nederlandstalige Samenvatting xxv

1 Introduction **1**
- 1.1 Medical Imaging 1
- 1.2 Motivation 8
- 1.3 Outline 9

2 Background **13**
- 2.1 Single Photon Emission Computed Tomography (SPECT) 13
- 2.2 Collimators 15
  - 2.2.1 Pinhole 16
  - 2.2.2 Parallel-hole 19
  - 2.2.3 Production Techniques and Novel Collimator Designs 22
- 2.3 Image Reconstruction 24
  - 2.3.1 The Imaging Problem 24
  - 2.3.2 Iterative Reconstruction 25
  - 2.3.3 MLEM 27
  - 2.3.4 PML 30
- 2.4 System Modeling 33
  - 2.4.1 Analytical Methods 33

2.4.2 Monte Carlo Simulations 36
2.4.3 Experimental System Matrix 39
2.5 Image Quality 40
2.5.1 Overview 40
2.5.2 FIM-based Approximation for Evaluation of Image Quality in PF-PML 46
2.6 Summary 47

3 Modeling of Geometric Response of Complex Collimator Geometries in SPECT 49
3.1 Introduction 49
3.2 Application 1: Pinholes and Loftholes 50
3.2.1 Analytical Method 50
3.2.1.1 Circular exit (pinhole) 52
3.2.1.2 Square exit (lofthole) 56
3.2.2 Simulations 60
3.2.3 Results and Discussion 61
3.3 Application 2: Parallel-holes of Non-standard Shape . . . 64
3.3.1 Analytical Method 64
3.3.2 Simulations 66
3.3.3 Results and Discussion 68
3.3.3.1 Cylindrical System 68
3.3.3.2 Hexagonal System 71
3.3.3.3 Final Remarks 72
3.4 Summary and Original Contributions 74

4 Evaluation of Fisher Information Matrix-based Methods for Fast Assessment of Image Quality in SPECT 75
4.1 Introduction 76
4.2 Methods 77
4.2.1 Local Shift-Invariance 77
4.2.2 Non-Uniform Object-Space Pixelation 81
4.2.3 Subsampled Fisher Information Matrix 83
4.3 Parallel-hole SPECT 84
4.3.1 Simulations 84
4.3.1.1 System Modeling and Phantom 84
4.3.1.2 Figures of Merit for Image Quality 86
4.3.2 Results and Discussion 87
4.4 Pinhole SPECT 90
4.4.1 Simulations 90

4.4.1.1 System Modeling 90
4.4.1.2 Phantoms 92
4.4.1.3 Experiments 94
4.4.2 Results 95
4.4.2.1 FIM Columns 95
4.4.2.2 Figures of Merit for Image Quality 96
4.4.2.3 Mean errors 97
4.4.2.4 Efficiency 101
4.4.3 Discussion 101
4.4.3.1 Local Shift-Invariance Approach 102
4.4.3.2 Alternative Approaches 104
4.5 Final Remarks and Guidelines for Method Selection . . . 105
4.6 Summary and Original Contributions 108

5 Parallel-hole Collimator Concept for Stationary SPECT Imaging 109
5.1 Introduction 109
5.2 Methods 111
5.2.1 The Concept 111
5.2.2 Simulated Systems 112
5.2.3 Simulations 114
5.2.3.1 Sensitivity, Resolution and Noiseless Reconstructions 114
5.2.3.2 Noisy Reconstructions 115
5.3 Results 115
5.3.1 Sensitivity, Resolution and Noiseless Reconstructions 115
5.3.2 Noisy Reconstructions 117
5.4 Discussion 119
5.5 Summary and Original Contributions 123

6 Comparison Study: New Stationary System vs Rotating System in Clinical Brain Imaging 125
6.1 Introduction 125
6.2 Simulations 127
6.2.1 The Systems 127
6.2.2 Evaluation of Image Quality 128
6.3 Results and Discussion 129
6.4 Summary and Original Contributions 132

7 Collimator Geometry for Highly Compact, Stationary

Small-Animal SPECT Imaging **135**

- 7.1 Introduction . . . 135
- 7.2 Methods . . . 136
  - 7.2.1 System Design . . . 136
  - 7.2.2 System Matrix . . . 138
  - 7.2.3 Simulations . . . 139
    - 7.2.3.1 Sensitivity, Resolution and Noiseless Reconstructions . . . 139
    - 7.2.3.2 Noisy Reconstructions . . . 140
- 7.3 Results . . . 141
  - 7.3.1 Sensitivity, Resolution and Noiseless Reconstructions . . . 141
  - 7.3.2 Noisy Reconstructions . . . 142
- 7.4 Discussion . . . 145
- 7.5 Manufacturing and Preliminary Experimental Results . . . 146
- 7.6 Summary and Original Contributions . . . 148

8 Conclusion **151**

- 8.1 Summary . . . 151
- 8.2 Future Research . . . 154
- 8.3 Final Conclusion . . . 156

References **159**

List of Publications **177**

List of Figures

1.1 A chest X-ray. The lighter areas correspond to a higher attenuation of the X-rays, usually as a result of bone. . . 2

1.2 A CT scan of the neck area. The top left image is a 3D rendering, and the remaining pictures are cross-sectional slices through the 3D image. The principle is the same as with X-ray imaging, but we can see that much more detailed information is visible. 3

1.3 Ultrasound of the urinary bladder and hyperplastic prostate. 4

1.4 An MRI image of the human brain. 5

1.5 Nuclear imaging scans. (a) A human brain PET scan, using the tracer 18F-FDG. (b) A bone SPECT scan of a mouse, using the tracer Tc-99m-HDP. 6

1.6 Examples of SPECT scanners. (a) The Triple Head human SPECT scanner Prism 3000 NewTec, from Inter Medical; it supports both parallel-hole and fanbeam collimators. (b) The stationary small animal SPECT/CT system U-SPECT II, from MILabs, which uses multi-pinhole collimation. 8

2.1 A schematic representation of how a SPECT scanner works. 14

2.2 Schematic representation of a standard pinhole aperture. . 16

2.3 Schematic representation of a single pinhole collimator imaging a region of interest in the object. 16

2.4 Schematic representation of a standard pinhole aperture and detector, showing the meaning of the variables used in equations (2.2) and (2.3). The subfigures (a) and (b) refer to the sensitivity and resolution calculations, respectively. 17

2.5 Schematic representation of a stationary multi-pinhole collimator and corresponding FOV. 19

2.6 Schematic representation of a parallel-hole collimator imaging the object. 20
2.7 Schematic representation of a parallel-hole collimator and detector, showing the meaning of the variables used in equations (2.4) and (2.5). The subfigures (a) and (b) refer to the sensitivity and resolution calculations, respectively. 20
2.8 Schematic representation of a standard pinhole (a) and a lofthole with square entrance and exit openings (b). In both cases a top and a side view is shown. 23
2.9 Schematic representation of the steps performed during an implementation of the MLEM algorithm. 29
2.10 Images obtained from simple MLEM reconstruction, at different number of iterations. (a) Original phantom; (b) reconstructed image at iteration 10; (c) reconstructed image at iteration 50; (d) reconstructed image at iteration 200. One can see that the images become increasingly plagued by high-frequency noise as the number of iterations increases. 29
2.11 Final reconstruction images obtained from different reconstruction algorithms. (a) Original phantom; (b) reconstructed image at iteration 200, using simple MLEM reconstruction; (c) reconstructed image at iteration 200, using simple MLEM reconstruction followed by Gaussian filtering; (d) reconstructed image at iteration 200, using PML reconstruction (uniform quadratic penalty, first-order neighborhood). 30
2.12 Schematic representation in 2D of the voxelized image space, the gamma camera (based on parallel-hole collimation) and the projection bins. In a very simple projection model, the values of the voxels in the highlighted row would be summed to obtain the value of the projection bin that is located along the same line. 34
2.13 Schematic representation in 2D of ray-tracing methods, considering a pinhole aperture modeled as one point through its center: (a) pixel-driven; (b) ray-driven; (c) distance-driven. 35
2.14 Plot of a cumulative probability distribution $CPDF$, where a random number $R \in [0, 1]$ is used to choose the value of a random variable x, which is equivalent to the direct sampling of the PDF. 37

2.15 Modeling of a SPECT system in GATE. The detector material is shown in yellow, the collimator body in blue, and the phantom in purple. Also represented are two simulated photon trajectories (in green), which start in the phantom (where the activity is located). 38

3.1 Schematic representation of a standard pinhole aperture and detector, showing the detector umbra and penumbra regions. 51
3.2 Three possible collimator geometries and the corresponding A_{int} region. 51
3.3 Schematic representation of a detector and a collimator with a single aperture, showing the high-sensitive, low-sensitive and insensitive areas of the image-space and detector. 53
3.4 Representation of the pinhole in the reference frame and some points of interest. 54
3.5 Intersection of the pinhole aperture circle with the exit circle projection from the point source onto the aperture plane. 54
3.6 Extreme case of the exit opening projection from a point source in the High Sensitivity Region onto the aperture plane. 57
3.7 Extreme cases of the exit opening projections from point sources in the No Sensitivity Region onto the aperture plane. 57
3.8 The different possible intersection shapes of the aperture with the exit opening projection. 58
3.9 Collimator geometries and variables used. 61
3.10 Plot of g, g_{corr} and $g_{simulated}$ for the pinhole geometry, comparing the collimator thicknesses t_1 and t_2 ($t_1 > t_2$). 62
3.11 Plot of g, g_{corr} and $g_{simulated}$ for the pinhole and lofthole geometries ($t = t_1$). 62
3.12 2D illustration of the principle behind the sensitivity calculation for a single parallel hole. 65
3.13 Schematic representation of the SPECT systems developed in chapters 5 and 7 (not to scale). The main collimator body is shown, along with a view of some of its transaxial slices. (a) Cylindrical system (Chapter 5); (b) Hexagonal system (Chapter 7). 67

3.14 Projections of a voxel. 69
3.15 Zoomed-in view of the projections shown in Fig. 3.14. . . 70
3.16 Sensitivity of the bottom detector to the cube phantom at bed positions corresponding to the center of each of the 128 transaxial collimator slices, using the analytical (red) and GATE (blue) modeling. Subfigures (1) to (3) correspond to the phantom positions shown in Fig. 3.17 (a1) to (a3), respectively. 72
3.17 Projection of a voxel cube onto the bottom detector, where columns 1 to 3 correspond to different voxel positions. (a) shows a schematic representation of the voxel position considered. (b) and (c) show a zoomed-in view of the analytical and GATE projections, respectively. (d) shows the line profile through the dashed line in both the analytical (red) and GATE (blue) projections. 73

4.1 A transaxial view of the phantom considered (Hoffman), showing the voxels at which the CRC and variance are computed. 85
4.2 CRC values given by the different LSI approximation methods (blue) versus the gold standard value (green), where each subfigure corresponds to a different approximation method and each bar in the subfigure corresponds to a different voxel of interest. 88
4.3 Variance values given by the different LSI approximation methods (blue) versus the gold standard value (green), where each subfigure corresponds to a different approximation method and each bar in the subfigure corresponds to a different voxel of interest. 89
4.4 CRC values given by the NUOP and subsampled approximation methods (blue) versus the gold standard value (green), where each subfigure corresponds to a different approximation method and each bar in the subfigure corresponds to a different voxel of interest. 91
4.5 Variance values given by the NUOP and subsampled approximation methods (blue) versus the gold standard value (green), where each subfigure corresponds to a different approximation method and each bar in the subfigure corresponds to a different voxel of interest. 92
4.6 Phantoms and ROIs. 93

4.7 Images corresponding to the jth column of the FIM using the phantoms and ROIs in Fig. 4.6. 96
4.8 Images of each FOM considered for the central ROI in the disk phantom, for the 32-angle sampling protocol. . . 97
4.9 RMSE (%) of the CRC obtained from each approximation method against the sampling protocol. 98
4.10 RMSE (%) of the (off-diagonal) LIR obtained from each approximation method against the sampling protocol. . . 98
4.11 RMSE (%) of the variance obtained from each approximation method against the sampling protocol. 99
4.12 RMSE (%) of the (off-diagonal) covariance obtained from each approximation method against the sampling protocol. 99

5.1 Schematic representation of a collimator design (not to scale) using the proposed concept. 111
5.2 Schematic representation of the type of SPECT system simulated in this chapter (not to scale), with some of the symbols and designations used. 112
5.3 Sensitivity map for the human full-body system. 116
5.4 Transaxial view of the hot-rod Derenzo phantom (a) and its noiseless MLEM reconstruction (b), for the three systems considered. 116
5.5 The uniform cylindrical phantom (a) and its noiseless MLEM reconstruction (b). 117
5.6 The XCAT phantom (a) and its MLEM reconstruction from noisy projections (b). 118
5.7 The Hoffman phantom (a) and its MLEM reconstruction from noisy projections (b). 119
5.8 The MOBY phantom (a) and its MLEM reconstruction from noisy projections (b). 120

6.1 A transaxial view of the phantom considered (Hoffman), showing the voxels at which the CRC, variance and CNR are computed (this is the same as in Chapter 4, Section 4.3.1.1). 128
6.2 Central transaxial slice of the sensitivity map for (a) the rotating system and (b) the stationary system. For each voxel, the intensity in the image represents the geometric sensitivity of the system to that voxel. The values of the color scale are given in cps/MBq. 129

6.3 Transaxial view of the reconstructed hot-rod Derenzo phantom for (a) the rotating system and (b) the stationary system. . . . 130

6.4 The CRC value, computed with the subsampled FIM method with grid G_2, at 5 representative voxels (P_1 to P_5) in the central transaxial slice of the Hoffman phantom. The blue bars represent the values obtained with the rotating system, the red bars the stationary system. . 131

6.5 The variance value, computed with the subsampled FIM method with grid G_2, at 5 representative voxels (P_1 to P_5) in the central transaxial slice of the Hoffman phantom. The blue bars represent the values obtained with the rotating system, the red bars the stationary system. . 131

6.6 The CNR value, computed with the subsampled FIM method with grid G_2, at 5 representative voxels (P_1 to P_5) in the central transaxial slice of the Hoffman phantom. The blue bars represent the values obtained with the rotating system, the red bars the stationary system. . 132

7.1 Schematic representation of the SPECT system developed in this chapter (not to scale), which has a hexagonal detector setup. . . . 137

7.2 The system symmetries which we use to reduce the number of system matrix elements computed. . . . 138

7.3 Sensitivity map. . . . 141

7.4 The uniform cylindrical phantom (a) and its noiseless MLEM reconstruction (b). . . . 142

7.5 The hot-rod Derenzo phantom (a) and its noiseless MLEM reconstruction (b). . . . 143

7.6 The cold-rod Derenzo phantom (a) and its noiseless MLEM reconstruction (b). . . . 143

7.7 The uniform cylindrical phantom (a) and its MLEM reconstruction from noisy projections (b). . . . 144

7.8 The ROBY phantom (a) and its MLEM reconstruction from noisy projections (b). . . . 144

7.9 Test piece of the collimator, printed using metal additive manufacturing, where the printing was done along the axial direction. . . . 147

7.10 Schematic drawing of one of the 3 pieces in which the collimator was divided in order to be printed. . . . 148

7.11 Photos of the full collimator from two different views, showing the three printed parts fitted together. 149
7.12 Reconstruction of a partially filled 20 ml syringe, scanned with 675 μm axial bed steps while keeping the system stationary. The images shown result from 50 MLEM iterations. 149

List of Tables

4.1 NUOP Rebinning Strategy 86
4.2 Error (%) of the CRC obtained from each approximation method at the voxels of interest. 90
4.3 Error (%) of the Variance obtained from each approximation method at the voxels of interest. 90

5.1 The parameters of the full-body, brain and small-animal systems simulated in this work. 113

List of acronyms

A

ACE	Artificial Compound-Eye

C

CBC	Circulant-Block-Circulant
CFOV	Central Field Of View
CNR	Contrast-to-Noise Ratio
CPU	Central Processing Unit
CRC	Contrast Recovery Coefficient
CT	Computed Tomography

D

DFT	Discrete Fourier Transform

E

ECD	Ethyl Cysteinate Dimer
EM	Expectation Maximization
ET	Emission Tomography

F

FBP	Filtered Backprojection
FFT	Fast Fourier Transform
FIM	Fisher Information Matrix
FOM	Figure Of Merit
FOV	Field Of View
FWHM	Full Width at Half Maximum

G

GATE	Geant4 Application for Tomographic Emission
GPU	Graphics Processing Unit

H

HMDP	Hydroxymethylene Diphosphonate

I

IQ	Image Quality

L

LIR	Local Impulse Response
LSI	Local Shift-Invariant

M

ML	Maximum Likelihood
MLEM	Maximum Likelihood Expectation Maximization
MOBY	Mouse Whole Body
MRI	Magnetic Resonance Imaging

N

NUOP	Non-Uniform Object-space Pixelation

O

OSEM	Ordered Subsets Expectation Maximization

P

PDF	Probability Density Function
PET	Positron Emission Tomography
PF-PML	Post-Filtered Penalized Maximum Likelihood
PML	Penalized Maximum Likelihood
PMT	Photomultiplier Tube
PSF	Point Spread Function

R

RMSE	Root Mean Squared Error
ROBY	Rat Whole Body
ROI	Region Of Interest

S

SNR	Signal-to-Noise Ratio
SPECT	Single Photon Emission Computed Tomography

X

XCAT	Extended Cardiac-Torso

English Summary

Nederlandstalige Samenvatting

English Summary

Single Photon Emission Computed Tomography (SPECT) is an imaging technique in the field of nuclear medicine, which allows us to visualize biochemical and physiological processes in living bodies. It is a non-invasive procedure that makes use of a radioactively labeled substance. This substance takes part in a metabolic process of interest similarly to the way the non-radioactively labeled substance would interact. By measuring the emitted gamma-radiation, we can track its movement and accumulation throughout the body. SPECT is a very useful technique to study processes and diseases that do not cause significant anatomical changes or take a longer time to do so, such as tumors. It is used in several areas of medicine and research.

A SPECT scanner is based on two fundamental components: the detector and the collimator. The function of the detector is to register incoming gamma photons, providing the position of the interaction of the detector with a gamma photon coming from the source. In order to trace the origin of each of these photons, which is the goal of the imaging process, we also need to determine the direction from which they originate and this is where the collimator comes in. It consists of a block of very dense material with small holes, positioned between the object being imaged and the radiation detector. If a gamma photon hits the collimator material, it is most likely attenuated, so most of the photons that eventually reach the detector are those that are able to go through the aperture holes without touching the collimator walls. As such, the position and shape of the collimator apertures gives us information about the possible trajectories of the detected gamma photons, with varying degrees of probability, and limits the regions in space in which the source(s) can be located.

To accurately locate the radiation source(s), we need to detect radiation from different angles around the object. Roughly speaking, if we

would have a single point source it would be located at the intersection of the possible trajectories of the photons that we detect at these different angles. This angular sampling is usually done by rotating the detector and the attached collimator around the object, while the object itself stays still. With the information we obtain from the SPECT system and a model of the acquisition system, the 3D distribution of the radioactive sources is estimated using an image reconstruction algorithm.

In this thesis we investigate innovative SPECT system designs, in particular with complex collimator geometries, which are now possible due to the advancement of metal additive manufacturing. We do this using simulation studies, which are more versatile, practical and cost-efficient for performing initial tests than building the actual system and performing experiments. These simulations are highly dependent on how well the SPECT system is modeled. In a first phase of this dissertation we will thus develop accurate and efficient analytical methods for this purpose. The methods were tested in four different types of collimators: two with pinhole-type apertures and two with parallel-hole-type apertures. We observe a very good match between the analytical methods and more realistic (but also more lengthy) simulation methods. The developed methods can be very useful tools for accurately evaluating system performance, guiding the system design and building better reconstruction models, especially when non-standard system geometries are involved, which is the case of the systems developed in this dissertation (and whose design corresponds to the parallel-hole-type systems for which the methods are validated here).

In a second phase, we study fast approaches for evaluation of the image quality of a SPECT system. These approaches are based on approximations of the covariance and local impulse response of the reconstructed images using the Fisher Information Matrix. These techniques are very often used in literature, but usually without a thorough validation, which means that we cannot be sure if we can indeed rely on them for accurately evaluating the scanner's performance. Using two standard SPECT systems, we compare different approaches based on three basic theories: local shift-invariance, non-uniform object-space pixelation, and subsampled Fisher Information Matrix. These approaches have never been compared with each other in literature before, so we not only wanted to see if they would match the gold standard method, but also how they performed relative to each other. Our results indicate that, at least in the systems evaluated here, the popular local shift-invariance technique is less reliable than the alternative approaches, and in some cases its performance is considerably worse. Although more thorough tests should be performed to generalize these conclusions, we believe this is a strong motivation for further research into alternatives to the local shift-invariant approximation method.

In a third phase of the thesis, we develop a new type of SPECT system. To do this, we made use of the tools previously investigated for system modeling and evaluation of image quality. The collimator and detector completely surround the object (in the transaxial plane) and instead of having to rotate the system in order to sample the object along different directions we merely need to translate the object along the longitudinal direction of the system. This is because the innovative collimator geometry has parallel-hole apertures whose axis is rotated on a different direction according to their position along the longitudinal axis of the system. The fact that the system is stationary, as opposed to rotating, has several advantages, such as the absence of rotation-related artifacts in the images, improved stability, less need for maintenance, etc. Furthermore, compared to current stationary SPECT systems, this design allows the system to be more compact, which can be an asset not only in terms of savings in space and materials, but also for applications which have spatial restrictions, such as in SPECT-MR scanners.

Using simulations, we explore the use of the proposed collimator concept in human full-body, human brain, and small-animal imaging. The reconstruction images for all three applications show potential and the performance is comparable to standard parallel-hole SPECT systems. At this stage the human brain and small-animal applications seem to be the most promising, especially taking into account that for larger collimators the manufacturing costs get significantly higher. As such, we explore these two applications in more detail.

We first investigate the application to brain imaging and compare the performance of a standard parallel-hole SPECT system with a simple cylindrical system design using the new stationary SPECT concept. Using the previously determined method for the assessment of image quality based on the Fisher Information Matrix, the proposed system shows a slight improvement in performance. Since we did not model the effects of rotation, which are generally detrimental to image quality, in the simulations of the standard rotating system, we conclude that the proposed stationary system could be more advantageous in clinical practice than the currently used scanners.

Finally, we further explore an application to small-animal imaging.

In particular, we propose a design that enables imaging of rat-sized objects in a currently existing detector setup (which is used to image mice with multi-lofthole collimation). The simulated images obtained with the system show a reasonable performance, even though the sensitivity-resolution trade-off is inferior to other state-of-the-art small-animal SPECT systems that are also stationary. The main advantage of the system compared to alternative stationary SPECT systems, based on multi-pinhole collimation, is its more efficient use of space, which means it can be much more compact. We are currently working on the validation of an initial prototype of this system, which may be used in the future in small-animal SPECT scanners in our lab.

The research presented in this dissertation was performed at MEDISIP (Medical Imaging and Signal Processing group); this research group is part of the Electronics and Information Systems department of the Faculty of Engineering and Architecture of Ghent University (Belgium). This work has resulted so far in three A1 journal publications (two as first author), one patent application, one book chapter and six contributions at international conferences.

Nederlandstalige Samenvatting

Single Photon Emission Computed Tomography (SPECT) is een nucleaire beeldvormingstechniek die toelaat om biochemische en fysiologische processen te visualiseren in het lichaam. Het is een niet-invasieve methode waarbij een radioactief gemerkte stof ingespoten wordt in het lichaam van de patiënt. Deze radioactief gemerkte stof is door het lichaam niet te onderscheiden van lichaamseigen stoffen en zal dus deelnemen aan specifieke lichamelijke processen. Door de uitgezonden gammastraling op te meten is het dan mogelijk de beweging en ophoping van deze stof in het lichaam te visualiseren. Het is een nuttige techniek om processen en ziektes te bestuderen die geen significante anatomische veranderingen met zich meebrengen of zich traag ontwikkelen, zoals kanker. Als dusdanig vindt SPECT vele toepassingen in de geneeskunde en klinisch onderzoek.

Een SPECT-scanner bestaat uit twee fundamentele onderdelen: een detector en een collimator. De detector zal de invallende gammafotonen waarnemen door te registreren waar er een interactie optreedt tussen het detectormateriaal en de gammafotonen afkomstig van de stralingsbron(nen). Om de herkomst van deze fotonen te traceren, het eigenlijke doel van beeldvorming, moeten we ook informatie verwerven over de richting waarin de fotonen zich bewegen: hiervoor is de collimator belangrijk. De collimator bestaat uit een blok zeer dens metaal met kleine openingen dat tussen het object en de stralingsdetector wordt geplaatst. Gammafotonen die het collimatormateriaal raken worden doorgaans tegengehouden. De fotonen die de detector bereiken zijn dus meestal diegene die ongehinderd door de openingen in de collimator zijn gepasseerd. De locatie en de vorm van de collimator geeft ons dus informatie over de waarschijnlijkheid dat de gammafotonen de detector bereiken en de mogelijke trajecten die ze kunnen afleggen. Dit laat ons toe om een regio te definiëren waar de stralingsbronnen gelegen zijn.

Om op nauwkeurige wijze de locatie van de stralingsbron(nen) te achterhalen, moeten we de uitgezonden straling vanuit verschillende hoeken rondom het object opmeten. In het een vereenvoudigde geval van een puntbron wil dit zeggen dat de bron zich in theorie op de locatie waar de verschillende fotontrajecten elkaar kruisen bevindt, wanneer deze vanuit meerdere hoeken wordt gedetecteerd. De opnames onder verschillende hoeken worden gemaakt door de detector samen met de bijhorende collimator rondom het object te bewegen terwijl het object zelf stationair blijft. Door gebruik te maken van de informatie die het SPECT-systeem ons geeft en een computermodel van het beeldvormingssysteem, kan de distributie van de radioactieve bronnen geschat en omgezet worden in een 3D-beeld door een zogenaamd beeldreconstructie-algoritme.

In deze thesis onderzoeken we innovatieve SPECT-ontwerpen met bijzondere aandacht voor complexe collimatorgeometrieën die mogelijk zijn door recente ontwikkelingen in het 3D-printen van metaal. Voor dit onderzoek doen we een beroep op simulaties omdat ze een veelzijdiger, makkelijker en goedkoper alternatief zijn dan het effectief bouwen en testen van de systemen. Omdat deze simulaties sterk afhankelijk zijn van de modellering van het SPECT-systeem, werden in de eerste fase van de dissertatie accurate en efficiënte analytische methoden ontwikkeld. De methodes werden getest met vier verschillende collimatortypes: twee met *pinhole*-achtige openingen en twee met *parallel-hole*-achtige openingen. We behaalden gelijkaardige resultaten met de analytische methoden en de meer realistische (maar ook langere) simulatiemethoden. De ontwikkelde methoden zijn een handig hulpmiddel voor de accurate evaluatie van systeemprestaties en kunnen gebruikt worden om systeemontwerpen te verbeteren en betere reconstructiemodellen te bouwen. De methode is vooral nuttig voor opstellingen waarin geometrieën gebruikt worden die afwijken van de huidige standaarden, zoals voorgesteld in de dissertatie (en waarvan het ontwerp overeenstemt met *parallel-hole* systemen waarvoor de methoden werden gevalideerd).

In de tweede fase van het onderzoek bekijken we enkele snelle methodes voor de evaluatie van de SPECT beeldkwaliteit. Deze methodes zijn gebaseerd op benaderingen van de covariantie en het lokale impulsantwoord van de gereconstrueerde beelden gebruikmakend van de Fisher informatie matrix. Deze methoden worden in de literatuur vooral gebruikt zonder grondige validatie, waardoor men niet zeker kan zijn of ze de prestaties van de scanner op een accurate wijze evalueren. We hebben verschillende methodes vergeleken door gebruik te maken van twee standaard SPECT-systemen. De methodes zijn gebaseerd op drie fundamentele theorieën: lokale shift-invariantie, niet-uniforme objectruimte pixellatie en gesubsamplede Fisher informatie matrix. Aangezien deze methodes nog nooit eerder vergeleken werden, wilden we ze niet enkel vergelijken met de gouden standaard, maar ook bestuderen hoe ze onderling presteerden. Onze resultaten tonen aan dat, voor de hier geëvalueerde systemen, de veel gebruikte lokale shift-invariantie techniek veel minder betrouwbaar is dan de alternatieven. In sommige gevallen was het resultaat zelfs beduidend slechter. Hoewel er meer testen moeten worden uitgevoerd om de bevindingen te veralgemenen, geloven we dat dit een sterke drijfveer is om alternatieven voor de lokale shift-invariantie benaderingsmethode verder te onderzoeken.

In de derde fase van dit thesisonderzoek ontwikkelden we een nieuw SPECT-systeem met behulp van de eerder ontwikkelde methoden voor de modellering van het systeem en de evaluatie van de beeldkwaliteit. In deze opstelling omhullen de collimator en de detector het object volledig (in het transaxiaal vlak) en worden opnames uit verschillende hoeken gemaakt door het object te translateren langs de longitudinale as van het systeem. Bij dit ontwerp is het dus niet langer nodig om het systeem te roteren rond het object. Dit is mogelijk door de innovatieve collimator-geometrie met *parallel-hole*-achtige aperturen. De assen van de collimatoropeningen zijn in functie van de positie langs de longitudinale as van het systeem namelijk in verschillende richtingen geroteerd. Doordat het systeem stationair is, zijn er enkele voordelen tegenover roterende systemen: er zijn geen rotatie-gebonden artefacten, de stabiliteit is hoger en er is minder onderhoud nodig. Een bijkomend voordeel tegenover huidige stationaire SPECT-systemen is dat het concept gebruikt kan worden in zeer compacte systemen. Dit is niet alleen een pluspunt in termen van materiaalkost en ruimte, het principe is ook interessant voor toepassingen met ruimtelijke beperkingen zoals in SPECT-MR scanners.

Via simulaties onderzochten we het gebruik van het voorgestelde collimatorconcept voor beeldvorming toegepast op het menselijk lichaam, de hersenen en kleine proefdieren. De gereconstrueerde beelden zijn veelbelovend voor deze drie toepassingen aangezien de prestaties vergelijkbaar zijn met die van standaard *parallel-hole* SPECT-systemen. In dit stadium hebben toepassingen met betrekking tot het menselijk brein en kleine proefdieren het meeste potentieel. Dit omdat de productiekosten voor grote collimatoren veel hoger zijn. We kozen er daarom voor om deze twee toepassingen in meer detail uit te werken.

We onderzochten eerst de toepassingen voor hersenscans en vergeleken daarbij de prestaties van een standaard *parallel-hole* SPECT systeem met een simpel cilindrisch systeem gebaseerd op het nieuwe stationaire SPECT concept. We gebruikten de meest accurate methode voor het bepalen van de beeldkwaliteit op basis van de Fisher informatie matrix en vonden dat het nieuwe systeem iets beter presteerde. Aangezien de simulaties geen rekening houden met de rotatie-effecten die de beeldkwaliteit doorgaans aanzienlijk verslechteren, kunnen we besluiten dat het voorgestelde stationaire systeem meer voordelen te bieden heeft in een klinische omgeving dan de huidige scanners.

Finaal onderzoeken we de preklinische toepassingen, met speciale aandacht voor ontwerpen die toelaten om voorwerpen ter grootte van een rat in een reeds bestaande detectorsetup in beeld te brengen. Deze bestaande setup wordt vaak gebruikt om muizen in beeld te brengen met multi-lofthole collimatoren. De gesimuleerde beelden die verkregen werden met dit systeem bezitten een aanvaardbare kwaliteit. In vergelijking met andere stationaire, state-of-the-art preklinische SPECT-systemen, is de balans tussen sensitiviteit en resolutie echter lager. Het grootste voordeel is dat het nieuwe systeem veel compacter gemaakt kan worden. We zijn momenteel een eerste prototype van dit systeem aan het testen opdat het ontwerp in de toekomst gebruikt zou kunnen worden in kleine SPECT-scanners in ons lab.

Het onderzoek beschreven in deze dissertatie werd uitgevoerd in MEDISIP (Medical Imaging and Signal Processing group); deze groep maakt deel uit van het departement voor elektronica en informatiesystemen van de faculteit Ingenieurswetenschappen en Architectuur van de Universiteit Gent (België). Dit werk heeft tot dusver geleid tot drie A1 publicaties in wetenschappelijke tijdschriften (twee als eerste auteur), een octrooiaanvraag, een hoofdstuk in een boek en zes bijdragen aan internationale conferenties.

Chapter 1

Introduction

1.1 Medical Imaging

Medical imaging has revolutionized medical practice and research, by allowing us to non-invasively observe the inside of the body. It helps doctors with the diagnosis, monitoring and treatment of many medical conditions, and in research it is used to investigate the mechanisms behind processes in the body, diseases, the action of drugs, etc.

Different types of imaging techniques are used for different purposes. Each has its own advantages and disadvantages, which makes them quite complementary, and often the same patient is scanned on different imaging modalities. The most commonly used modalities are X-ray radiography, Computed Tomography (CT), ultrasound, Magnetic Resonance Imaging (MRI), Positron Emission Tomography (PET) and Single Photon Emission Computed Tomography (SPECT), which we will shortly describe in this Section.

Imaging modalities can be divided into structural (or anatomical) and functional, according to what they allow us to visualize. Structural imaging techniques show the anatomy of the body, and allow us to distinguish different tissues; this is the case for X-ray, CT, ultrasound and MRI. Functional imaging modalities, on the other hand, show biological processes occurring in the body; this is the case in nuclear imaging (PET and SPECT), contrast-enhanced CT/MRI/ultrasound and also in the growing field of functional MRI (fMRI). Particular examples of each type of imaging will be given for each modality. Nowadays, the trend in medical imaging practice and research is to move towards multi-modality systems, i.e. merging more than one imaging modality in one scanner,

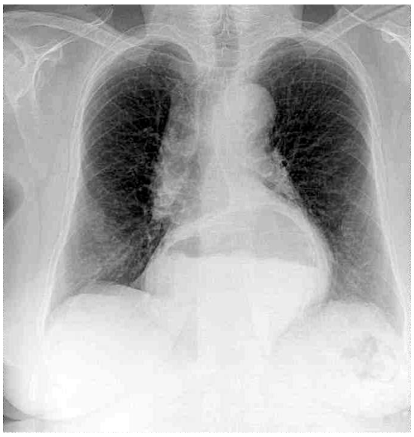

Figure 1.1: A chest X-ray. The lighter areas correspond to a higher attenuation of the X-rays, usually as a result of bone. [Image obtained from [1], used under a Creative Commons Attribution-ShareAlike license]

especially to combine functional and structural information in one image (e.g. PET/CT, SPECT/CT, PET/MR and SPECT/MR).

X-Ray Radiography

The first modality to be used for clinical purposes was X-ray planar radiography, in 1896.

An X-ray machine uses an X-ray beam that is sent through the body. When passing through the body, parts of the beam are absorbed. On the opposite side of the body, the transmitted X-rays are detected, resulting in a 2D image (see Fig. 1.1). Since different tissues absorb different amounts of radiation, according to how dense they are, they result in different shades of gray in the image (different photon intensities).

The most frequent use of X-rays today is to check for broken bones, cavities and swallowed objects. Other common uses are in breast cancer detection (mammogram) and in directing interventional instruments in the patient's body (interventional radiology). Furthermore, if a special contrast agent is injected on the patient beforehand, X-ray can be used to visualize organs and the interior of blood vessels (angiography).

The fact that this technique is 2D means that the body's internal structures will appear superimposed in the image, which can hinder the analysis of what we are investigating. Yet, despite the advance of 3D tomography, it is still in wide use. This is mainly due to the ease of use,

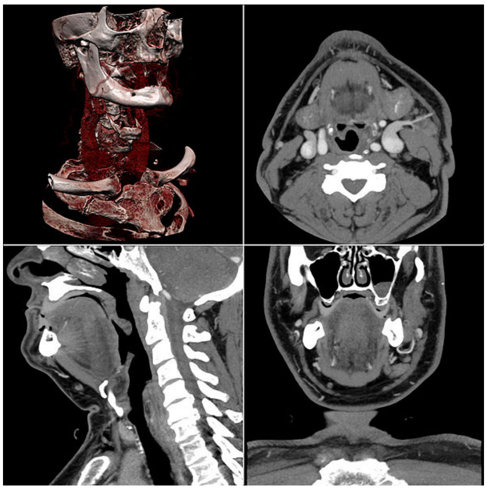

Figure 1.2: A CT scan of the neck area. The top left image is a 3D rendering, and the remaining pictures are cross-sectional slices through the 3D image. The principle is the same as with X-ray imaging, but we can see that much more detailed information is visible. [Image obtained from [2], used under a Creative Commons Attribution-ShareAlike license]

low cost, low radiation dose and high resolution, in both space and time (useful in interventional procedures).

Computed Tomography (CT)

Computed Tomography, most commonly known as CT or CAT, is based on the same principle as X-Ray imaging, but the X-Ray Source and the detector rotate around the body during the examination so that images at different angles can be acquired (see Fig. 1.2). With these 2D projections we are able to form a 3D image of the inside of the body, using what we call a "reconstruction algorithm" (see Section 2.3). CT is used for similar purposes to X-Ray, but the fact that it is 3D provides much more information, and it has a higher contrast compared to conventional X-ray imaging. On the other hand, because of the fact that the imaging is done from several different angles around the body, the total radiation exposure is considerably higher, and the increased complexity makes it a more expensive modality.

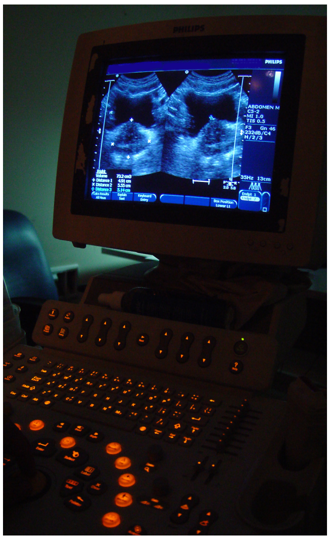

Figure 1.3: Ultrasound of the urinary bladder and hyperplastic prostate. [Image obtained from [3], used under a Creative Commons Attribution 3.0 Unported license]

Ultrasound

Ultrasound, echography or sonography, works like a radar. It uses a probe to transmit pulses of high frequency sound waves into the body. These waves penetrate the body tissue and are reflected on organs and structures inside the body, at the interface between different tissues, at different reflection rates depending on their composition. The signal that is returned to the probe is then converted into an image (see Fig. 1.3).

Ultrasound is mostly used to image organs, soft tissue and blood flow inside the body, and particularly for viewing the fetus during pregnancy (as it is harmless to the fetus). Nowadays it is possible to produce not only 2D but also 3D ultrasound images.

Although other techniques give more detail and accuracy, ultrasound is still very commonly used because it is relatively inexpensive, quick to perform, mobile, it shows the image immediately as it is being captured (on-the-fly), and it emits no ionizing radiation.

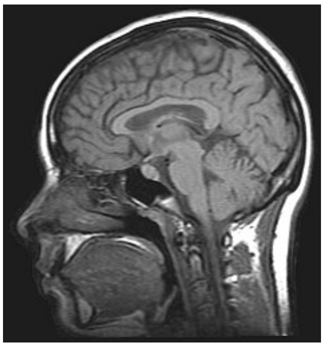

Figure 1.4: An MRI image of the human brain. [Image obtained from [4]]

Magnetic Resonance Imaging (MRI)

In a Magnetic Resonance Imaging (MRI) scanner, a strong main magnetic field (in the Tesla range) is present, and radio-waves are sent to the parts of the body which we are interested in, causing the nucleus of certain types of atoms that naturally exist within the body to align their spin. As the protons return to their usual alignment, they emit energy that varies according to the type of body tissue in which they lie, and based on this we are able to create a 3D image showing the different tissues.

An MRI image (see Fig. 1.4) allows us to distinguish different soft tissues much better than any other modality, including the difference between normal and diseased soft tissue, with a very high resolution, and without exposing the patient to ionizing radiation. Some of its most common applications are in neurological and musculoskeletal imaging. MRI also has functional capabilities, to do perfusion and molecular imaging, but with limitations in terms of sensitivity (the images produced are quite noisy). The main drawback of MRI imaging nowadays is its high cost.

Nuclear Imaging

The final category of medical imaging that we describe here is Nuclear Imaging. Like X-Ray and CT, it makes use of ionizing radiation. However, instead of having a radiation beam going through the patient, a small quantity of a radioactive substance, the tracer, is injected into the patient's bloodstream prior to the test. The tracer consists of a molecule

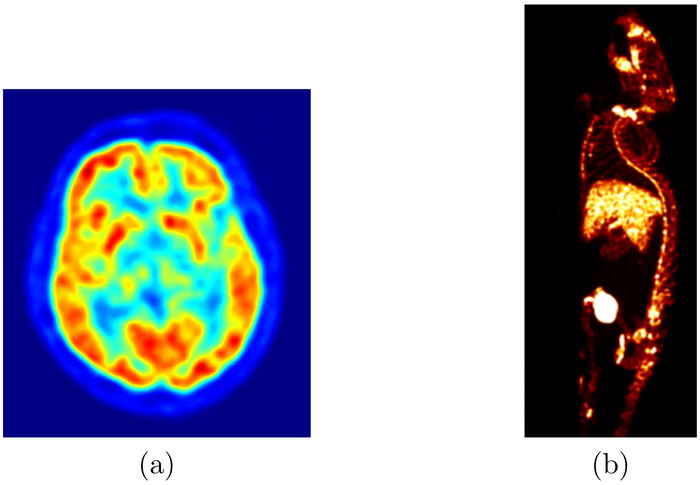
(a) (b)

Figure 1.5: Nuclear imaging scans. (a) A human brain PET scan, using the tracer 18F-FDG [image obtained from [5]]. (b) A bone SPECT scan of a mouse, using the tracer Tc-99m-HDP [image obtained from [6]].

that naturally exists in the body, but it is labeled with a radioactive isotope that causes the emission of gamma-rays. The gamma-rays are captured by detectors that surround the body, and with this information we are then able to make a 3D representation of the distribution of the tracer throughout the body.

The two main nuclear imaging techniques are Positron Emission Tomography (PET), seen in Fig. 1.5 (a), and Single Photon Emission Computed Tomography (SPECT), seen in Fig. 1.5 (b), depending on the type of radioactive particle that the isotope emits (positrons or gamma photons). The processes shown depend upon the particular substance which is injected into the patient. They can be used to detect and locate tumors, to image certain organs, blood flow, the distribution of a drug, and many more applications. For better localization, they are also commonly used in combination with either CT or MRI, which can also be used to derive the gamma-ray attenuation through the subject to improve the quality of the PET or SPECT image and to make it quantitative.

Positron Emission Tomography (PET) The tracers used in PET imaging contain a positron-emitting radionuclide (beta decay). When a positron is emitted, it travels through the body for a short distance (about 1 mm) until it interacts with an electron, and since it is its antiparticle this results in their mutual annihilation and production of two back-to-back gamma photons (going in opposite directions starting from the interaction point). The PET scanner contains a full ring of detectors surrounding the patient, and if two gamma photons are detected within a short time window it is assumed that they originate from the same point, and roughly speaking the line that connects the two photon detections should contain the point of origin (which we are trying to estimate). If we detect many of these gamma photons we get enough “lines” to be able to approximate the original activity distribution. The fact that no collimator is used makes the sensitivity of PET scanners much higher than SPECT, and the corresponding resolution is also better, especially in human imaging. To give an idea of the difference, a standard clinical PET system has a sensitivity of the order of $10^{-2}\,\mathsf{cps/Bq}$ for a $5\,\mathsf{mm}$ resolution, whereas a SPECT scanner gives a sensitivity in the order of $10^{-4}\,\mathsf{cps/Bq}$ for an $8-10\,\mathsf{mm}$ resolution. However, PET scanners are intrinsically limited by the positron range ($\sim 1\,\mathsf{mm}$), which becomes more significant as we go to smaller objects, such as in small-animal imaging. Another disadvantage is the fact that most PET radioisotopes are produced in cyclotrons, which have increased space and technical requirements (and accompanying costs), and the short half-life of the radioisotopes means that the cyclotron needs to be close to the PET scanner.

Single Photon Emission Computed Tomography (SPECT) SPECT makes use of gamma-emitting radioisotopes (gamma decay). The gamma-rays are detected using the so-called gamma camera of the scanner, which is composed by a collimator positioned in front of a radiation detector. The function of the collimator is to select the directions of the incident photons, since in this case we have the emission of a single photon per decay. The most common approach in SPECT imaging is to rotate the gamma camera around the subject, so that the photons are detected from a variety of directions. This information is then used to produce 3D images with the approximate distribution of the tracer. This thesis treats the improvement on SPECT imaging, so we will go into more detail on this modality and its characteristics for the remainder of this section.

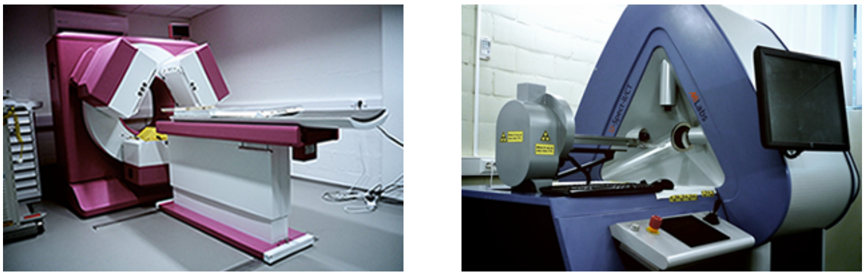

(a) (b)

Figure 1.6: Examples of SPECT imaging scanners. (a) The Triple Head human SPECT scanner Prism 3000 NewTec, from Inter Medical; it supports both parallel-hole and fanbeam collimators. (b) The stationary small animal SPECT/CT system U-SPECT II, from MILabs, which uses multi-pinhole collimation. [Images obtained from [7]]

1.2 Motivation

In this dissertation we put forward several developments in the field of SPECT. As explained before, SPECT is a nuclear imaging technique that provides 3-dimensional information on the metabolism and physiology of the body *in vivo* (functional imaging). This allows us for example to detect certain diseases early on, before anatomical changes take place.

SPECT imaging is commonly used in medicine and research, in areas such as oncology, cardiology, neurology and molecular imaging. Its use is normally divided into clinical and preclinical imaging, which corresponds to having humans or lab animals as subjects, respectively. SPECT is often used to image specific regions of interest within the imaging field of view, with special collimator designs that focus on that region and thus improve the image resolution in a way that is not feasible for other modalities. As such, the most wide-spread clinical applications of SPECT tend to be in the imaging of specific organs, such as the heart and the brain [8], and it is also a very important technique in preclinical imaging (mice and rats) [9, 10], where sub-millimeter resolution is now the standard. Compared to the alternative imaging modalities that also provide functional information of the body, such as PET and fMRI, SPECT is less costly and requires fewer technical and physical resources. Another advantage of SPECT is the existence and ease of access to many radiotracers for different purposes; the radioisotopes used come in a variety of energies, and have a relatively long half-life. Therefore, SPECT remains an important and competitive imaging modality with a lot of opportunities for innovation and improvement, either by itself or in combination with other medical imaging modalities.

Motivated by recent progress in manufacturing techniques, in this thesis we develop a new type of collimator for stationary SPECT imaging (i.e. no movement of the gamma camera). Being stationary gives it several advantages, in terms of size, stability, cost, maintenance, etc. Furthermore, the proposed design allows the scanner to be more compact than the currently available stationary SPECT systems. We explore several possible applications for this system, in both clinical and preclinical imaging, and discuss its properties in comparison to currently available SPECT systems.

Before we do this, however, we investigate and develop methods to help guide the design of such systems, and to accurately predict their performance. These methods can be divided in two closely related categories: system modeling and evaluation of image quality. System modeling refers to the computational modeling of the system's action during a scan, and the more accurate it is the better we are able to assess how the system will behave in reality, without having to build it first. This allows us to test many different system designs in a controlled and efficient way, in terms of both time and money, as well as improve the algorithms for image reconstruction and evaluation of image quality. Evaluation of image quality refers to the measurement of quantities (figures-of-merit) that indicate how well the system performs according to a given criterium. This allows us to compare several imaging systems to decide which will perform best on average, as well as compare different configurations and protocols of the same system. This research into tools for system modeling and evaluation of image quality is then used to support the investigation into the newly developed SPECT system.

1.3 Outline

In **Chapter 2** we introduce the essential background to frame the work in this dissertation. We start by a description of how a SPECT image acquisition works. Since this work deals with collimator design, we go into more details on the important collimator characteristics to be considered, with particular emphasis on pinhole and parallel-hole collimation. Following that, we explain the basics behind several techniques used throughout this thesis: image reconstruction, system modeling and image quality. The last two sections also provide the basis for the main developments in Chapters 3 and 4, respectively.

In **Chapter 3** we present an accurate and efficient analytical approach for modeling non-standard collimator geometries. We apply and validate it for two different categories of collimators with innovative shapes: those based on pinhole-like apertures (loftholes) and those based on parallel holes. For the lofthole collimators, formulas for the total point sensitivity are derived, and validated using a simple ray-tracer. In the case of the parallel-hole collimators, whose design corresponds to the new stationary SPECT systems proposed in this thesis, we describe how to compute the sensitivity of each detector bin to a point source, and we validate the method with realistic Monte Carlo simulations.

In **Chapter 4** we introduce several different approaches for the practical application of the Fisher Information Matrix-based evaluation of image quality in SPECT. These approaches have previously been described and used frequently in literature, especially the so-called local shift-invariant approach, but their accuracy has not been thoroughly tested. In this chapter we evaluate the performance of these different approaches and compare them to each other. This is done for two illustrative systems: a parallel-hole and a pinhole system. Based on these results, we then derive some general insights about the suitability of the approaches for the use in evaluation of image quality in SPECT.

In **Chapter 5** a novel collimator concept for stationary SPECT imaging is developed. We first introduce the general idea behind it, followed by the description of three systems that would use the proposed collimator concept in different applications. These three applications would be the imaging of a full human body, a human brain and a small animal. We evaluate the systems by simulating projection data and reconstructing it. In this first study, the sensitivity and resolution of the systems is evaluated, and we see if they are able to reconstruct artifact-free images. Chapters 6 and 7 then continue to build on the ideas and results presented in this chapter, and each focus on a specific system design for which the collimator concept presents particular advantage.

In **Chapter 6** we take the design proposed in Chapter 5 from human brain imaging and compare its performance with a standard clinical SPECT system. This comparison is done based on simulated reconstructions, as well as the Fisher Information Matrix-based method from Chapter 4. Although the simulations are ideal and simplified, they give indications as to the value of using the proposed stationary SPECT system design in clinical practice.

In **Chapter 7** an additional stationary SPECT design is proposed, this time for small-animal imaging. Its geometry is suited to fit a particular detector setup which is already available in our lab, so that we could easily test it experimentally. Similar evaluations to the previous chapters are performed, based on simulated projection data and reconstructions. Finally we also mention the development of a prototype based on this collimator design and show some initial experimental results.

Finally, in **Chapter 8** we summarize the results of this thesis. We discuss possible future directions for this research and make a general conclusion.

Chapter 2

Background

This chapter describes the background and fundamental principles from which the work in this thesis is derived. In Section 1.1 we have given a general overview of medical imaging and the most important modalities. In this chapter we will start in Section 2.1 with a more detailed explanation about SPECT imaging, which is the focus of the dissertation. In the following sections we address the most important concepts behind the work: collimation (Section 2.2), image reconstruction (Section 2.3), system modeling (Section 2.4) and evaluation of image quality (Section 2.5).

2.1 Single Photon Emission Computed Tomography (SPECT)

In SPECT, molecules labeled with a gamma-emitting radioisotope, commonly referred to as a tracer, are injected into the subject under study. The SPECT scanner measures gamma-rays originating from the decaying isotope using a radiation detector, and a collimator is positioned in front of the detector to select a certain direction of incidence of gamma-photons on the detector. Fig. 2.1 shows a diagram of how this process works. The combination of the detector and collimator is called a gamma camera, and it is the fundamental component of the SPECT scanner.

The gamma-ray detector is usually composed of a NaI(Tl) scintillator plate, which converts the gamma radiation into visible light. To stop photons with the standard gamma-ray energy used in SPECT, i.e. 140 keV, the plate has a standard thickness of 3/8". The scintillator is coupled to photomultiplier tubes (PMTs), which convert the light signal into electrical current and amplify it. To obtain the approximate position at which gamma photons were detected, Anger logic is applied to the light-spread in the PMTs.

The collimator, on the other hand, consists of a block of material with a high attenuation coefficient with respect to the emitted gamma-rays. The most commonly used materials are lead (Pb) and tungsten (W), due to their high stopping power and lower cost compared to the alternatives (materials such as gold and depleted uranium have also been used for small portions of collimators). In this material, small holes are provided to allow incidence of photons from a limited acceptance angle. There are several different types of collimators, with different advantages. Collimator design is a major part of this thesis, so a more detailed overview about the subject is given in Section 2.2.

By combining the information from the detector and the collimator, we can estimate the possible trajectories taken by each detected photon, and the corresponding probabilities. Due to the random nature of radioactive decay, the more photons we detect the more accurate this estimation will be.

In order to reconstruct a 3D image of the radioisotope distribution, each point in the distribution needs to be observed by the scanning system from a sufficient number of angles, and this is called sampling completeness. Sampling completeness is usually achieved by rotating the gamma-camera(s) around the subject, and stopping at certain angular positions to acquire data. What results is a set of 2D projections, each

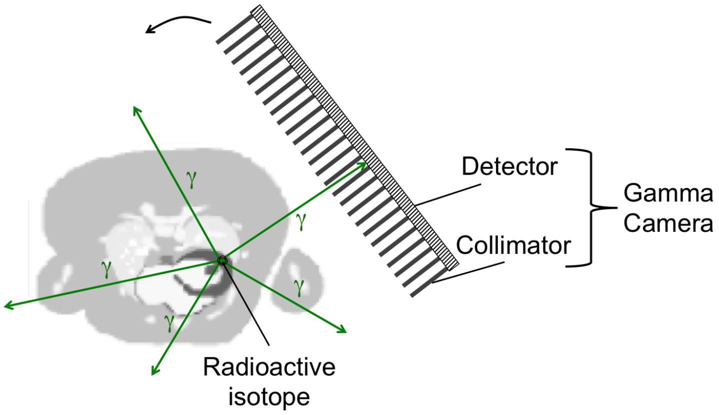

Figure 2.1: A schematic representation of how a SPECT scanner works.

corresponding to a different angular position of the camera. From the 2D projections and the model of the system acquisition, we are able to estimate the tracer distribution in the body by applying a so-called reconstruction algorithm (see Section 2.3).

2.2 Collimators

As explained in the previous section, the role of the collimator in the gamma-camera is to select the directions of incidence through which gamma photons can hit the detector. This is because the collimator material absorbs gamma radiation, so most of the photons that are able to hit the detector have passed through one of the holes in the collimator. There are several types of collimators, and in this dissertation we focus on two of the most common types: pinhole and parallel-hole collimation (see Sections 2.2.1 and 2.2.2 respectively).

There are three important concepts that distinguish collimator types: field of view (FOV), sensitivity and resolution. The choice of which collimator to use will depend on the restrictions we impose on the system, and will always involve a trade-off between these three properties.

FOV The FOV is the region of space which is “seen” by the collimator (i.e. from which photons can originate that hit the detector) at all angular positions of the gamma-camera. In other words, it corresponds to the points in space which we can accurately reconstruct (with full angular sampling).

Sensitivity The sensitivity of the collimator to a point-source is the ratio of the number of photons which are able to go through the collimator to the total number of photons emitted from that source. This value (so-called geometric sensitivity) is then multiplied by the detector efficiency to obtain the total sensitivity of the gamma-camera to the source.

Resolution The resolution is defined as the smallest distance between two points in the image-space such that they can be distinguished by the system. It is dependent on the distance between the points and the collimator (the longer the distance, the worse the resolution). The global resolution R has two components: the geometric resolution R_g,

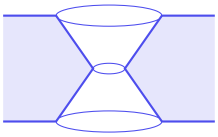

Figure 2.2: Schematic representation of a standard pinhole aperture.

which results from the collimator properties, and the intrinsic detector resolution R_D, which results from the limited capability of the detector to distinguish between rays arriving at points too close to each other.

2.2.1 Pinhole

The standard pinhole (knife-edge) has the shape of a sort of double cone, as shown in Fig. 2.2. A part of the image space is projected through the pinhole in a similar way to a camera obscura (see Fig. 2.3), such that the image seen in the detector is inverted with regards to the original object. Depending on the distance from the image to the pinhole (h) and from the detector to the pinhole (f), the image can be magnified or minified onto the detector, which corresponds to the magnification $m = f/h$ being greater or smaller than 1.

The geometric sensitivity g of a detection system with respect to a point source Src is defined as

$$g = \frac{\text{number of detected photons from the source}}{\text{total number of photons emmitted (isotropically) from the source}}.$$

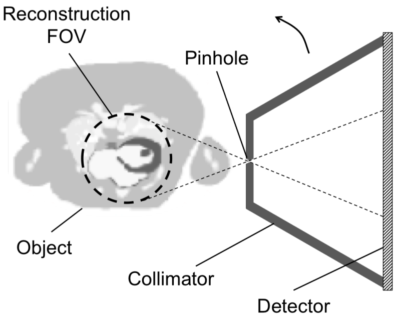

Figure 2.3: Schematic representation of a single pinhole collimator imaging a region of interest in the object.

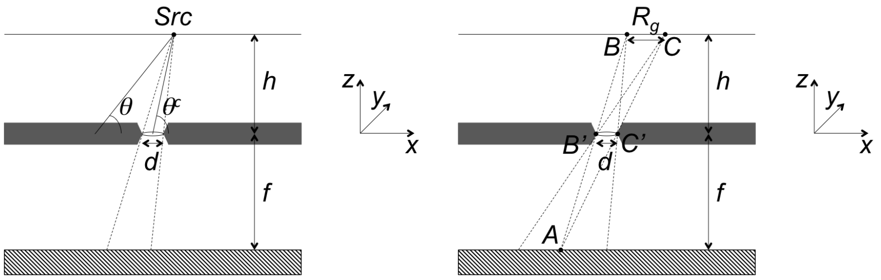

(a) (b)

Figure 2.4: Schematic representation of a standard pinhole aperture and detector, showing the meaning of the variables used in equations (2.2) and (2.3). The subfigures (a) and (b) refer to the sensitivity and resolution calculations, respectively.

If we consider a single pinhole aperture, and we assume that all photons passing through the collimator aperture hit the detector, this value can be computed as

$$g = \frac{1}{4\pi} \iint_{aperture} d\Omega = \frac{1}{4\pi h^2} \iint_{aperture} \sin^3 \left[\theta(x, y)\right] dxdy, \tag{2.1}$$

where $d\Omega$ is the solid angle that an infinitesimal element of the aperture subtends at the point source, 4π is the total solid angle subtended at the source, $\theta(x, y)$ is the incidence angle of a photon on the aperture plane at the infinitesimal aperture element $dxdy$ and h is the perpendicular distance from the source to the aperture plane (see Fig. 2.4. (a)). As is mostly done in literature [11] and in practice, we assume that for a given point source $\theta(x, y) \approx \theta(0, 0) = \theta$ for all $(x, y) \in A_{int}$, which is usually a good approximation. Then, expression (2.1) becomes

$$g \approx \frac{A_{aperture} \sin^3 \theta^c}{4\pi h^2} = \frac{d^2 \sin^3 \theta^c}{16 h^2} \tag{2.2}$$

where $A_{aperture}$ is the area of the aperture, $\theta^c = \arctan\left(\frac{h}{x}\right)$ is the incidence angle of a photon at the center of the aperture and d is the aperture diameter.

The geometric resolution R_g is the distance between two point sources whose projection circles touch each other at the edge. An example of two such points (B and C) can be seen in Fig. 2.4. (b). The distance

R_g can be computed due to the similarity of the two triangles $\triangle ABC$ (of base R_g and height $h+f$) and $\triangle AB'C'$ (of base d and height f), which implies

$$\begin{aligned} \frac{R_g}{h+f} &= \frac{d}{f}, \\ R_g &= \frac{d}{f}(h+f)\,. \end{aligned} \tag{2.3}$$

Note that expression (2.3) shows that the only variable value on which R_g depends is h, the perpendicular distance to the plane of the pinhole aperture. In particular, the resolution improves if h decreases, i.e. if we come closer to the collimator. We then compute R, the global resolution, as

$$R \approx \sqrt{R_g^2 + \left(\frac{R_D}{m}\right)^2},$$

where R_D is the intrinsic detector resolution and $m = f/h$ is the magnification. Note that the magnification mode ($m > 1$) allows us to reduce the effect of the intrinsic detector resolution on the projection, but the system becomes larger (we usually need to increase f), and with minification ($m < 1$) the opposite happens.

To model the effect of collimator penetration, the aperture diameter d in equations (2.2) and (2.3) can be replaced by an effective diameter [12]

$$d_e \approx \left[d\left(d + \frac{2}{\mu}\tan\frac{\alpha}{2}\right)\right]^{1/2},$$

where μ is the attenuation coefficient for the collimator material and α is the pinhole's opening angle.

The sensitivity-resolution trade-off in pinhole collimators is most advantageous for imaging small regions of interest (using the magnification effect) close to the collimator. This is because both resolution and sensitivity ((2.2) and (2.3)) improve as h approaches 0, but this also makes the FOV smaller (see Fig. 2.3). The magnification effect allows us to surpass the intrinsic detector resolution, and achieve ultra-high resolution imaging of small objects. As such, pinhole SPECT systems are often

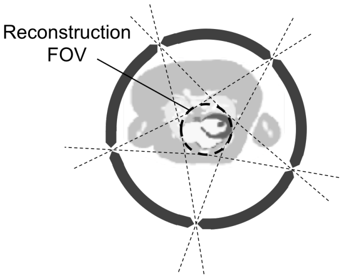

Figure 2.5: Schematic representation of a stationary multi-pinhole collimator and corresponding FOV.

used for small-animal (mice and rats) imaging [13, 14, 15, 16, 17, 18], and also in imaging of specific human organs, such as the heart [19, 20, 21], the thyroid [22, 23] and the brain [24, 25]. This can either be done with a rotating pinhole camera (Fig. 2.3), with one or more pinholes, or with a multi-pinhole stationary collimator (Fig. 2.5). The advantages of a stationary system compared to a rotation-based system are that it does not require large and expensive rotation mechanisms, it has simple mechanics (table translation) and is easy to calibrate, thereby avoiding rotation-related degradation of image quality and system idle time due to its mechanical motion. On the other hand, its FOV is fixed, and the magnification cannot be increased by placing the collimator closer to the object. A more detailed discussion on the advantages and disadvantages between these two types of imaging is done in Chapter 6.

2.2.2 Parallel-hole

In a parallel-hole collimator (Fig. 2.6), the apertures are long thin holes, closely packed and oriented parallel to each other. The collimator material between two aperture holes is called a septum. Since this type of collimator only accepts photons that hit the detector in trajectories of (roughly) the same direction as the holes, the projection of the object is not magnified or minified. As shown in Fig. 2.6, the diameter of the FOV is then equal to the detector size. Also note that when using parallel-hole collimators the transaxial FOV is given by the circle inscribed by the trajectory of the gamma-camera(s).

The geometric sensitivity g of a standard parallel-hole system with

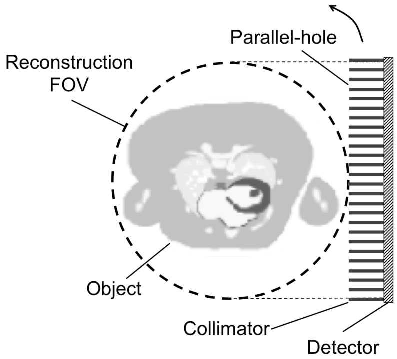
Parallel-hole
Reconstruction FOV
Object
Collimator
Detector

Figure 2.6: Schematic representation of a parallel-hole collimator imaging the object.

respect to a point source *Src* can be shown to be given by

$$g = \left(\frac{Kd^2}{a(d+t)}\right)^2 \tag{2.4}$$

with K a factor that depends on the hole geometry, d the hole width, t the septal thickness and a the hole height (see Fig. 2.7. (a)). For the full derivation we refer the reader to [26, 27]. In the case of square holes in a square grid, the geometry used in this thesis, the geometric factor

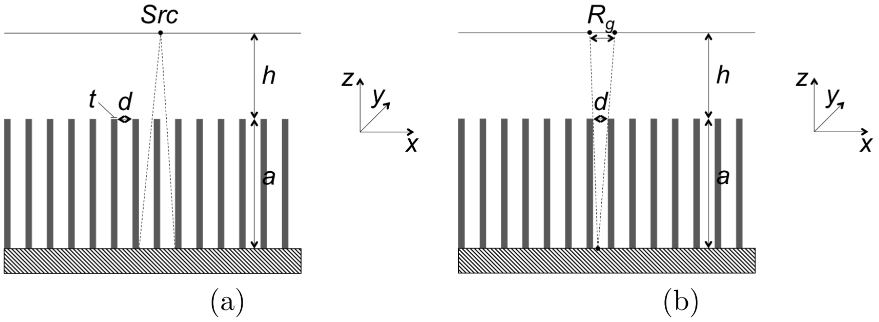
Src
t
d
h
a
z
y
x
(a)
R_g
d
h
a
z
y
x
(b)

Figure 2.7: Schematic representation of a parallel-hole collimator and detector, showing the meaning of the variables used in equations (2.4) and (2.5). The subfigures (a) and (b) refer to the sensitivity and resolution calculations, respectively.

is given by [28, 27]

$$K = \frac{1}{\sqrt{4\pi}}.$$

Note that (2.4) depends only on the collimator geometry and not on the distance of the point source to the collimator. This can be intuitively understood from the fact that as a point source moves further away from the collimator the sensitivity per collimator aperture will decrease but more apertures will be covered (a larger area of the detector is irradiated but at a lower intensity per detector pixel).

The geometric resolution R_g can be computed in the same way as in Section 2.2.1 for a pinhole collimator, by triangle similarity (see Fig. 2.7. (b)), and we get

$$R_g = \frac{d}{a}\left(h + a\right). \tag{2.5}$$

Note that again here the resolution improves as the object comes closer to the collimator. Since there is no magnification, we compute the global resolution R as

$$R \approx \sqrt{R_g^2 + R_D^2}. \tag{2.6}$$

To model the effect of collimator penetration, the hole height a is replaced by an effective height a_e in equations (2.4) and (2.5), determined by the attenuation coefficient μ as $a_e = a - 2/\mu$ [12].

When designing a parallel-hole collimator to achieve a given target resolution, the hole height a and diameter d are chosen according to (2.5) and (2.6). Once those values are determined, the septal thickness t that results in a given maximum amount of penetration β (usually 5%) is computed using [26]

$$t = \frac{2dw}{a - w}, \tag{2.7}$$

where $w = -(\ln\beta)/\mu$ is the length of the path of minimum attenuation through the septum.

Parallel-hole collimators are more commonly used for clinical imaging (imaging of humans), due to the ability to image a larger volume (FOV) compared to the size of the system. The absence of the magnification effect implies that when coming very close to the collimator (small h) the intrinsic resolution factor R_D becomes dominant in expression (2.6), which limits how good the resolution can get. In terms of the system geometry, from expressions (2.4) and (2.5) we get the following approximated expressions assuming $h \ggg a$ (far field) and $t \approx 0$:

$$g \approx \left(\frac{Kd}{a}\right)^2, \qquad R_g \approx \frac{dh}{a},$$

which means that if we change the system parameters d and a to improve the resolution (lower R_g value) this results in a quadratic decrease in sensitivity. So, as would be expected, improvement of either resolution or sensitivity results in a worsening of the other property.

2.2.3 Production Techniques and Novel Collimator Designs

In this subsection we focused on two standard types of collimators: pinhole (Section 2.2.1) and parallel-hole (Section 2.2.2). For a more detailed overview of the different types of standard collimators (fanbeam, conebeam, slit-slat...) in SPECT and discussions on collimator design and optimization, the reader is referred to [29, 28, 30].

In theory, many different, non-standard, collimator designs are possible, but this is necessarily limited by the production techniques. Two easy and low cost techniques, which can only be used with lead, are molding and stacked foil sheets. Of these two techniques, pinhole collimators can only be produced with the first method (molding), whereas both can be used to produce parallel-, fan-, cone-, and diverging-beam collimators. With these techniques we are able to produce collimators with hole diameters as small as 1.2 mm and septa of 0.15 mm [30], but for higher resolution collimators other techniques are required, such as X-ray lithography combined with metal electroforming [31], or stacking photochemically etched tungsten foils [32]. For pinhole collimators, on the other hand, there is also the option of introducing the aperture holes in the block of material by drilling, milling, or electric discharge machining (EDM). The latter techniques are, however, much more expensive, and still do not allow designs with more complex shapes, holes with large tilt angles or very small opening angles in pinholes. In order to be able to produce a wider variety of geometries, our research group MEDISIP (Medical Imaging and Signal Processing Group of Ghent University) has been at the forefront of the use of Additive Manufacturing

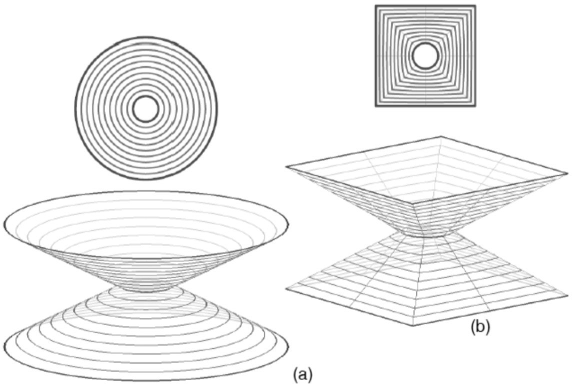

Figure 2.8: Schematic representation of a standard pinhole (a) and a lofthole with square entrance and exit openings (b). In both cases a top and a side view is shown. Figure from [37].

for collimator production [33, 34]. This is a 3D Printing technique in which a thin layer of metal powder is laid down on a horizontal plane, then a laser selectively melts the parts which will form the collimator, and afterwards a new layer of powder is added on top and the process is repeated until the product is complete. The unwanted parts (those that should not be filled) remain in powder form and are removed after the process.

With these new techniques for collimator design, new types of collimator have been proposed. MEDISIP has been especially active on the design of novel, cutting-edge SPECT scanners. In particular, innovative collimator designs have been developed to improve the performance of the scanners for particular purposes, such as compact small-animal imaging [18], high-resolution brain imaging [35] and simultaneous SPECT and MRI imaging [36]. An especially important development for small-animal SPECT imaging has been the lofthole collimator [37], where the aperture holes are similar to pinholes but have non-circular entrance and exit openings, allowing a more efficient use of the (limited) detector space (see Fig. 2.8). In this dissertation we also propose a novel type of collimator geometry, based on parallel-holes with a varying angular alignment and non-traditional shapes for the collimator body (Chapter 5). The main motivation behind the development of this collimator geometry was to allow for a stationary SPECT system (with the advantages mentioned in Section 2.2.1) with an enlarged FOV (in proportion to the size of the entire system) as compared to the existing multi-pinhole stationary systems.

The development of these new collimator geometries requires appropriate modeling. In particular, the expressions for collimator sensitivity and resolution derived in sections 2.2.1 and 2.2.2 are no longer valid. As such, in Chapter 3 we derive generalizations of expressions (2.2) and (2.4) for non-standard collimator geometries.

2.3 Image Reconstruction

In the previous sections we have described the basic principles behind the functioning of SPECT scanners, and the collimator component in particular. The final data from a scan is a set of 2D images, corresponding to projections along different angles with regards to the object. With these projections we then need to obtain a 3D image of the radioisotope distribution, for which we need a model of the SPECT system (sections 2.2 and 2.4) and a reconstruction algorithm. In this section we will describe the general idea behind reconstruction algorithms and those which are of particular interest for this dissertation.

2.3.1 The Imaging Problem

There are three main components to the imaging problem in SPECT: the image, the projection, and the system response. The image, $\mathbf{f}$, is a mathematical representation of the true radioisotope distribution in the object which is being scanned; in practice, we do not know what the true image is, and the goal of image reconstruction is to find an approximation to this image, $\hat{\mathbf{f}}$, as accurate as possible. The projection, $\mathbf{g}$, is what is measured by the detector; this is what we always know in a real experiment, and what we try to predict in a simulation of the system. Finally, the system response is the model we use to convert the image into the projection data.

The detector measurements, also referred to as projection or as sinogram, are generally represented by a random vector $\mathbf{g} \in \mathbb{R}^{M \times 1}$, where $M =$ number of pixels in one detector × number of detectors × number of rotation angles of the camera. For i corresponding to a fixed rotation angle, detector and pixel, the vector element g_i is the total number of photons that have hit that particular pixel area in the detector during the time period in which the gamma-camera was at that position.

The image is, in reality, a continuous function $f(x, y, z)$, representing the γ-ray emission rates (the activity) of the underlying object at each (x, y, z) coordinate in image-space. However, in practice, when treating SPECT image reconstruction the standard approach nowadays is to discretize the $3D$ image-space into N cubic voxels, and then represent it by vector $\mathbf{f} \in \mathbb{R}^{N \times 1}$. This discretization step is unavoidable in particular to represent the image computationally, but other basis functions besides the usual cubic voxel can be chosen [38, 39]. The vector element f_j is then the amount of activity contained in the volume of the jth voxel. Note that the object being imaged can be a biological entity or an imaging phantom, which is an object specifically designed to either simulate the body of a biological entity or to evaluate the system's performance (e.g. resolution).

Finally, in this formulation of the imaging problem the SPECT system response has the form of an $M \times N$ system matrix, $\mathbf{H}$. Each element H_{ij} of the system matrix represents the probability that a gamma photon originating from voxel j has of being detected by detector pixel i. In Section 2.4 we will explain how this can be done in more detail.

From the definition of the system matrix $\mathbf{H}$, it follows that by applying it to $\mathbf{f}$ we obtain the mean value predicted for the projection data, i.e.

$$\overline{\mathbf{g}}(\mathbf{f}) = \mathbf{Hf}. \tag{2.8}$$

The operation of multiplying $\mathbf{H}$ by an image is called a "projection", and the application of its transpose $\mathbf{H}^T$ to a projection vector is called a "backprojection".

2.3.2 Iterative Reconstruction

Two main classes of image reconstruction algorithms exist: analytical and iterative. For an overview of the most important methods for SPECT reconstruction in these two categories the reader can see for example [40], and for a more in-depth explanation Chapters 20 and 21 of [41].

The idea behind analytical reconstruction algorithms is to find an exact mathematical solution to the imaging problem. The most popular analytical reconstruction method is the Filtered BackProjection (FBP) algorithm [42], based on the inversion of the Radon transform. Such methods are generally easy to implement and fast to compute, but they are based on several simplified assumptions about the system: that it is perfectly modeled (there is limited capacity to incorporate correction methods), that the angular sampling is continuous (or, in practice, that a high number of angles is used), that the projection data used is noiseless... This significantly limits their accuracy, and introduces image-degrading artifacts, but in the earlier days of SPECT it was the standard approach.

In iterative reconstruction, on the other hand, we solve the imaging problem by starting with an initial estimation of the image, $\hat{\mathbf{f}}_0$, and successively updating it such that in the limit it should get closer and closer to the true image (speaking in simplified terms). The method allows us to model the imaging process more accurately and to account for the inaccuracies in the modeling and the stochastic nature of the processes that occur (namely, radioactive decay). Iterative algorithms are more computationally intensive than analytical reconstruction methods, since each iterative step usually involves calculations of similar or greater mathematical complexity as the single step done in an analytical counterpart. However, nowadays, with significant improvements in computational power, they have become the standard in SPECT reconstruction. The more realistic the modeling of the imaging process, the more the computational complexity increases, but also the more accurate the final image estimates should be.

In this dissertation our focus is on statistical iterative reconstruction methods, i.e. methods that take a statistical model of the measured data into account. The idea is to find the mean activity values in $\mathbf{f}$, which is what we actually want to estimate, instead of the particular instance (number of emissions per voxel) which is observed in that particular experiment. In particular, we will explain two of the most used algorithms in SPECT: MLEM (Section 2.3.3) and PML (Section 2.3.4). The detector measurements $\mathbf{g}$ will be described as conditionally independent Poisson random variables, resulting from the fact that the radioactive disintegrations from which the detected gamma-photons originate, as well as the particle interactions, are themselves Poisson processes [43, 44]. As such, we will assume a conditional probability $p(\mathbf{g}|\mathbf{f})$ as

$$p(\mathbf{g}|\mathbf{f}) = \prod_{i=1}^{M} \frac{(\overline{g}_i(\mathbf{f}))^{g_i} \, e^{-\overline{g}_i(\mathbf{f})}}{g_i!}, \tag{2.9}$$

where $\overline{\mathbf{g}}$ is given by (2.8).

2.3.3 MLEM

The Maximum Likelihood Estimation Maximization (MLEM) algorithm [45, 46] is the basis of most reconstruction algorithms currently used for SPECT reconstruction. As the name indicates, it is based on finding the estimation $\hat{\mathbf{f}}$ that maximizes the likelihood that data set $\mathbf{g}$ (which we measure in an experiment) results from an underlying image $\mathbf{f}$, given by (2.9). This is equivalent to maximizing the logarithm of the likelihood, which we call the log-likelihood function $L(\mathbf{g}|\mathbf{f})$,

$$\begin{aligned} L(\mathbf{g}|\mathbf{f}) &:= \log p(\mathbf{g}|\mathbf{f}) \\ &= \log \left[\prod_{i=1}^{M} \frac{(\overline{g}_i(\mathbf{f}))^{g_i} \, e^{-\overline{g}_i(\mathbf{f})}}{g_i!} \right] \\ &= \sum_{i=1}^{M} \left(g_i \log \overline{g}_i(\mathbf{f}) - \overline{g}_i(\mathbf{f}) - \log g_i! \right) \\ &= \sum_{i=1}^{M} \left(g_i \log \left(\sum_{j=1}^{N} H_{ij} f_j \right) - \sum_{j=1}^{N} H_{ij} f_j - \log g_i! \right) \end{aligned} \tag{2.10}$$

where we replaced $p(\mathbf{g}|\mathbf{f})$ by (2.9) and $\overline{g}_i(\mathbf{f})$ by (2.8).

As explained before, the MLEM estimate $\hat{\mathbf{f}}_{MLEM}$ is given by

$$\hat{\mathbf{f}}_{MLEM}(\mathbf{g}) = \arg\max_{\mathbf{f} \geq 0} L(\mathbf{g}|\mathbf{f}). \tag{2.11}$$

Expression (2.11) cannot be transformed into a closed form mathematical expression to derive $\mathbf{f}$ from $\mathbf{g}$, and so we need to find an iterative rule to obtain $\hat{\mathbf{f}}$. To find the maximum of $L(\mathbf{g}|\mathbf{f})$ we compute the zero of its derivative, i.e.

$$\begin{aligned} \frac{\partial L(\mathbf{g}|\mathbf{f})}{\partial f_j} &= 0, \\ \sum_{i=1}^{M} \left(g_i \frac{H_{ij}}{\sum_{j'=1}^{N} H_{ij'} f_{j'}} - H_{ij} \right) &= 0, \\ \sum_{i=1}^{M} \left(g_i \frac{H_{ij}}{\sum_{j'=1}^{N} H_{ij'} f_{j'}} \right) &= \sum_{i=1}^{M} H_{ij}, \end{aligned}$$

$$\frac{1}{\sum_{i=1}^{M} H_{ij}} \sum_{i=1}^{M} \left(g_i \frac{H_{ij}}{\sum_{j'=1}^{N} H_{ij'} f_{j'}} \right) = 1,$$

$$\frac{f_j}{\sum_{i=1}^{M} H_{ij}} \sum_{i=1}^{M} \left(g_i \frac{H_{ij}}{\sum_{j'=1}^{N} H_{ij'} f_{j'}} \right) = f_j.$$

We can convert this formula into the following iterative rule [46]

$$\hat{f}_j^{(k+1)} = \frac{\hat{f}_j^{(k)}}{\sum_{i=1}^{M} H_{ij}} \sum_{i=1}^{M} \left(\frac{g_i}{\sum_{j'=1}^{N} H_{ij'} \hat{f}_{j'}^{(k)}} H_{ij} \right), \tag{2.12}$$

where $\hat{f}_j^{(k)}$ represents the estimated activity at voxel j at iteration k. This equation should be applied to each voxel of $\hat{\mathbf{f}}^{(k+1)}$. Intuitively we can see that the closer $\hat{\mathbf{f}}^{(k)}$ is to the true image, the closer its forward projection should be to the measured data, so if $\frac{g_i}{\sum_{j'=1}^{N} H_{ij'} \hat{f}_{j'}^{(k)}} \to 1$ then $\hat{f}_j^{(k+1)} \to \frac{\hat{f}_j^{(k)}}{\sum_{i=1}^{M} H_{ij}} \sum_{i=1}^{M} H_{ij} = \hat{f}_j^{(k)}$.

Now we describe how the implementation of the MLEM algorithm works in practice (Fig. 2.9). We start with an initial estimate $\hat{\mathbf{f}}^{(0)}$, which can, for example, have simply a uniform value within the FOV, or be an initial estimate of the image obtained by e.g. FBP. This estimate is then updated at each iteration k by performing the following steps

1. Forward project $\hat{\mathbf{f}}^{(k)}$: $\sum_{j'=1}^{N} H_{ij'} \hat{f}_{j'}^{(k)}$;

2. Compute the ratio of the measured projection data with the forward projection of the estimate (computed in Step 1), element by element: $\frac{g_i}{\sum_{j'=1}^{N} H_{ij'} \hat{f}_{j'}^{(k)}}$;

3. Backproject the ratio computed in Step 2 (which has projection-space dimensions): $\sum_{i=1}^{M} \left(\frac{g_i}{\sum_{j'=1}^{N} H_{ij'} \hat{f}_{j'}^{(k)}} H_{ij} \right)$;

4. Normalize the correction term computed in Step 3, with an element-wise division by a backprojection of a uniform projection of ones ($\sum_{i=1}^{M} H_{ij}$): $\frac{\sum_{i=1}^{M} \left(\frac{g_i}{\sum_{j'=1}^{N} H_{ij'} \hat{f}_{j'}^{(k)}} H_{ij} \right)}{\sum_{i=1}^{M} H_{ij}}$;

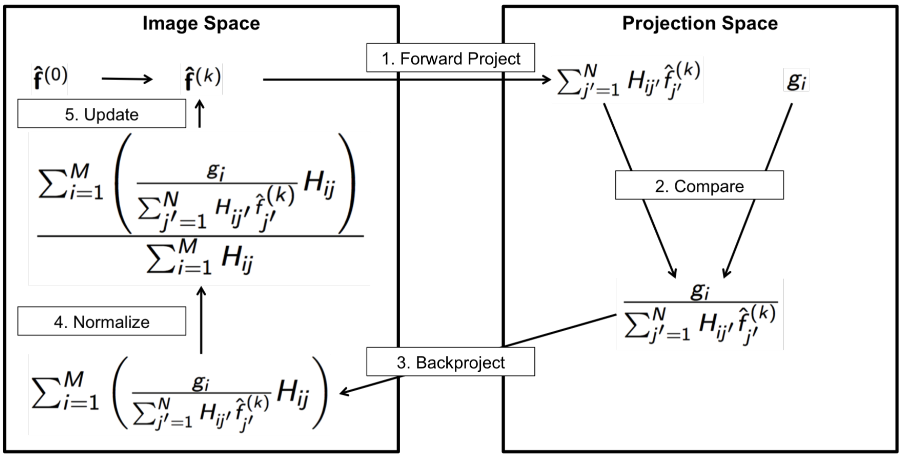
Image Space
Projection Space
$\hat{\mathbf{f}}^{(0)} \longrightarrow \hat{\mathbf{f}}^{(k)}$
1. Forward Project
$\sum_{j'=1}^{N} H_{ij'}\hat{f}_{j'}^{(k)}$
g_i
2. Compare
$\frac{g_i}{\sum_{j'=1}^{N} H_{ij'}\hat{f}_{j'}^{(k)}}$
3. Backproject
$\sum_{i=1}^{M}\left(\frac{g_i}{\sum_{j'=1}^{N} H_{ij'}\hat{f}_{j'}^{(k)}} H_{ij}\right)$
4. Normalize
$\frac{\sum_{i=1}^{M}\left(\frac{g_i}{\sum_{j'=1}^{N} H_{ij'}\hat{f}_{j'}^{(k)}} H_{ij}\right)}{\sum_{i=1}^{M} H_{ij}}$
5. Update

Figure 2.9: Schematic representation of the steps performed during an implementation of the MLEM algorithm.

5. Multiply $\hat{\mathbf{f}}^{(k)}$ with the term computed in Step 4, element-by-element: $\hat{f}_j^{(k+1)} = \frac{\hat{f}_j^{(k)}}{\sum_{i=1}^{M} H_{ij}} \sum_{i=1}^{M}\left(\frac{g_i}{\sum_{j'=1}^{N} H_{ij'}\hat{f}_{j'}^{(k)}} H_{ij}\right)$.

The fact that the detector measurements $\mathbf{g}$ are noisy means that the MLEM image estimation $\hat{\mathbf{f}}_{MLEM}$ will also be noisy, in order to fit the noisy data, and this introduces instabilities: the algorithm tends to amplify the noise with each iteration [47, 48] (see Fig. 2.10). To control this effect, the common procedure is to either stop the algorithm when it reaches a given limit for the noise level [49, 50, 47] or to let it run to

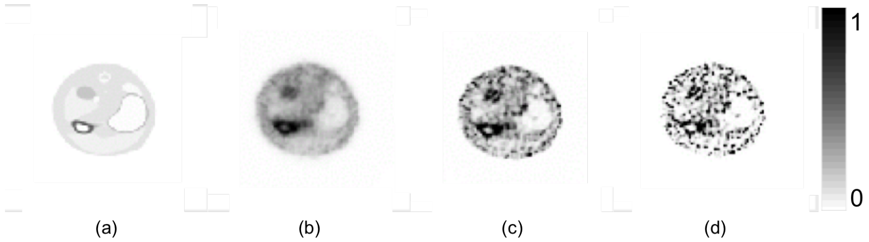

Figure 2.10: Images obtained from simple MLEM reconstruction, at different number of iterations. (a) Original phantom; (b) reconstructed image at iteration 10; (c) reconstructed image at iteration 50; (d) reconstructed image at iteration 200. One can see that the images become increasingly plagued by high-frequency noise as the number of iterations increases.

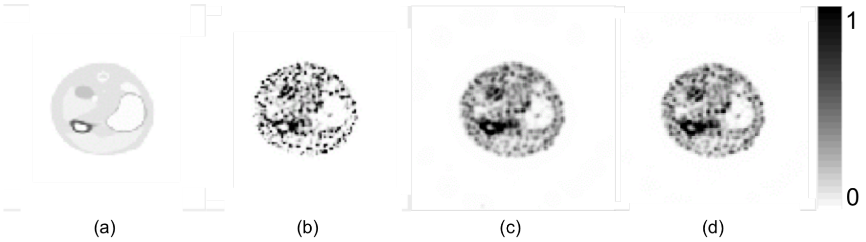

Figure 2.11: Final reconstruction images obtained from different reconstruction algorithms. (a) Original phantom; (b) reconstructed image at iteration 200, using simple MLEM reconstruction; (c) reconstructed image at iteration 200, using simple MLEM reconstruction followed by Gaussian filtering; (d) reconstructed image at iteration 200, using PML reconstruction (uniform quadratic penalty, first-order neighborhood).

convergence and then smooth the image out using a filtering operator [51, 52] (see an example in Fig. 2.11. (c)), represented by an $N \times N$ matrix $\mathbf{P}$

$$\hat{\mathbf{f}}_{PF-MLEM}(\mathbf{g}) = \mathbf{P}\hat{\mathbf{f}}_{MLEM}(\mathbf{g}).$$

The algorithm described in the next subsection was also developed to produce images with less noise (Fig. 2.11. (d)).

2.3.4 PML

The Penalized Maximum Likelihood (PML) algorithm [53], also referred to as Maximum A Posteriori (MAP), follows the same basic principle of MLEM but introduces prior information about the image to reduce noise and favor convergence (so-called regularization). The prior usually assumes that the true image is smooth (not very noisy).

The prior is introduced using Bayes' Theorem:

$$p(\mathbf{f}|\mathbf{g}) = \frac{p(\mathbf{g}|\mathbf{f})p(\mathbf{f})}{p(\mathbf{g})},$$

where $p(\mathbf{f}|\mathbf{g})$ is the image's a posteriori probability distribution, which this algorithm wants to maximize. $p(\mathbf{g}|\mathbf{f})$ has been defined in (2.9); $p(\mathbf{f})$ is the function that contains prior knowledge about the image, usually given by $p(\mathbf{f}) = Ce^{-\beta R(\mathbf{f})}$ (Gibbs prior, used to enforce local smoothness), where β is the weight of the regularization, $R(\mathbf{f})$ is the penalty function and C a constant value; $p(\mathbf{g})$ is the projection data's a priori probability, independent of $\mathbf{f}$. In this case the image estimator $\hat{\mathbf{f}}$ becomes

$$\hat{\mathbf{f}}_{PML}(\mathbf{g}) = \arg\max_{\mathbf{f}\geq 0}\left[p(\mathbf{f}|\mathbf{g})\right] = \arg\max_{\mathbf{f}\geq 0}\left[L(\mathbf{g}|\mathbf{f}) - \beta R(\mathbf{f})\right]. \tag{2.13}$$

As in Section 2.3.3, to compute (2.13) we equate to zero the derivative of the logarithm of the probability function

$$\begin{aligned} \frac{\partial \log p(\mathbf{f}|\mathbf{g})}{\partial f_j} &= 0, \\ \frac{\partial \log p(\mathbf{g}|\mathbf{f})}{\partial f_j} + \frac{\partial \log p(\mathbf{f})}{\partial f_j} - \frac{\partial \log p(\mathbf{g})}{\partial f_j} &= 0, \\ \sum_{i=1}^{M}\left(g_i \frac{H_{ij}}{\sum_{j'=1}^{N} H_{ij'} f_{j'}} - H_{ij}\right) - \beta\frac{\partial R(\mathbf{f})}{\partial f_j} - 0 &= 0, \end{aligned}$$

and performing similar steps to what was done in Section 2.3.3 we finally get the iterative rule [53]

$$\hat{f}_j^{(k+1)} = \frac{\hat{f}_j^{(k)}}{\sum_{i=1}^{M} H_{ij} + \beta\frac{\partial R(\hat{\mathbf{f}}^{(k)})}{\partial f_j}} \sum_{i=1}^{M}\left(\frac{g_i}{\sum_{j'=1}^{N} H_{ij'} \hat{f}_{j'}^{(k)}} H_{ij}\right). \tag{2.14}$$

The implementation of the PML algorithm follows a similar sequence as described for MLEM, with the additional step that we need to compute $\frac{\partial R(\hat{\mathbf{f}}^{(k)})}{\partial f_j}$, which depends on the penalty function $R(\mathbf{f})$ chosen. The typical functions result in a penalization of the differences in intensity of neighboring voxels [54, 55, 56]. One of the simplest functions, which is the one used in this thesis, is the uniform quadratic penalty [57]

$$R(\mathbf{f}) = \sum_{j=1}^{N}\sum_{k\in N_j} \frac{w_{jk}}{4}\left(f_j - f_k\right)^2 \tag{2.15}$$

where N_j is the set of pixels in a certain neighborhood of voxel j and the parameter w_{jk} is symmetric ($w_{jk} = w_{kj}$). Equation (2.15) can also be written as

$$R(\mathbf{f}) = \frac{1}{2}\mathbf{f}^T\mathbf{R}\mathbf{f} \tag{2.16}$$

with $\mathbf{R}$ the Hessian matrix of $R(\mathbf{f})$, with components

$$\mathbf{R}_{jk} = \begin{cases} \sum_{l \in N_j} w_{jl}, & k = j \\ -w_{jk}, & k \neq j \end{cases}. \tag{2.17}$$

For (2.14) we need the derivative of (2.15), which is

$$\frac{\partial R(\mathbf{f})}{\partial f_j} = \sum_{k \in N_j} w_{jk} \left(f_j - f_k \right). \tag{2.18}$$

To understand how using such a prior favors smoother image estimations, we can look at equation (2.18). If the image is already smooth, i.e. $f_j \approx f_k$, then $\partial R(\mathbf{f})/\partial f_j \approx 0$ and the algorithm becomes the standard MLEM ((2.14) becomes close to (2.12)). If the neighbors surrounding voxel j have on average higher values than j, then $\partial R(\mathbf{f})/\partial f_j < 0$, resulting in a decrease in the denominator in expression (2.14) and an increase in the value of $\hat{f}_j^{(k+1)}$ compared to $\hat{f}_j^{(k)}$, thereby getting the estimated value closer to the value of its neighbor voxels. When the value at voxel j is higher than its neighbors, then the opposite happens. Since in (2.14) the $\partial R(\mathbf{f})/\partial f_j$ term is multiplied by the regularization parameter β, the larger we set this value the smoother the final estimation will be, which means it will be less noisy but also more blurry. After obtaining $\hat{\mathbf{f}}_{PML}$, the noise in the estimation can be further smoothed out (if required) using a filtering operator, and the final post-filtered penalized maximum likelihood (PF-PML) estimation is written as

$$\hat{\mathbf{f}}_{PF-PML}(\mathbf{g}) = \mathbf{P}\hat{\mathbf{f}}_{PML}(\mathbf{g}). \tag{2.19}$$

In the most simple case, first-order neighborhood, only the nearest neighbors are included in N_j, and the conventional choice is to set [58]

$$\begin{cases} w_{jk} = 1, & k \in N_j \\ w_{jk} = 0, & k \notin N_j \end{cases}.$$

In 3D each voxel has 6 nearest neighbors, and so equation (2.17) becomes

$$\mathbf{R}_{jk} = \begin{cases} 6, & k = j \\ -1, & k \neq j \end{cases}.$$

In Section 2.5 we will describe an analytical method for evaluation of image quality of reconstructions using the PF-PML algorithm, which will later be used in Chapters 4 and 6.

2.4 System Modeling

The modeling of a SPECT system's response is crucial for two main purposes: the projection/backprojection operations (multiplication by $\mathbf{H}/\mathbf{H}^T$) during image reconstruction (Section 2.3) and producing simulated projection data $\mathbf{g}$. The more accurate the modeling, the better the reconstruction outcome [59, 60] and the more realistic the simulation. In sections 2.4.1 to 2.4.3 we will describe the three most commonly used methods for modeling the system, in increasing order of accuracy: Analytical, Monte Carlo and Experimental derivation.

Note that in this section we only consider the modeling of system response, and not the effect of gamma photons being absorbed or scattered within the body being scanned. These are referred to as attenuation and scatter effects, and they are usually taken into account in SPECT reconstructions/simulations. They are dependent on the specific phantom being imaged (its shape, size and composition), which complicates their implementation and makes the reconstruction take longer. For this reason, and because including these effects would not alter the analysis and conclusions in this dissertation significantly, attenuation and scatter are not modeled. For a detailed description on attenuation and scatter correction, see for example [41].

2.4.1 Analytical Methods

An analytical or algebraic method basically consists of a mathematical formulation of the projection and backprojection operations that does not involve any random elements (it is deterministic). For this we need to model the phantom and the gamma camera geometries, as well as the gamma-rays and their interaction with the materials they come in contact with before possibly being detected.

A very simple and fast approach that can be used to obtain a rough estimation of the projection, in the case of parallel-hole collimation, is to obtain the projection as the sum of all voxels in each row (possibly with weights to model the different sensitivity values), as schematically shown in Fig. 2.12 for one row of voxels. To obtain the projections for

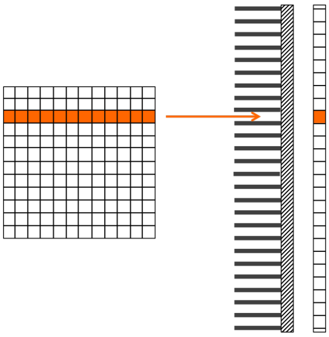

Figure 2.12: Schematic representation in 2D of the voxelized image space, the gamma camera (based on parallel-hole collimation) and the projection bins. In a very simple projection model, the values of the voxels in the highlighted row would be summed to obtain the value of the projection bin that is located along the same line.

different angles of rotation, the image can be rotated in the opposite direction and the process is repeated. This approximation assumes that only rays parallel to the collimator apertures can pass through them, so for a more accurate model other approaches are required.

A more realistic approach which is often used, especially in SPECT geometries with a limited number of collimator apertures (e.g. pinhole SPECT), is ray-tracing. Ray-tracing is based on the modeling of the aperture holes as a set of points through which we trace rays between the image and the detector surface. Most ray-tracing methods are either pixel- or ray-driven. Pixel-driven methods were the first to be proposed [61, 62]. In their most simple version, the center of each image pixel/voxel is mapped onto the detector by drawing a ray (a line) which connects them through the aperture points to the detector (see Fig. 2.13. (a)), so each pixel/voxel and aperture point is visited in a loop. The weight of the detector bins can be assigned by different interpolation methods. In the ray-driven approach, on the other hand, the mapping is done by drawing a ray from the center of each projection bin in the detector to the image space, passing through each aperture point (see Fig. 2.13. (b)), so it loops over each projection bin and aperture point. The contribution of an image element to a detector bin can be computed in different ways, a popular one being based on the length of the intersection of the corresponding ray with the image element L, shown in Fig. 2.13. (b) (Siddon's algorithm [63]). Finally, we also mention the distance-driven approach, first proposed by De Man

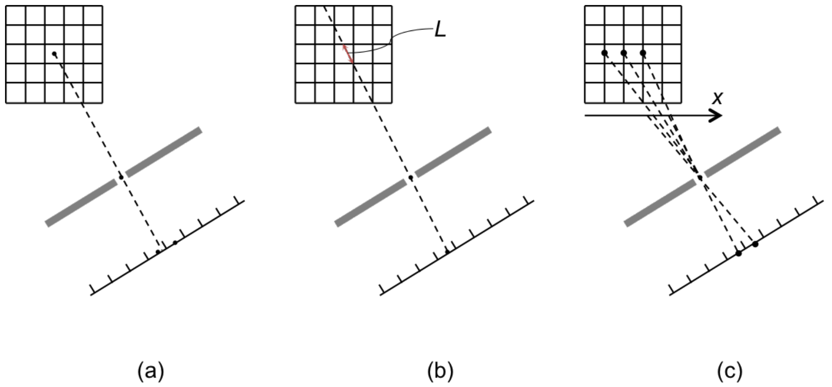

Figure 2.13: Schematic representation in 2D of ray-tracing methods, considering a pinhole aperture modeled as one point through its center: (a) pixel-driven; (b) ray-driven; (c) distance-driven.

and Basu for 2D CT [64] and later extended to 3D geometries [65, 66]. In this method, the boundaries of both image and projection elements are mapped onto a common line, shown as the x-axis in Fig. 2.13. (c). The weighting factors are the normalized lengths of overlap (for a detailed explanation see [65]). The distance-driven approach iterates over all the image and detector elements, but in a very computationally efficient way. It has been gaining popularity, especially in CT, due to its combination of speed and accuracy, and it has been recently shown to provide improved image quality in pinhole SPECT as compared to a ray-driven approach [67]. The distance-driven method is used in Chapter 4 to model a single-pinhole SPECT system.

The particular advantage of ray-tracing methods is that they are very fast to compute, so the projection and backprojection can be done on-the-fly, avoiding the need to store the (very large) system matrix $\mathbf{H}$ in computer memory. To improve their accuracy, all one has to do is increase the number of rays considered (for example, by dividing the aperture into more points, or dividing the image/projection elements into smaller pieces), but this of course makes them less computationally efficient. Several specific approaches have been proposed for different SPECT geometries [68, 69, 70, 71], but they are quite time-consuming, especially if there are many collimators apertures and/or there is a complex collimator geometry to take into account.

Finally, we should also mention a quite straightforward approach for analytical system modeling, which is to simply compute the sensitivity of each projection bin to each image element (or, in other words, computing the elements of $\mathbf{H}$ one by one), using sensitivity formulas similar to (2.1). A procedure to obtain an accurate estimation of this sensitivity value is developed in Section 3.3, and this is used to compute a system matrix for the analytical simulations in Chapters 5 to 7.

In all these methods, the intrinsic detector resolution is typically incorporated by blurring out the projection images with a 2D Gaussian kernel with the corresponding full width at half maximum (FWHM). Furthermore, because analytical methods are noiseless, to generate noisy (and therefore more realistic) projection data a Poisson random number generator can be used, using the analytical projection values as the mean of the distribution.

2.4.2 Monte Carlo Simulations

Monte Carlo methods are a broad class of numerical techniques that use random numbers to solve statistical problems in various fields. They are usually applied to simulate complex, non-deterministic situations which are difficult or impractical to reproduce with real experiments. Some interesting examples can be found in [72] (physics), [73] (biology) and [74] (geology).

In nuclear medical imaging [75], Monte Carlo methods are frequently used to simulate the radioactive decay of the tracer and the subsequent interactions of the emitted photons with matter (in the phantom, collimator and detector), which are stochastic phenomena. They have been used in SPECT since the 80's [76, 77, 78], and are currently the most common methods for simulating projection data from SPECT systems. We can also use them to produce high-count projection data from uniform gamma-ray sources located at each image voxel position, which can be used to compute the system matrix $\mathbf{H}$ that we employ in SPECT reconstructions [79, 80, 81].

In these methods, the value of a random variable is obtained by sampling a probability density function (PDF) using generated (pseudo)random numbers. These random numbers come from a uniform PDF. One way of doing this sampling is by using the Distribution Function method. In this method we compute the cumulative probability distribution $CPDF$ from its definition

$$CPDF(x) = \int_a^x PDF(x')dx',$$

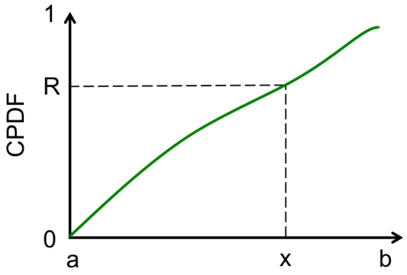

Figure 2.14: Plot of a cumulative probability distribution $CPDF$, where a random number $R \in [0,1]$ is used to choose the value of a random variable x, which is equivalent to the direct sampling of the PDF.

where $x \in [a,b]$, the range over which the PDF is defined (and the PDF should be normalized within this interval); we then generate a (pseudo)random number R from the range $[0,1]$ (where any number within the interval has the same probability of being picked); finally, we solve the equation

$$CPDF(x) = R$$

for x, which will give us the desired value. This last step can be visualized in Fig. 2.14 . Note that for Monte Carlo algorithms to be effective, it is crucial to use a good random number generator; using current computers this is not a truly random process, but by always starting with a different seed we may be able to assume it is random enough for our practical purposes. It is also important to know what the PDF of the underlying processes that we are trying to emulate looks like; as an example, the distance that a photon travels in a medium before interacting with it has a PDF given by

$$PDF(x) = \mu e^{-\mu x},$$

with μ the linear attenuation coefficient (which depends on the photon energy and the characteristics of the medium). For a more detailed overview of the use of Monte Carlo techniques in nuclear medicine, see for example chapter 25 in [41].

Monte Carlo simulations result in very realistic simulations of the imaging process in the scanner. The major drawback compared to a real experiment is that the system is modeled in a simplified way

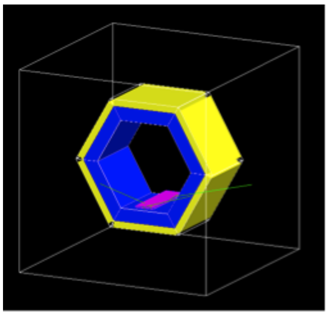

Figure 2.15: Modeling of a SPECT system in GATE. The detector material is shown in yellow, the collimator body in blue, and the phantom in purple. Also represented are two simulated photon trajectories (in green), which start in the phantom (where the activity is located).

(not taking manufacturing imperfections into account). Compared to analytical methods, on the other hand, the process can be extremely computation- and time-consuming, especially for low-sensitivity systems such as SPECT.

In this dissertation, and in a large portion of the current literature on SPECT, Monte Carlo simulations of the imaging process are performed using the simulation software GATE, the Geant4 Application for Tomographic Emission [82]. In Fig. 2.15 we show an example of a SPECT system configuration, a phantom and some photon trajectories, obtained using GATE. This open source software was and continues to be developed by many research groups, together forming the OpenGATE collaboration, and it builds upon Geant4 [83], a simulation toolkit collaboratively developed in C++ for comprehensive modeling of the physics of particle interactions. It is specifically developed to facilitate the use of certain Geant4 libraries for nuclear medicine applications, and it allows the design of standard geometries but also a significant amount of freedom in the system design. It also allows for the source and/or scanner components to move, and models the source decay's evolution in time. It tracks the photon's trajectory and simulates effects that occur as it goes through the phantom/collimator/detector materials, such as photoabsorption, Compton scatter and Rayleigh scatter. From running a program in GATE we get the time and position of all photon detections, and with this information we can produce the projection images that a real scanner would obtain. A GATE simulation also gives us more information about the processes occurring than a real experiment would, since the software controls everything that happens, which allows more in-depth studies. We can, for example, know exactly how many photons are lost due to attenuation/scatter in the phantom/collimator [82], whereas in a real experiment we only know how many photons are detected by the system. This can be used, for example, for accurate scatter correction [84].

In this dissertation, GATE is used in Chapter 3, Section 3.3, to simulate two new system designs, with non-standard collimator geometries. This means we can test their imaging performance in a realistic setting, without having to actually build them, which would be unpractical. The simulated data is used to validate the analytical method developed in Chapter 3, which is used for system modeling in the majority of the simulations in this dissertation.

2.4.3 Experimental System Matrix

The final type of modeling we describe here is that which is based on real experimental measurements of the system. The idea is that if we measure the detector response to a point source at all the voxel positions in image-space, one at a time, we obtain all the columns of the system matrix $\mathbf{H}$. The source can be moved very precisely using a 3D robot stage, and using this method everything in the instrumentation chain is considered, not as an ideal model but as it is in reality (with manufacturing imperfections, etc.). As such, using the experimental system matrix is generally the most accurate way of modeling a SPECT system, and when reconstructing real data obtained from the scanner it leads to increased image quality [85]. One limitation of the experimental method is that this process cannot be done on-the-fly, it is necessary to store the system matrix $\mathbf{H}$, but since only a limited number of detector pixels are sensitive to each voxel we can usually work with $\mathbf{H}$ more efficiently as a sparse matrix. We are also limited to testing existing scanners, so this approach cannot be used during the design process.

To minimize the effect of experimental noise in the system matrix measurement, the point source needs to be scanned for a long enough period of time at each position. Since there is a very large number of voxels to consider in 3D imaging this becomes quite cumbersome, especially as SPECT systems move towards better resolution images (which require smaller voxels). As such, in practice measurements are usually acquired only at a limited number of voxel positions, and a given model is used to obtain the remaining voxel projections.

This approach of obtaining the system matrix from point source acquisitions was mainly developed at the University of Arizona, and applied to the small-animal multi-pinhole SPECT scanners FASTSPECT [86], FASTSPECT II [14, 87] and M^{3}R [88]. In this thesis we use, in Section 7.5, the method developed by van der Have *et al.* [89, 85]. This approach first consists of acquiring point-source measurements at a limited number of voxel positions, and modeling the shape of the point-spread-functions; we then calculate the projection for the missing positions by taking the point-spread-function of the nearest voxel position that was measured and adjusting it based on the new point's location, as well as the expected resolution and sensitivity.

2.5 Image Quality

In this last section, we discuss techniques for evaluation of image quality (IQ) in SPECT imaging. We place particular emphasis on the calculation of the Contrast-to-Noise Ratio (CNR) using the analytical expressions proposed by Fessler *et al.* [57, 90] (Section 2.5.2), which is the method used in chapters 4 and 6.

2.5.1 Overview

Researchers strive for the best performing imaging systems. To measure the performance of an imaging scanner, one has to look at the quality of its images. The goal is most often to compare the image quality of either different systems or different settings of the same system. The first is useful to decide which system performs the best in the situation under study, and the second is used to optimize the design features or the scanning protocol to maximize the scanner's performance.

Sensitivity-resolution trade-off

In system optimization, it is common to use the predicted sensitivity and resolution of the system, computed either analytically or numerically, as indicators of image quality. For the optimization, a procedure similar to this is followed:

1. Define the required FOV and the system constraints;

2. Set a fixed target resolution, either at the center of the FOV or on average (the latter option is more indicative of the global performance);

3. Find the system parameters (or a relation between parameters), such as collimator aperture height, diameter, etc., that result in the given target resolution;

4. Limit the amount of collimator penetration allowed;

5. Find the parameters that comply with steps 3 and 4 which maximize the sensitivity of the system, either at the center of the FOV or the average over the FOV (the latter being the most comprehensive option).

This analysis is straightforward for standard parallel-hole, fanbeam and conebeam collimator geometries, for which closed form mathematical expressions can be used [91, 92, 93]. For optimizing a parallel-hole collimator configuration, for example, we can use the formulas described in Section 2.2.2: fixing the value of the total resolution R at a given height h, expressions (2.6) and (2.5) give us an equation with two unknowns d and a (aperture width and height, respectively); on the other hand, fixing the penetration β in formula (2.7) gives a relationship between a, d and t (septal thickness); with these two equations for three unknowns we can for example write d and t as functions of the aperture height a, and then write the sensitivity g in (2.4) as a function of a only; finally, we can take its derivative with respect to a and equate it to 0, giving us the value of a that maximizes the sensitivity g. This approach can also be used in more complicated geometries, if we can assume that locally they are close to a parallel-hole geometry [91].

For multi-pinhole collimators, on the other hand, the process is more complicated. This is due to the increased number of degrees of freedom on which the sensitivity and resolution depend, such as the number of pinholes, pinhole opening angle, pinhole tilt, etc. As such, most authors limit the number of degrees of freedom before performing the optimization, by restricting the possible system configurations. For example, Rentmeester *et al.* [94], Goorden *et al.* [25] and Nillius *et al.* [95] assume a spherical system (detector and collimator) with the pinholes all focused on the center of the FOV. A cylindrical geometry has also been evaluated in [18], with a predefined set of flat detectors.

The optimization of the sensitivity-resolution trade-off, although certainly indicative of a higher IQ, does not include some important elements that influence IQ, such as the angular sampling, and refers to sensitivity and resolution at the level of the system (and not the reconstructed image). However, it is a simple and straightforward method that can be easy to apply to standard SPECT system configurations, so it remains a very popular approach.

Objective Assessment

Another important approach is objective assessment of IQ, mainly introduced by Barrett [96, 97, 98, 99]. It stems from the fact that, ultimately, things like resolution and sensitivity are not in themselves the goal when performing medical imaging. The goal is to get the best outcome for the specific task(s) for which the system is intended, on average. For example, if the task for which we want to use the scanner for is to determine the presence of a certain disease, then the best system will be that which results in a higher rate of correct diagnoses.

So objective assessment of IQ is based on the idea that the quality is given by how well a certain observer performs a given task on an ensemble of subjects under investigation (patients). In other words, in order to say that a given scanning system is better for a given task, and will thus provide better results on average, one should take into consideration:

- the task;
- the observer;
- the ensemble of subjects.

In medicine, there are two main tasks to be considered (either separately or in combination) [100]: classification and estimation. A classification task is one which categorizes an image into one of a finite number of alternative classes. If there are only two classes (which is the most common scenario), we refer to a detection task. An example of a classification task can be the detection of a tumor in the body. Estimation tasks, on the other hand, quantify a certain parameter in the image, such as the size of a tumor or its localization.

Then it is necessary to define how the task will be performed, or, equivalently, what kind of observer is performing the task. In the case of lesion-detection tasks, a human (doctor) will usually be the final observer of the images, whereas in estimation tasks we often have a human-assisted computer observer. So the most realistic and accurate way to evaluate the performance of the tasks is with human-observer studies. This is, however, very time-consuming and impractical, since multiple observers need to evaluate the images, for all the systems under study. As an alternative to human-observer studies, several numerical observers have been developed to model human observers under certain conditions [101, 102]. The most common approach is to use linear numerical observers, which simply apply linear functions to the data, as they are computationally efficient and considerably successful in predicting observer performance (including human). Ideal linear observers are of particular importance, as they represent an upper limit for the performance of any linear observer; for detection and estimation tasks, the ideal linear observers are the Hotelling and the Wiener observer, respectively.

Once the observer is defined, we also need to choose a figure of merit to assess its performance. In lesion-detection studies, for example, the standard tool is the receiver-operator characteristic (ROC) curve [100]. This curve plots the fraction of true positives (detecting the presence of a lesion when it is actually present) versus the fraction of false positives (deciding that a lesion is present when this is not the case). The area under the curve (AUC) is then used to measure the performance of the observer in this task ($AUC = 1$ corresponds to never making a mistake, whereas an $AUC = 0.5$ would be equivalent to randomly guessing the outcome). It is also common to use the signal-to-noise ratio (SNR) as a figure of merit for detection tasks, since it has a one-to-one correspondence with the AUC [100].

The largest difficulty in using objective figures of merit stems from their higher complexity, which requires more computational capacity and time. For this reason, they are not that often used in practical studies, and are mainly restricted to evaluate performance in detection tasks (which are simpler than estimation tasks). As an intermediate between accuracy and efficiency, the techniques described in the next subsection have become increasingly popular for evaluating the system performance and optimization.

Local impulse response and covariance

Finally, we discuss a frequently used method to assess the resolution and noise in a reconstructed image (see Section 2.3 for some of the notation used in this section). These two properties give us an indication of how well the system performs, in combination with the reconstruction algorithm.

The resolution properties of a shift-invariant system can be represented using a shift-invariant convolution filter, the Impulse Response function. It has this name because it refers to the response of the system to an impulse function. Emission Tomography systems have a shift-variant response, so in this case we use a Local Impulse Response (LIR), l^j, which is defined (for voxel j of the image estimation $\hat{\mathbf{f}}$) as

$$l^j(\hat{\mathbf{f}}) = \lim_{\delta \to 0} \frac{E\left[\widehat{\mathbf{f} + \delta \mathbf{e}^j}\right] - E\left[\hat{\mathbf{f}}\right]}{\delta}, \tag{2.20}$$

with $E[\cdot]$ the expectation operator and $\mathbf{e}^j \in \mathbb{R}^{N \times 1}$ the jth unit vector. In other words, the LIR is the limiting difference between the mean reconstruction of the image with an additional impulse δ at voxel j and the mean of the original image reconstruction, normalized. To understand intuitively how this measures resolution, note that if there would be no blurring of the image from the imaging process, then an increase of δ in voxel j would result in $l^j = \mathbf{e}^j$. Several authors [47, 48, 103] have observed that in emission tomography, and using likelihood-based estimators, taking the expectation value of the estimator over a large number N_r of noise realizations of the data is roughly equivalent to reconstructing the noise-free data set

$$E\left[\hat{\mathbf{f}}\right] \approx \frac{1}{N_r} \sum_{i=1}^{N_r} \hat{\mathbf{f}}(\mathbf{g}_i) \approx \hat{\mathbf{f}}(\overline{\mathbf{g}}(\mathbf{f})), \tag{2.21}$$

where $\mathbf{g}_i$ is the ith independent noise realization of the projection data (all from the same mean value $\overline{\mathbf{g}}$). This corresponds to an assumption that the estimator is locally linear, and substituting (2.21) in (2.20) we get

$$l^j(\hat{\mathbf{f}}) \approx \lim_{\delta \to 0} \frac{\hat{\mathbf{f}}\left(\overline{\mathbf{g}}(\mathbf{f} + \delta \mathbf{e}^j)\right) - \hat{\mathbf{f}}\left(\overline{\mathbf{g}}(\mathbf{f})\right)}{\delta}. \tag{2.22}$$

This approximation means that to compute the LIR we only need to perform two reconstructions, instead of N_r, which is considerably faster. For the practical calculation of the LIR using this formula, the limit $\delta \to 0$ is replaced by a small δ value. The shape of the LIR vector is important for resolution investigation, but for many applications (such as optimization) it is more practical to work with a scalar quantity, which we call the contrast recovery coefficient (CRC), defined as

$$CRC_j := l_j^j(\hat{\mathbf{f}}). \tag{2.23}$$

The calculation of the noise properties of the estimator is mathematically more straightforward, but computationally heavier. To measure how the variation in each image voxel correlates with variation in the other voxels in the image, we use the covariance matrix, whose elements are mathematically defined as

$$Cov_{j'}^{j}(\hat{\mathbf{f}}) := E\left[\left(\hat{\mathbf{f}}^{j} - E\left[\hat{\mathbf{f}}^{j}\right]\right)\left(\hat{\mathbf{f}}^{j'} - E\left[\hat{\mathbf{f}}^{j'}\right]\right)\right], \quad j, j' \in \{1, \dots, N\} \tag{2.24}$$

where the mean value $E\left[\cdot\right]$ is taken over an N_r number of noise realizations (i.e. independent experiments) considered, which should be large. In this case we really have to perform an N_r number of reconstructions (as well as acquire/simulate N_r projection realizations), and the larger N_r the more accurate the approximation. The corresponding scalar figure of merit is the variance, which measures the spread around the mean of the voxel value, as is defined for voxel j as

$$Var_j := Cov_j^j(\hat{\mathbf{f}}). \tag{2.25}$$

Using only resolution or variance to evaluate image quality can be misleading, since they are inversely related. In other words, a change in the system geometry (for example) that leads to an improvement in resolution will usually also lead to an increase in the variance (noise), so the final image quality is not necessarily better (the so-called noise-resolution trade-off). As such, to evaluate the combined effect of the resolution and variance, we define a single figure of merit called the contrast-to-noise ratio (CNR)

$$CNR_j := \frac{CRC_j}{\sqrt{Var_j}}. \tag{2.26}$$

The concepts described in this subsection are the basis for the analytical formulas in Section 2.5.2, which will later be used in chapters 4 and 6.

2.5.2 FIM-based Approximation for Evaluation of Image Quality in PF-PML

In this section we consider the more specific problem of estimating the image voxel values using PF-PML reconstruction (see Section 2.3), and a deterministic and more efficient approach for the evaluation of the IQ. The task at hand is to evaluate the IQ of the reconstructed images through the LIR / CRC, which measure resolution, and the covariance matrix / variance, which measure noise, as defined in Section 2.5.1.

There is no exact formula for the LIR or the covariance matrix of the PML estimate. As described in Section 2.5.1, we can estimate them by performing reconstructions from a large number of independent Poisson noise realizations of the projection data, ran until convergence, in order to simulate the experiment an “infinite” number of times [57, 90]. This is, however, usually not practical. As an alternative, Fessler *et al.* [57, 90] have derived analytical approximations of the LIR, for a voxel with index $j \in \{1, \dots, N\}$, and of the covariance matrix. These approximations assume that the estimator (2.13) is locally linear, i.e. formula (2.21) is valid, and for Poisson data they result in

$$l^j(\hat{\mathbf{f}}_{PML}) \approx [\mathbf{F} + \beta\mathbf{R}]^{-1}\mathbf{F}\mathbf{e}^j, \tag{2.27}$$

$$Cov(\hat{\mathbf{f}}_{PML}) \approx [\mathbf{F} + \beta\mathbf{R}]^{-1}\mathbf{F}\left([\mathbf{F} + \beta\mathbf{R}]^{-1}\right)^{\dagger}, \tag{2.28}$$

where $\mathbf{F}$ is the Fisher information matrix (FIM), $\mathbf{R}$ is the Hessian matrix of $R(\mathbf{f})$, $\mathbf{e}^j \in \mathbb{R}^{N\times 1}$ is the jth unit vector and † the conjugate transpose operator. The derivation of (2.27) and (2.28) is quite lengthy, so we direct the interested reader to the original papers [57, 90].

The elements (j, j') of the FIM are by definition given by

$$\mathbf{F}_{jj'} := -E\left[\frac{\partial^2}{\partial x_j \partial x_{j'}} L(\mathbf{g}|\mathbf{f})\right], \quad j, j' \in \{1, \dots, N\}, \tag{2.29}$$

with $E[\cdot]$ the expectation operator. Using (2.10) and (2.8) in this expression we eventually get a simplified formula for the FIM,

$$\mathbf{F} = \mathbf{H}^T \mathrm{diag}\left(\frac{1}{\bar{y}_i}\right)\mathbf{H}, \tag{2.30}$$

where ^{T} represents the transpose operator and $\mathrm{diag}(e_i)$ a diagonal matrix whose (i, i) entry is equal to e_i, $i \in \{1, \dots, M\}$.

To obtain the formula equivalent to (2.27)-(2.28) for PF-PML, we simply replace (2.13) by (2.19) in Fessler's derivations [57, 90], and since $\mathbf{P}$ is a constant and real linear operator (2.27)-(2.28) become

$$
\begin{aligned}
l^j(\hat{\mathbf{f}}_{PF-PML}) &\approx \mathbf{P}[\mathbf{F}+\beta\mathbf{R}]^{-1}\mathbf{F}\mathbf{e}^j, && (2.31)\\
Cov(\hat{\mathbf{f}}_{PF-PML}) &\approx \mathbf{P}[\mathbf{F}+\beta\mathbf{R}]^{-1}\mathbf{F} && \\
&\qquad \left([\mathbf{F}+\beta\mathbf{R}]^{-1}\right)^{\dagger}\mathbf{P}^{T}. && (2.32)
\end{aligned}
$$

To obtain an approximation of the CRC and the variance at voxel j, after PF-PML reconstruction, we simply take the jth element of vector (2.31) and the (j, j) element of matrix (2.32), respectively.

Expressions (2.31) and (2.32) can be used to evaluate the resolution and noise properties in the final reconstructed image, and in the rest of this dissertation we shall refer to them as the FIM-based approximations of the LIR vector and of the covariance matrix, respectively. Note that if we consider the maximum likelihood limit ($\beta \to 0$) this poses an issue in expressions (2.31)-(2.32) because in pinhole SPECT the FIM is generally not invertible. In this case, an expression for the pseudoinverse of the FIM has been proposed [104], but we avoid this additional approximation by taking $\beta \neq 0$.

Note that the inversion of $[\mathbf{F}+\beta\mathbf{R}]$, an $N\times N$ matrix, is computationally a very intensive operation. In Chapter 4 we will take these formulas and derive approximations that make the calculations more tractable in practice. These approaches will then be used both in chapters 4 and 6 to evaluate the IQ of different SPECT systems.

2.6 Summary

In this introductory chapter we explained what SPECT is, and we described some important concepts in SPECT imaging which are of special importance in this dissertation.

In Section 2.2, we explored one of the important components of a gamma camera, the collimator. In particular, we characterized two types of collimator: pinhole collimators are used directly in chapters 3 and 4, and are also very important in stationary and small-animal SPECT imaging (which is the focus of later chapters); parallel-hole collimators are used in Chapter 3 as well, and are the basis of the novel collimator designs developed in chapters 5 to 7.

In Section 2.3 we explained the process of image reconstruction, and in particular MLEM and PML iterative reconstruction. These approaches are used in simulations throughout the dissertation.

In Section 2.4, some of the most important types of system modeling were described. Analytical methods are used in all the chapters in the dissertation. Monte Carlo simulations are used in Chapter 3 to validate analytical methods. Finally, in Chapter 7 we also briefly refer to the experimental system matrix method, used to obtain some preliminary reconstructions from a real system.

Finally, in Section 2.5 we discussed evaluation of IQ. We made an overview of the different methods used in the state-of-the-art, and then addressed the FIM-based approximation of the LIR and covariance for PF-PML. This last approach is the basis of the methods for efficient evaluation of IQ described in Chapter 4.

Chapter 3

Modeling of Geometric Response of Complex Collimator Geometries in SPECT

In this chapter we describe analytical principles for modeling the geometric response of any collimator geometry, and how we applied them to the study of different SPECT systems. The methods described are implicitly used in the work presented in the remaining chapters of the dissertation. The general concept is explained in section 3.1. Then, in sections 3.2 and 3.3 we apply the method to non-standard pinhole and parallel-hole collimator geometries, respectively. We describe both the theoretical approach and its validation with simulation studies.

3.1 Introduction

Having an accurate model for the response of a SPECT scanner is crucial in performance evaluation and reconstruction [59, 60]. In this chapter we are interested in modeling the response of systems with collimator geometries that differ from standard SPECT systems, in particular some variations on conventional pinhole and parallel-hole SPECT systems. These are cases in which the usual formulas for the sensitivity of a pinhole collimator [11] and of a parallel-hole collimator [26] are poor approximations of reality, and a more accurate model is required.

The most accurate way of computationally modeling the system geometry would be through high-count Monte Carlo simulations [79, 80, 81], but for low-sensitivity systems (which is the case) this is extremely demanding in terms of time, computation complexity and storage. Simplified calculations based on ray-tracing have also been proposed for many SPECT geometries [68, 69, 70, 71], but it tends to be quite time-consuming (to get accurate results) and it can be difficult to include complex collimator geometries.

In Chapter 2.2 we introduced the notion of geometric sensitivity (g). We showed that the sensitivity of a flat surface area (A) to a point source emitting isotropically (Src) is given by the corresponding solid angle, normalized, which is approximately given by (see equation (2.2)):

$$g \approx \frac{A \sin^3 \theta^c}{4\pi h^2}, \tag{3.1}$$

where h is the perpendicular distance from the source to the surface plane and θ^c is the angle between the plane of A and the ray connecting its center to the source. However, this formula assumes that all the emitted photons in the solid angle Ω subtended by the surface area (A) reach the detector, which is not always true. In this chapter, based on the work of [105, 106], we adapt the use of the sensitivity formula (3.1) to particular situations in which the imaging system's properties, in particular the collimator geometry, require a more accurate determination of the sensitivity.

3.2 Application 1: Pinholes and Loftholes

3.2.1 Analytical Method

The sensitivity of a single pinhole collimator is usually assumed to be given by (3.1), where A is simply the area of the circular pinhole aperture $\pi\left(\frac{d}{2}\right)^2$ [11]. However, this does not take the effect of the entrance/exit openings into account (see Fig. 3.1). When the collimator has an entrance and/or exit opening, only the photons crossing the aperture in a limited region are able to go through. This region is the intersection A_{int} between the pinhole aperture and the entrance and exit openings projected onto the aperture plane. This is illustrated in Fig. 3.2, where we can see three possible collimator geometries and the corresponding A_{int} region: they all have a circular aperture, the first has a circular exit,

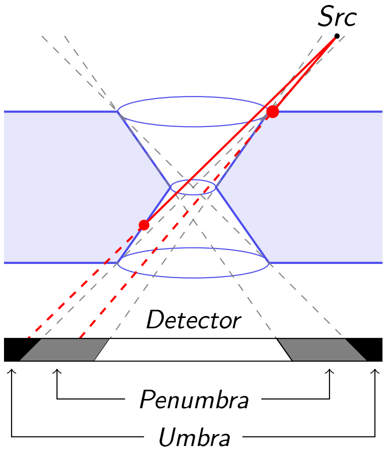
Src
Detector
Penumbra
Umbra

Figure 3.1: Schematic representation of a standard pinhole aperture and detector, showing the detector penumbra (region that does not receive photons from the entire aperture area) and umbra (region that does not receive any photons) regions.

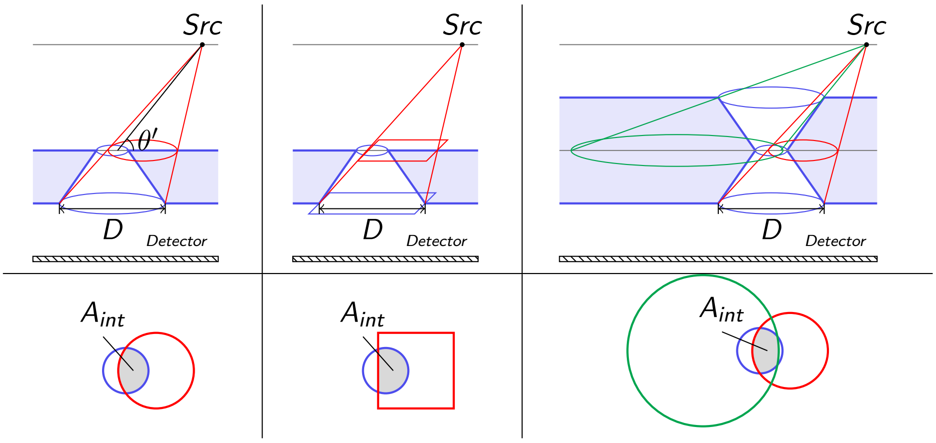
Src
θ'
D
Detector
Src
D
Detector
Src
D
Detector
A_{int}
A_{int}
A_{int}

Figure 3.2: Three possible collimator geometries and the corresponding A_{int} region. On top you see the collimator geometry, and on the bottom the projection of the entrance/exit openings on the aperture plane (A_{int}).

the second a square exit, and the last geometry a circular entrance and exit. The square geometry is what is called a lofthole, which is a generalization of the pinhole geometry that allows for non-circular entrance and exit openings [107, 37].

To correct for this effect, we can start from equation (2.1) but integrate over A_{int}, and then do a similar approximation to what was done in (2.2)

$$g_{corr} = \frac{1}{4\pi h^2} \iint_{A_{int}} \sin^3 [\theta(x, y)]\, dxdy \approx \frac{A_{int} \sin^3 \theta'}{4\pi h^2}, \tag{3.2}$$

with θ' the angle measured from the center of A_{int} (see Fig. 3.2). The analytical calculation is different for each particular pinhole/lofthole geometry, but we can generally divide A_{int} in 3 parts: when gamma-photons originating from the point source can go through the aperture and hit the detector without interference from the entrance or exit opening (High Sensitivity Region), $A_{int} = A_{aperture} = \pi \left(\frac{d}{2}\right)^2$; when no gamma-photons originating from Src are able to hit the detector (No Sensitivity Region), $A_{int} = 0$; and finally there is the intermediate case (Low Sensitivity Region), when some photons are stopped by the entrance and/or exit opening. See Fig. 3.3 for a visual representation of the high, low and no sensitivity regions of image-space. So in order to get an analytical model for the point sensitivity, we need to: 1) determine the boundaries for the Src coordinates on these 3 regions; 2) find the analytical formula for A_{int} in the Low Sensitivity Region. From this point on, when we refer to A_{int} in this section we are considering the Low Sensitivity Region.

The effect of the shape of the entrance and exit openings becomes crucial when the collimator is very close to the detector and/or the source Src. This problem has been discussed in literature for cylindrical holes in Chapter 4 of [105] and knife-edge pinholes in [106]. In this section we extend the approach to a hole with a circular exit and a hole with a square exit only, with the diameter of the aperture circle smaller or equal to the exit opening's projected diameter or side ($d \leq D'$), such as shown in the first two images of Fig. 3.2, but the general case can be built from here for any geometry.

3.2.1.1 Circular exit (pinhole)

We start by aligning the x-axis of the reference frame in the aperture plane with the direction defined by the perpendicular projection of the point source in this plane, so that the aperture circle and the projec-

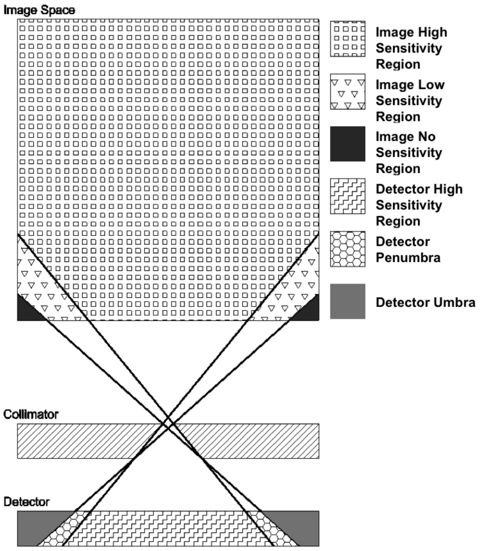
Image Space
Image High Sensitivity Region
Image Low Sensitivity Region
Image No Sensitivity Region
Detector High Sensitivity Region
Detector Penumbra
Detector Umbra
Collimator
Detector

Figure 3.3: Schematic representation of a detector and a collimator with a single aperture, showing the high-sensitive, low-sensitive and insensitive areas of the image-space and detector.

tion of the exit opening have their center points on this axis (see Fig. 3.4 and Fig. 3.5). Due to the pinhole's symmetry, the (non-negative) x-coordinate of Src, x_{Src}, suffices to determine the corresponding sensitivity (for a given h).

Let us start by computing x_1 and x_2, the x-coordinates of the intersection points I_1 and I_2 between the projection of the exit opening and the x-axis, or, using the points in Fig. 3.4, the intersections between the line segments $\overline{SrcA}$ and $\overline{SrcB}$, respectively, with $z = 0$. Starting with x_1, as the line segments $\overline{SrcI_1}$ and $\overline{SrcA}$ have the same direction, they define the same slope, and so we can write

$$\begin{aligned} \text{slope } \overline{SrcI_1} &= \text{slope } \overline{SrcA}, \\ \frac{h}{x_{Src} - x_1} &= \frac{h+t}{x_{Src} + \frac{D}{2}}, \\ x_1 &= x_{Src} - \frac{h}{h+t}\left(x_{Src} + \frac{D}{2}\right). \end{aligned} \tag{3.3}$$

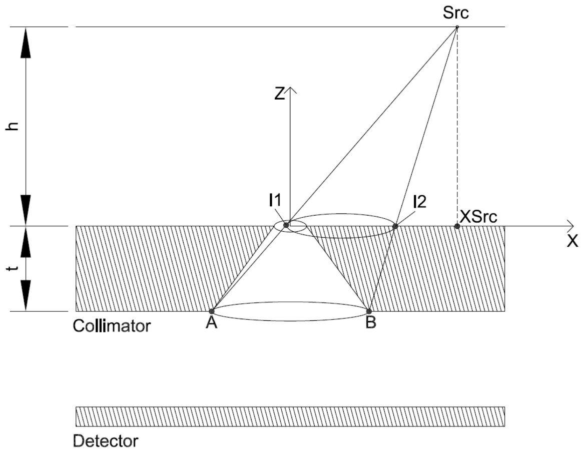
Src
Z
h
I1
I2
XSrc
X
t
Collimator
A
B
Detector

Figure 3.4: Representation of the pinhole in the reference frame and some points of interest.

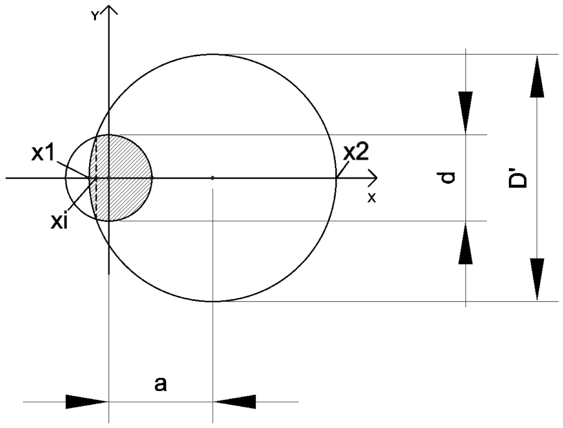
Y
x1
x2
x
xi
d
D'
a

Figure 3.5: Intersection of the pinhole aperture circle with the exit circle projection from the point source onto the aperture plane.

Following the same reasoning we get

$$x_2 = x_{Src} - \frac{h}{h+t}\left(x_{Src} - \frac{D}{2}\right), \tag{3.4}$$

and it follows that the diameter D' of the circle of the projection of the exit opening onto the aperture plane is

$$D' = x_2 - x_1 = D \times \frac{h}{h+t}. \tag{3.5}$$

Looking at Fig. 3.5, the point sources in the High Sensitivity Region are such that $x_1 \leq -\frac{d}{2}$, and using (3.3) we get

$$x_{Src} - \frac{h}{h+t}\left(x_{Src} + \frac{D}{2}\right) \leq -\frac{d}{2}, \tag{3.6}$$

$$x_{Src} \leq \frac{h}{t}\left(\frac{D}{2} - \frac{d}{2}\right) - \frac{d}{2} = \{x_{Src}\}_{min}, \tag{3.7}$$

or, in other words,

$$Src \in High\,Sensitivity\ Region \Leftrightarrow x_{Src} \in [0, \{x_{Src}\}_{min}]. \tag{3.8}$$

The No Sensitivity Region starts when $x_1 = \frac{d}{2}$, and doing the same calculations we get the upper boundary of the Low Sensitivity Region region

$$\{x_{Src}\}_{max} = \frac{h}{t}\left(\frac{D}{2} + \frac{d}{2}\right) + \frac{d}{2}. \tag{3.9}$$

The equations of the two intersecting circles are:

$$x^2 + y^2 = \left(\frac{d}{2}\right)^2, \tag{3.10}$$

$$(x-a)^2 + y^2 = \left(\frac{D'}{2}\right)^2, \tag{3.11}$$

where a (see Fig. 3.5) is the distance between the centers of the circles, and can be written as

$$a = \frac{D'}{2} + x_1 = \frac{t}{h+t}x_{Src}. \tag{3.12}$$

Using formulas (3.10) and (3.11), the x-coordinate of the intersection of the two spheres, x_i, is given by

$$(x_i - a)^2 - x_i^2 = \left(\frac{D'}{2}\right)^2 - \left(\frac{d}{2}\right)^2,$$

$$x_i = \frac{a^2 - \left(\frac{D'}{2}\right)^2 + \left(\frac{d}{2}\right)^2}{2a}. \tag{3.13}$$

The upper area of the intersection region ($y \geq 0$) is computed (see Fig. 3.5) by integrating over the upper half of the projection of the exit opening between x_1 and x_i and over the upper half of the aperture circle between x_i and $\frac{d}{2}$. The lower area is the same, so we finally get

$$\begin{aligned} A_{int} &= 2\int_{x_1}^{x_i} \sqrt{\left(\tfrac{D'}{2}\right)^2 - (x-a)^2}dx + 2\int_{x_i}^{\frac{d}{2}} \sqrt{\left(\tfrac{d}{2}\right)^2 - x^2}dx \\ &= \left(\frac{D'}{2}\right)^2 \cos^{-1}\left(\frac{a-x_i}{\frac{D'}{2}}\right) + \left(\tfrac{d}{2}\right)^2 \cos^{-1}\left(\frac{x_i}{\frac{d}{2}}\right) \\ &\quad -a\sqrt{\left(\tfrac{d}{2}\right)^2 - (x_i)^2}. \end{aligned} \tag{3.14}$$

3.2.1.2 Square exit (lofthole)

We consider the exit opening to be a square of side D and the reference frame in the aperture plane is centered on the aperture, with its axes parallel to the sides of the exit opening (see Fig. 3.6). For symmetry reasons we choose to consider only positive values for the point source coordinates (x_{Src}, y_{Src}) (otherwise we apply the transformation $(x_{Src}, y_{Src}) \to (|x_{Src}|, |y_{Src}|)$).

The intersections of the projection exit with $y = 0$ and $x = 0$ are computed just as before for the pinhole, and we get the same formulas as before:

$$x_1 = x_{Src} - \frac{h}{h+t}\left(x_{Src} + \frac{D}{2}\right), \quad x_2 = x_{Src} - \frac{h}{h+t}\left(x_{Src} - \frac{D}{2}\right), \tag{3.15}$$

$$y_1 = y_{Src} - \frac{h}{h+t}\left(y_{Src} + \frac{D}{2}\right), \quad y_2 = y_{Src} - \frac{h}{h+t}\left(y_{Src} - \frac{D}{2}\right) \tag{3.16}$$

and again the side of the projected square will be

$$D' = x_2 - x_1 = y_2 - y_1 = D \times \frac{h}{h+t}. \tag{3.17}$$

Due to the fact that $x_{Src}, y_{Src} \geq 0$, this implies that $x_2 \geq |x_1|$ and $y_2 \geq |y_1|$. We also have that $x_2, y_2 \geq \frac{d}{2}$, as we consider $D' \geq d$. This will help to reduce the number of cases to consider in the following computations.

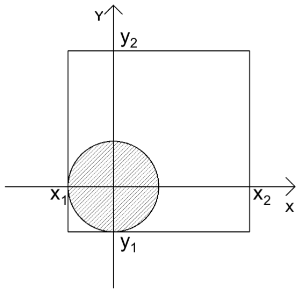

Figure 3.6: Extreme case of the exit opening projection from a point source in the High Sensitivity Region onto the aperture plane.

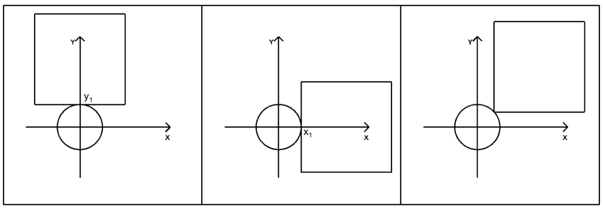

Figure 3.7: Extreme cases of the exit opening projections from point sources in the No Sensitivity Region onto the aperture plane.

For a given point source, we first test if it is located in the High Sensitivity Region, meaning (Fig. 3.6) that

$$x_1 \leq -\frac{d}{2} \quad \wedge \quad y_1 \leq -\frac{d}{2}, \tag{3.18}$$

or if it is in the No Sensitivity Region (Fig. 3.7)

$$x_1 \geq \frac{d}{2} \quad \vee \quad y_1 \geq \frac{d}{2} \quad \vee \quad \left(\sqrt{x_1^2 + y_1^2} \geq \frac{d}{2} \wedge x_1, y_1 \geq 0\right). \tag{3.19}$$

All points outside of these conditions are in the Low Sensitivity Region.

The shape of A_{int} varies according to the position of the source, so we start from the case with the maximum number of intersections between the circle and square (Fig. 3.8). The upper part of A_{int} ($y > 0$), A_u, can be simply written as the integral over the upper half of the aperture

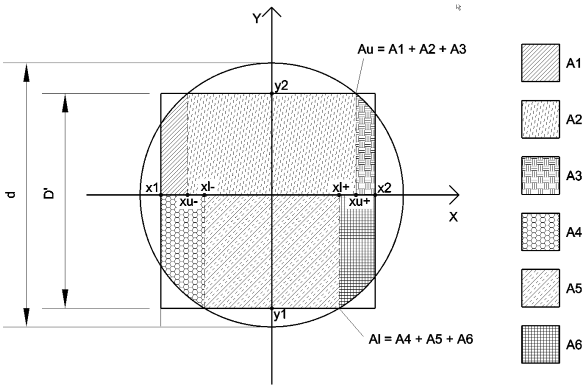

Figure 3.8: The different possible intersection shapes of the aperture with the exit opening projection.

circle between x_1 and $\frac{d}{2}$, so

$$A_u = I(x_1, \frac{d}{2}), \tag{3.20}$$

with

$$\begin{aligned} I(x_a, x_b) &= \int_{x_a}^{x_b} \sqrt{\left(\frac{d}{2}\right)^2 - x^2 dx} \\ &= \left(\frac{d^2}{8} \sin^{-1}\left(\frac{x}{\frac{d}{2}}\right) + \frac{x}{2}\sqrt{\left(\frac{d}{2}\right)^2 - x^2} \right) \Bigg|_{x_a}^{x_b}. \end{aligned} \tag{3.21}$$

The lower part of the area ($y < 0$), A_l, is divided in three parts (see Fig. 3.8),

$$A_l = A_4 + A_5 + A_6, \tag{3.22}$$

which separated by the intersections of the circle with the $y = y_1$ line, with coordinates

$$x_+ := x_{l+} = \sqrt{\left(\frac{d}{2}\right)^2 - y_1^2}, \quad x_- := x_{l-} = -x_{l+}, \quad \text{for } |y_1| \leq \frac{d}{2} \tag{3.23}$$

The first part, A_1, is calculated by integrating over the aperture circle between x_1 and x_-, so

$$A_1 = I\left(x_1, x_-\right). \tag{3.24}$$

The second part is bounded by the $y = y_1$ line, between x_- and x_+

$$A_2 = |y_1|\left(x_+ - x_-\right), \tag{3.25}$$

and the third part is similar to A_1,

$$A_3 = I\left(x_+, \frac{d}{2}\right). \tag{3.26}$$

To generalize the intersection area calculation, we consider the other possible intersection shapes. If $x_1 \leq -\frac{d}{2}$, the lower integration limit in (3.20) and (3.24) is $-\frac{d}{2}$ instead of x_1, so in these equations we replace x_1 by $\max\left(-\frac{d}{2}, x_1\right)$; when $x_1 \geq x_-$, which excludes the previous case since $x_- \geq -\frac{d}{2}$, then $A_1 = 0$, and so we can in this case define the upper integration limit as equal to the lower limit x_1. Combining this, we can re-write A_u and A_1 as

$$A_u = I\left(\max\left(-\frac{d}{2}, x_1\right), \frac{d}{2}\right), \tag{3.27}$$

$$A_1 = I\left(\max\left(-\frac{d}{2}, x_1\right), \max\left(x_-, x_1\right)\right). \tag{3.28}$$

For $x_+ \geq x_1 \geq x_-$, the rectangle A_2 is between $x = x_+$ and $x = x_1$, instead of $x = x_-$, and for $x_1 \geq x_+$ it becomes zero, so to incorporate this we re-write (3.25) as

$$A_2 = |y_1|\left(\max\left(x_+, x_1\right) - \max\left(x_-, x_1\right)\right). \tag{3.29}$$

Following the same reasoning for (3.26) we get

$$A_3 = I\left(\max\left(x_+, x_1\right), \frac{d}{2}\right). \tag{3.30}$$

When x_- and x_+ are not defined, meaning that $y_1 < -\frac{d}{2}$, A_2 disappears, and upper limit of the integration in A_1 should coincide with the lower integration limit of A_3, so we define

$$x_+ = \begin{cases} \sqrt{\left(\frac{d}{2}\right)^2 - y_1^2}, & \text{if } |y_1| < \frac{d}{2} \\ 0, & \text{if } |y_1| \geq \frac{d}{2} \end{cases}, \quad x_- = -x_+, \tag{3.31}$$

and the total generalization of the lower area is given by

$$\begin{aligned} A_l = I\left(\max\left(-\frac{d}{2}, x_1\right), \max\left(x_-, x_1\right)\right) \\ +|y_1|\left(\max\left(x_+, x_1\right) - \max\left(x_-, x_1\right)\right) + I\left(\max\left(x_+, x_1\right), \frac{d}{2}\right). \end{aligned} \tag{3.32}$$

When $y_1 \leq 0$, A_{int} is given by summing A_u with A_l, but when $y_1 > 0$ this is no longer valid (the intersection is contained in the $y > 0$ plane). In the second case, we have to subtract A_l from A_u, and so we get to the general expression for the intersection area

$$A_{int} = A_u - \operatorname{sgn}(y_1) A_l, \tag{3.33}$$

where A_u and A_l are given by formulas (3.27) and (3.32) respectively, and

$$\operatorname{sgn}(x) = \begin{cases} 1 & \text{if } x > 0 \\ 0 & \text{if } x = 0 \\ -1 & \text{if } x < 0 \end{cases}.$$

3.2.2 Simulations

As a practical application, we use our corrected analytical sensitivity to compare sensitivity curves for different system settings which are considered equivalent in light of the usual formula (2.2). We consider the pinhole and the lofthole geometries shown in Fig. 3.9. The perpendicular distance between the source and the collimator is $h = 5\,\mathrm{mm}$, the two collimator diameters are $d = 1\,\mathrm{mm}$ and $D = 19.4\,\mathrm{mm}$ (in both geometries), and the source position x_{Src} varies from 0 to $12\,\mathrm{mm}$. The first comparison study we make is between the sensitivity obtained for the pinhole collimator if its thickness t is $t_1 = 10\,\mathrm{mm}$ versus $t_2 = 5\,\mathrm{mm}$. Then, fixing $t = 10\,\mathrm{mm}$, we compare the pinhole with the lofthole geometry.

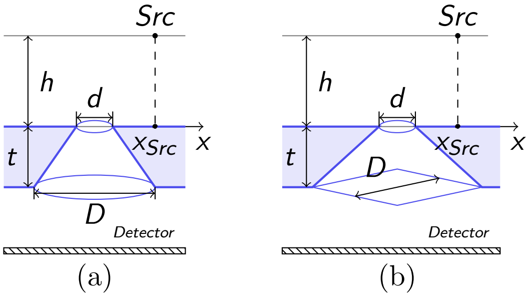

Figure 3.9: Collimator geometries and variables used: (a) pinhole, (b) lofthole.

To compute the analytical sensitivity g_{corr} we use expression (3.2), and replace A_{int} by $\pi\left(\frac{d}{2}\right)^2$ if x_{Src} is in the High Sensitivity Region, by 0 if it belongs to the No Sensitivity Region, and if x_{Src} is in the Low Sensitivity Region A_{int} is given by (3.14) and (3.33) for the pinhole and lofthole geometries respectively. The boundaries of the regions are also as derived in sections 3.2.1.1 and 3.2.1.2.

We validate the expressions for the analytical sensitivity with a ray tracer. The way it works is by randomly selecting a direction for a photon leaving the source, then tracing its geometric path, and calculating if, at any point, this path intersects the collimator. If a photon is able to reach the detector without intersecting the collimator, then we count it as a detection. By doing this many times we get an increasingly accurate value for the geometric sensitivity (the fraction of photons that reaches the detector), which we will refer to as $g_{simulated}$. The ray tracer was stopped after either $10,000$ detections occurred or $100,000,000$ photons were emitted from the source.

3.2.3 Results and Discussion

In this section, the goal is to derive and validate an analytical expression for the total pinhole sensitivity to activity emitted from a point source, taking the penumbra into account. We also want to use the analytical calculations to study the effect of having non-circular (in this case square) exit/entrance openings – the so-called lofthole collimator [107, 37].

In the figures shown here we represent the standard sensitivity prediction g (given by the formulation (2.2)), the analytical prediction derived

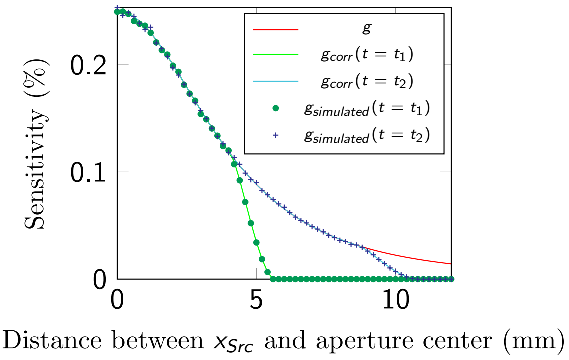

Figure 3.10: Plot of g, g_{corr} and $g_{simulated}$ for the pinhole geometry, comparing the collimator thicknesses t_1 and t_2 ($t_1 > t_2$).

in sections 3.2.1.1 and 3.2.1.2 (g_{corr}) and the prediction computed using the ray-tracer ($g_{simulated}$). In Fig. 3.10 we plot the sensitivity of the pinhole geometry for thicknesses t_1 and t_2, and in Fig. 3.11 we compare the sensitivity given by the pinhole and lofthole geometries (when the source is moved along the diagonal of the square, as shown in Fig. 3.9).

We first note that in all cases the corrected analytical predictions match the standard sensitivity formula when the projected point source (x_{Src}, y_{Src}) is close to the center of the pinhole, which corresponds to the High Sensitivity Region, then they become lower (Low Sensitivity Region) and eventually reach 0 in the No Sensitivity Region,

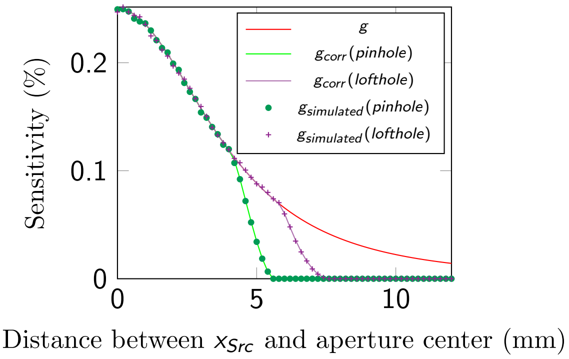

Figure 3.11: Plot of g, g_{corr} and $g_{simulated}$ for the pinhole and lofthole geometries ($t = t_1$).

whereas formula (2.2) assumes the sensitivity is always positive and independent of t and the shape of the entrance/exit. The corrected analytical predictions match the simulated values very closely, and indeed we obtain an error of less than 3% in the Low Sensitivity Area ($Error = |g_{simulated} - g_{corr}|/g_{simulated}$), which confirm our expectations that the corrected formulas are much more accurate at evaluating the geometric sensitivity in the cases explored in this section than equation (2.2). For practical implementations, in which penetration should also be taken into account, an effective diameter should be used in the formulations instead of the real diameter.

The influence of increasing the collimator thickness t is that the penumbra and umbra regions on the detector increase. Therefore, the x-coordinate for which the sensitivity starts being affected by the collimator entrance and exit walls is lower, which is exactly what we see in Fig. 3.10. In addition, this effect becomes more important when the object comes very close to the collimator (we have $h = t_2 = t_1/2$), which is the case in the compact small-animal SPECT systems that our group is developing using lofthole collimators [18].

The influence of changing from a circular to a square geometry is that the penumbra and umbra regions in the detector decrease (if the side of the square is equal to the circle diameter, D), and therefore the point sensitivity is higher for certain regions in image space, as can be seen in Fig. 3.11. In a flat collimator (as shown in the examples here) we can fit the same number of pinholes as loftholes, so the loftholes will allow us to use the entire detector more efficiently. However this behavior is not apparent if we just use expression (2.2). For a more detailed comparison of these two systems (including experimental results), see [37].

In conclusion, we see that our calculation provides a much better fit for the pinhole/lofthole geometric sensitivity for cases in which the penumbra effect is significant. This effect can have a substantial influence on the total sensitivity, e.g. when $h \approx t$. The formula enables system designers to place pinholes more efficiently, especially in multi-pinhole collimators, where projections may overlap. It also allows them to compare different shapes of the exit/entrance openings (lofthole). Finally, it is crucial for a more accurate sensitivity modeling in image reconstruction.

As a concluding remark, we note that the analytical calculation is different for each lofthole geometry, and can be quite lengthy for some geometries with less symmetry (e.g. pentagonal loftholes, tilted pinholes...). As an alternative one can do an accurate (but also slower) evaluation of the geometric sensitivity by discretizing A_{int} in a sufficient number of smaller areas ΔA and then use it in the formula

$$g_{corr} \approx \frac{1}{4\pi h^2} \sum_{(i,j)\in A_{int}} \sin^3\left[\theta(i,j)\right] \Delta A. \tag{3.34}$$

3.3 Application 2: Parallel-holes of Non-standard Shape

3.3.1 Analytical Method

The point sensitivity of a parallel-hole collimator is usually assumed to be given by (2.4). However, it is not valid in situations in which:

- the height and shape of individual holes differ;
- the holes are not oriented perpendicularly to the detector;
- the size of the septa is not negligible compared to the hole size;
- the source comes very close to the collimator and detector.

There are many situations in which it makes sense to have a system that violates one or more of these assumptions, so a more general analytical approach is desirable for their modeling. In this section we propose a method to compute the geometric sensitivity of a detector pixel to a point source, taking all these factors into account.

First of all note that, in the absence of a collimator, the geometric sensitivity of a detector pixel to a point source emitting isotropically is given by (3.1):

$$g_{pixel} \approx \frac{A_{pixel} \sin^3\theta}{4\pi h^2}, \tag{3.35}$$

where A_{pixel} is the detector pixel area, θ the angle between the pixel and the ray connecting it to the source, and h the perpendicular distance from the source to the detector. When certain photons that would otherwise hit the detector are blocked by a collimator, we have to adjust

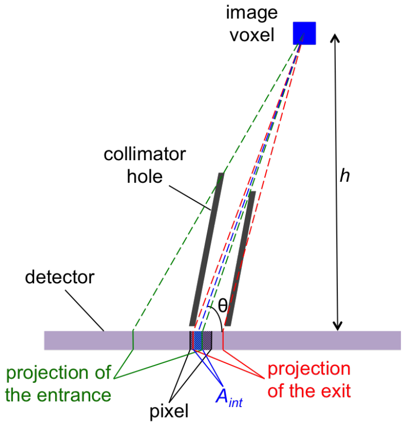

Figure 3.12: 2D illustration of the principle behind the sensitivity calculation for a single parallel hole.

the area A_{pixel} so that it corresponds to the area of the pixel that can be hit, which we call A_{int}

$$g_{pixel-coll} \approx \frac{A_{int} \sin^3 \theta}{4\pi h^2}, \tag{3.36}$$

and θ should now be the angle made by the ray connecting the source and the center of A_{int}. If we consider a single collimator hole (Fig. 3.12), A_{int} will be the intersection between the detector pixel and the projection from the point source onto: 1) the hole's entrance opening and 2) the hole's exit opening. This is equivalent to the reasoning we did in Section 3.2 for the sensitivity of a pinhole/lofthole. We then repeat the process for those collimator holes that project onto the detector pixel.

We are interested in using this method to obtain the system matrix elements, i.e. the sensitivity of each detector pixel to each image voxel. Since, in reality, a voxel is not a point source, in our modeling we approximate the voxels by 8 point sources, in order to better simulate their cubic shape. To get the different projections needed to calculate A_{int}, we project the hole openings from the point source onto the detection plane. In this dissertation we restrict ourselves to holes that have a rectangular cross-section, so the intersections on the detector plane are easy to compute (trapezoids). A_{int} is computed for each individual point source, pixel and collimator hole (since each hole has a distinct shape). To take penetration into account, instead of the real height of the holes we shorten the entrance and exit positions by the same amount, such that the total height of the hole is the effective height $a_e = a - 2/\mu$ [92]. As a final step, we multiply the final sensitivity value by a factor corresponding to the detector efficiency, and the projections are blurred with a 2D Gaussian kernel with a FWHM corresponding to the intrinsic detector resolution.

3.3.2 Simulations

In this section we simulate the innovative parallel-hole SPECT systems that are described in chapters 5 (cylindrical system) and 7 (hexagonal system). In Fig. 3.13 we show schematic representations of the two systems. For a detailed explanation of these system geometries we refer the reader to those chapters. The reason why these systems are simulated here is to show that we can reliably use the method described in Section 3.3.1 to model them in the simulations we perform in chapters 5 to 7. The image and detector dimensions are also as described in chapters 5 and 7.

To validate the analytical method, we use Monte Carlo simulations as the gold-standard method. This is more realistic than the ray-tracer method used for validation in Section 3.2, as explained in Section 2.4. Even though Monte Carlo-based methods are more time-consuming, the applications shown in this section are quite important, since they are at the basis of most results presented in chapters 5 to 7 of this dissertation, so a more thorough validation was essential.

The systems are modeled with the Monte Carlo-based simulation software GATE (Geant4 Application for Tomographic Emission) [82], version 6.1. A single collimator slice (as shown in Fig. 3.13) is built by inserting, in a mother volume of air, the collimator septa between the holes in that slice: to make one sector within the slice, the septa are defined individually, as blocks of lead with different pre-computed heights, and triangular blocks of material are defined on the edges of the sector to separate it from the others; then a ring repeater is used to obtain the other two sectors in the slice. To separate this slice from the next there should be a layer of lead with the thickness of the septa, and to achieve this we insert a hollow cylinder with the height of the septa and the thickness of our collimator. To obtain the entire collimator, this slice is repeated with the translation and rotation corresponding to each of the other slices.

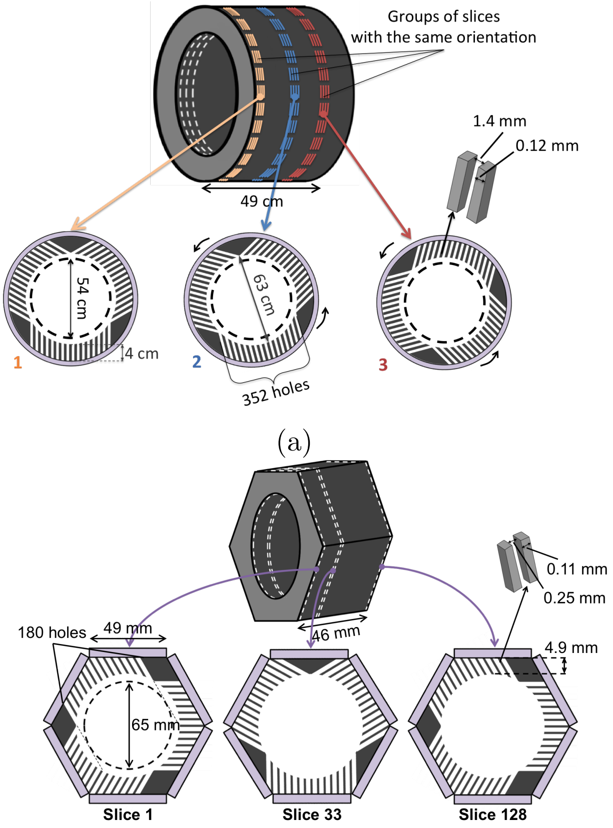
Groups of slices
with the same orientation
1.4 mm
0.12 mm
49 cm
54 cm
4 cm
63 cm
352 holes
1
2
3
180 holes
49 mm
46 mm
0.11 mm
0.25 mm
4.9 mm
65 mm
Slice 1
Slice 33
Slice 128

(a)

(b)

Figure 3.13: Schematic representation of the SPECT systems developed in chapters 5 and 7 (not to scale). The main collimator body is shown, along with a view of some of its transaxial slices. (a) Cylindrical system (Chapter 5); (b) Hexagonal system (Chapter 7).

Our goal is to validate the system matrix, which gives us, for each image voxel, the corresponding projection onto the system's detector. We therefore simulate cubic-shaped uniform sources in GATE, each having the same size as one image voxel, to exemplify the effect of the projector model at several representative voxel positions. The simulated amount of activity and time are chosen high enough for the effect of noise in the GATE simulations to be minimal. Due to the small size of the objects considered, phantom attenuation was not modeled. Furthermore, we remove the depth of interaction effect in the detector, in order to simulate the collimator response by itself.

The cylindrical system simulated here is the model described in chapter 5 for human full-body imaging. The detectors are NaI 3/8" crystals (90% efficiency for $^{99m}\mathsf{Tc}$) with an intrinsic resolution of 3 mm. In this case we simulate two cubic-shaped sources with 1 mCi of $^{99m}\mathsf{Tc}$, one at the center and one at the edge of the FOV. The sources are scanned for $10\,s$ at 10 different axial positions, placed at intervals of 4.9 cm.

The hexagonal system is described in chapter 7, and is intended for small-animal imaging. The detectors are NaI, with an 80% efficiency for $^{99m}\mathsf{Tc}$ and an intrinsic resolution of 0.8 mm [108]. We consider three cubic-shaped sources with 1 mCi of $^{99m}\mathsf{Tc}$, placed in the transaxial plane at positions $[0, -32.5]$ mm, $[0, 0]$ mm and $[0, 32.5]$ mm (bottom, center and top of the FOV). For each bed position, the sources are positioned, in the axial direction, at the center of each of the 128 collimator slices, and they are scanned for $12\,s$ per bed position.

3.3.3 Results and Discussion

3.3.3.1 Cylindrical System

In the experiments, the projections of two cubic sources with the size of an image voxel are simulated in GATE, at 10 different axial bed positions (at intervals of 4.9 cm). Their position in the transaxial plane can be seen in Fig. 3.14 (a): the first column of each figure corresponds to a source located at the center and the second column to one at the edge of the transaxial FOV, in the horizontal direction.

We first observe, in Fig. 3.14 (b) and (c), projection images with the data gathered from the 10 bed positions, using the analytical and GATE modeling respectively. In these images the vertical axis corresponds to the axial direction of the system and the horizontal axis to the circumference around the collimator in the transaxial plane. For each axial bed

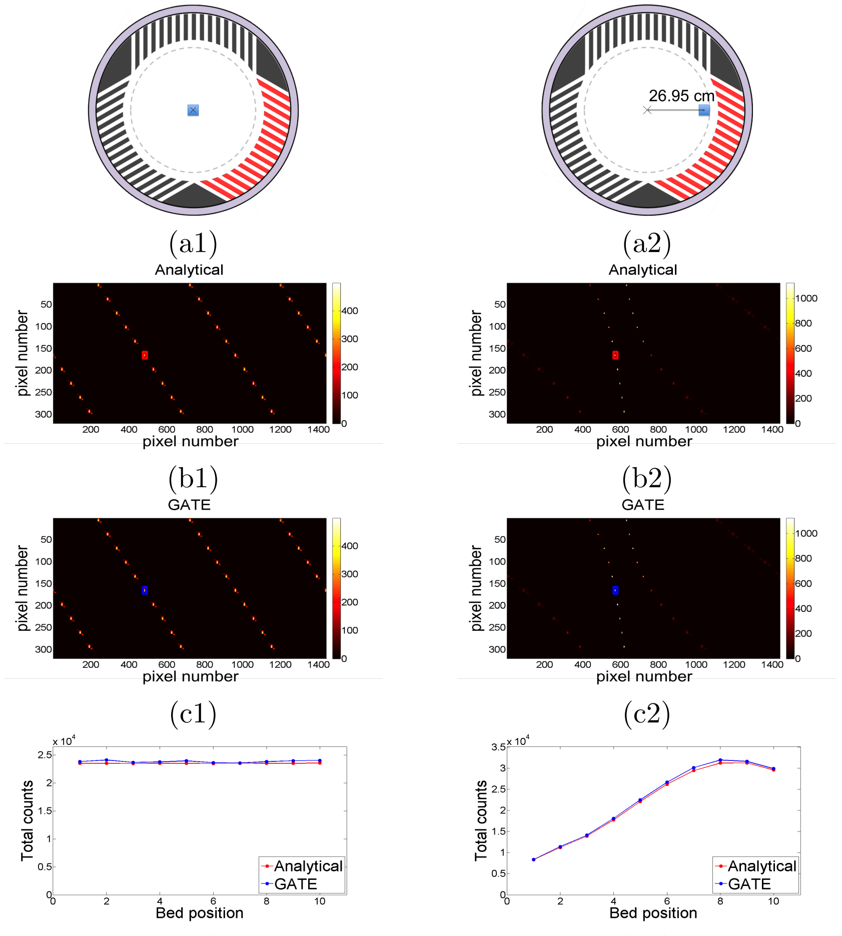

(a1) (a2)

(b1) (b2)

(c1) (c2)

(d1) (d2)

Figure 3.14: Projections of a voxel in the cylindrical system, where columns 1 and 2 correspond to different voxel positions. (a) shows a schematic representation of the voxel position considered, at slice group 21. (b) and (c) show, respectively, the corresponding analytical and GATE projections onto the detector for 10 different axial positions of the source. (d) shows a plot of the total number of counts through the highlighted sector of the collimator for these 10 axial bed positions, in both the analytical and GATE projections.

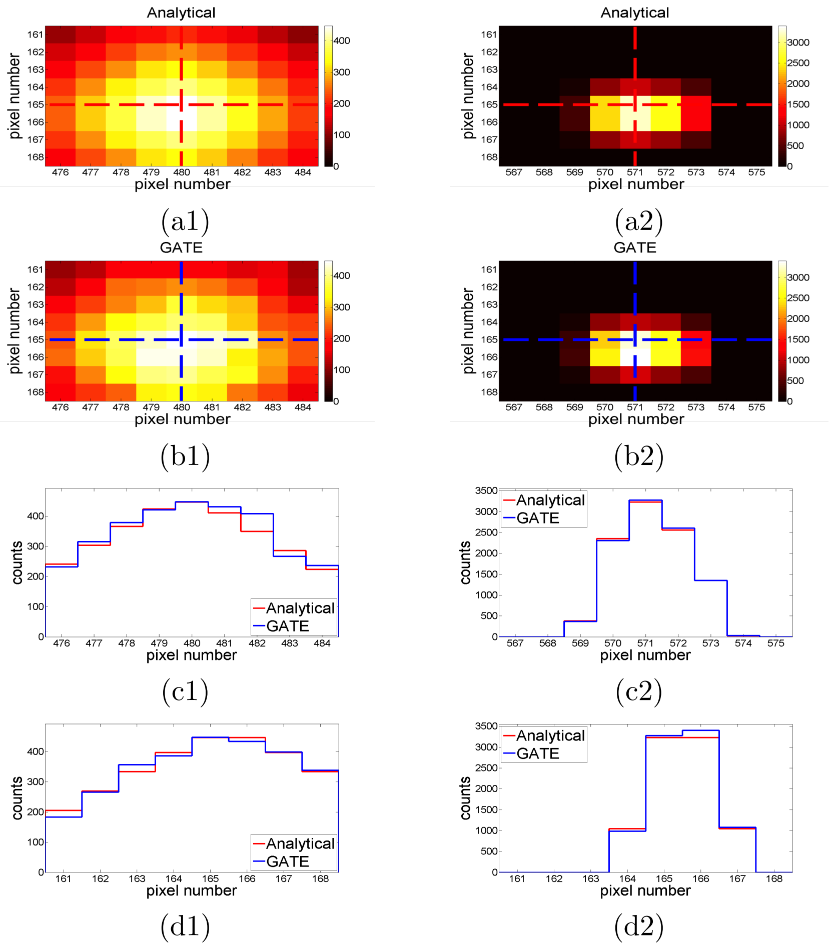

(a1) (a2)

(b1) (b2)

(c1) (c2)

(d1) (d2)

Figure 3.15: Zoomed-in view of the projections shown in Fig. 3.14, where columns 1 and 2 correspond to the voxel positions shown in Fig. 3.14 (a1) and (a2). (a) and (b) show a zoomed-in view of the analytical and GATE projections, respectively. The region of the projection which is zoomed-in is highlighted in Fig. 3.14 (b) and (c). (c) and (d) show line profiles in the transaxial and axial directions of the detector, respectively, in both the analytical and GATE projections. The profiles are taken through the dashed lines in subfigures (a) and (b).

position of the source (vertical axis), the projection through the three different collimator sectors results in three spots at the same vertical position but separated along the horizontal direction. We can see that the behavior of the projections is very similar for the two types of modeling.

We then present, in Fig. 3.14 (d), the total number of counts through one of the collimator sectors, highlighted in red in Fig. 3.14 (a), as a function of the bed position of the source. We see that the count number matches quite well, with an error of $\sim$ 1% or lower for each bed position.

In Fig. 3.15 (a) and (b) we take a closer look at one of the individual projections, indicated as a red/blue square in Fig. 3.14 (b) and (c) respectively. This is the projection through the collimator sector highlighted in red in Fig. 3.14 (a), when the source is positioned at the center of the 21st slice group (close to the center of the system). Line profiles through this region of the projection are then shown in Fig. 3.15 (c) and (d), and we can see again a very good match between the analytical and GATE modeling.

3.3.3.2 Hexagonal System

In this second study, we placed the small voxel-sized sources at the bottom, center and top of the FOV, as shown in Fig. 3.17 (a), and translated them for 128 bed positions (at intervals of 0.36 mm).

In Fig. 3.16 we show the total sensitivity of the bottom detector to each cubic source as a function of bed position, for the analytical and the GATE modeling, and we observe a good match between the two approaches.

In Fig. 3.17 (b) and (c) we show, for the 33rd bed position (centered at the 33rd collimator slice), a partial view of the projection onto the bottom detector for the analytical and GATE modeling, respectively. In (d) we show the line profiles through the dashed line in the projection images. We can see, both from the projection images and the line profiles, that the projections match quite well, even though the GATE projection is noisy.

In both Fig. 3.16 and 3.17, we see that the analytical model slightly overestimates the realistic projection for voxels very close to the detector and collimator (subfigures (1)), probably because for this voxel the point source approximations are the least accurate.

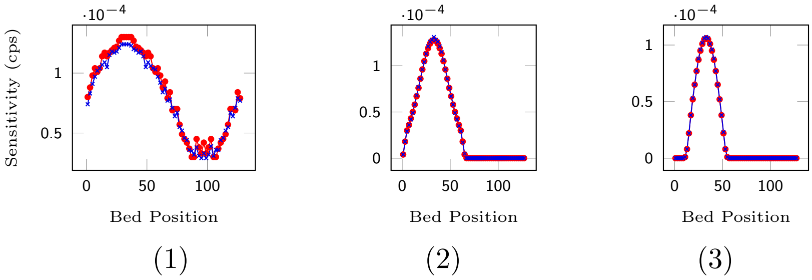

Figure 3.16: Sensitivity of the bottom detector to the cube phantom at bed positions corresponding to the center of each of the 128 transaxial collimator slices, using the analytical (red) and GATE (blue) modeling. Subfigures (1) to (3) correspond to the phantom positions shown in Fig. 3.17 (a1) to (a3), respectively.

3.3.3.3 Final Remarks

In Section 3.3.1 we described an analytical method which takes into account the geometrical features of complex parallel-hole collimators. In particular, it considers the non-standard shape of the holes, their different lengths and their different perpendicular distances to a given point in the reconstruction FOV. The advantage with regards to ray-tracer methods is that it only requires us to do the calculations once for each voxel-pixel pair, while keeping a high accuracy (as long as the geometry is correctly characterized). The method is also flexible enough to be used for any system geometry and any shape of collimator holes.

Here we validated this approach by comparing it with the results obtained from realistic GATE simulations. We analyzed both the shape of the projections and the total number of counts, to show that the analytical method can be used reliably to predict the approximate system response both qualitatively and quantitatively. Based on these results, the method will later be used to evaluate the systems in chapters 5 to 7.

Note that here we only analyze the accuracy of the analytical method in terms of modeling the collimator geometry, not the detector. However, in this dissertation we are interested in evaluating the collimator concepts and so we are mainly interested in the modeling of the pure geometric sensitivity of the collimator and of the angular sampling. In the real system, on the other hand, the most advisable approach for reconstruction would be to use an empirically determined system matrix, based on the measurement of a large number of point source projections

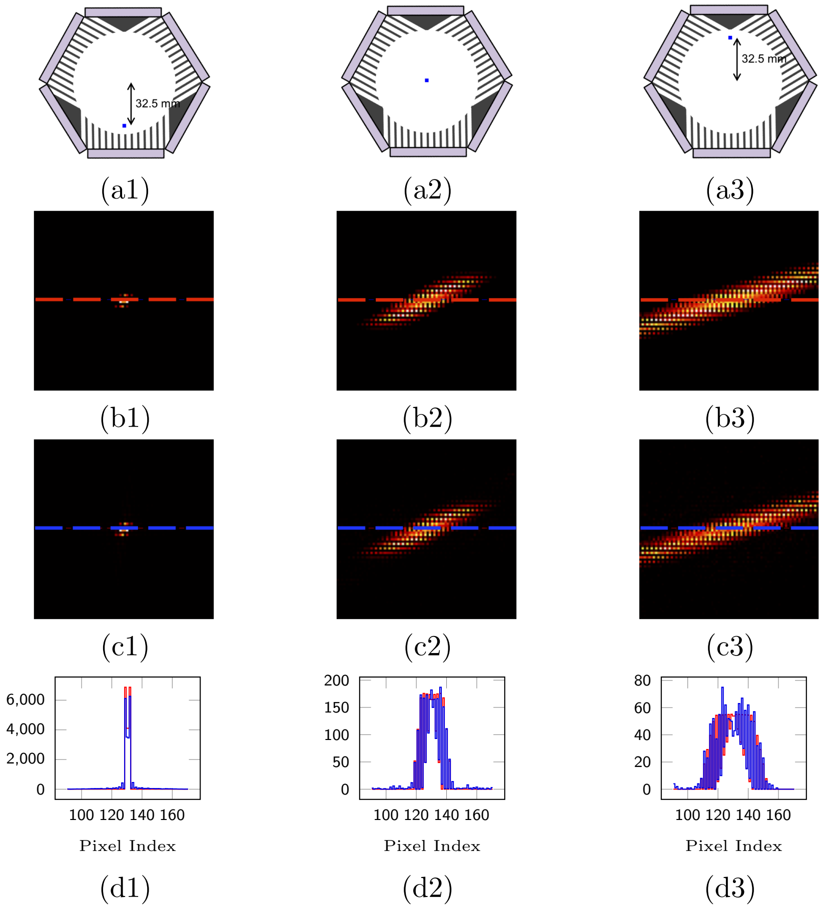

Figure 3.17: Projection of a voxel cube onto the bottom detector, where columns 1 to 3 correspond to different voxel positions. (a) shows a schematic representation of the voxel position considered. (b) and (c) show a zoomed-in view of the analytical and GATE projections, respectively. (d) shows the line profile through the dashed line in both the analytical (red) and GATE (blue) projections.

sequentially positioned in the field of view (see e.g. [87]), since the complex system geometry makes the reconstruction more sensitive to any mismatch between the ideal and real systems. This is what we do in fact in Section 7.5, with the first prototype system.

3.4 Summary and Original Contributions

In this chapter we developed accurate and efficient analytical methods to compute the geometric collimator response to a point or image voxel, for systems whose geometrical peculiarities make the modeling more challenging than standard (pinhole and parallel-hole) SPECT systems. With different validation approaches, we showed that these methods closely match the real system response (assuming an exact geometry).

The work described in this chapter is used for the system modeling and reconstructions in the remainder of this dissertation. In particular, the method described in Section 3.2 is used for pinhole SPECT in Chapter 4, and Section 3.3 is used for a standard parallel-hole system in chapters 4 and 6, for the cylindrical system in chapters 5 and 6 and for the hexagonal system in Chapter 7.

This work has been published as part of several journal and conference publications. The application to pinholes/loftholes is described in a peer-reviewed A1 journal publication [37] and a conference abstract [109], in the context of the development of the lofthole collimator developed by Karel Deprez. Figures 3.3 to 3.8 were created by Karel Deprez. The application to the cylindrical parallel-hole system has been published in a peer-reviewed A1 journal [110], and the application to the hexagonal system in a conference proceeding [111]. The system modeling and simulations shown here for the cylindrical parallel-hole system were performed by Tiziana Zedda.

Chapter 4

Evaluation of Fisher Information Matrix-based Methods for Fast Assessment of Image Quality in SPECT

In this chapter we compare the accuracy of different methods that use the Fisher Information Matrix for evaluation of image quality (IQ) in SPECT. Some of the methods and results obtained in this chapter will also be used in Chapter 6.

The chapter is organized as follows. Section 4.2 reviews the theoretical framework behind the local shift-invariant, the non-uniform object-space pixelation, and the subsampled approximations of the Fisher Information Matrix. In Sections 4.3 and 4.4 these approximations are applied to standard parallel-hole and pinhole SPECT systems, respectively. Each of these sections starts with the description of the characteristics of the imaging system and the phantoms considered, as well as the details regarding the simulations and calculations performed, and then we compare the performance of each approximation method. Finally, in Section 4.5 we derive general insights from all the results acquired with both SPECT systems, and give some guidelines to help in the selection of the most appropriate methods.

4.1 Introduction

In order to optimize and compare SPECT systems, or the protocols to be followed, we have to define a reliable measure for their respective IQ. For this purpose it has become common to consider the local impulse response (LIR) and the covariance at voxels of interest of the image estimator as measures of resolution and noise at those voxels, respectively, as well as for task-based assessment of IQ. For maximum likelihood (ML) or penalized maximum likelihood (PML) estimation, reconstruction techniques commonly used in emission tomography, it is not possible to precisely evaluate these quantities. As such, the most accurate way of estimating them is by running reconstructions until convergence for a very large number of noise realizations of the projection data, making the method too time-consuming for most applications (e.g. to compare many different system configurations or to guide an adaptive system in real-time).

Therefore, it is more practical to use analytical approximations to the LIR and the covariance at convergence. Such approximations have been derived by Fessler *et al.* [90, 57], and for the reconstruction of emission tomography data using PML they are given by expressions (2.27) and (2.28) in Chapter 2. In this case the calculations involve the inverse of a matrix of the same size as the Fisher information matrix (FIM). This means that the higher the number of voxels in the image the higher their complexity, and in practice it becomes imperative to use further approximations to apply these analytical calculations to $3D$ PET and SPECT systems, at least with the currently available computing power.

The most popular of these approximations is the local shift-invariant (LSI) approximation of the FIM. It stems from the assumption that shift-variant systems could be considered as being locally shift-invariant, which was first proposed for PET by Fessler and Booth [112] and then applied to simplify the calculation of the LIR and covariance by Qi and Leahy [113]. The LSI method keeps the size of the FIM but reduces the complexity of the calculations by using the properties of circulant matrices. It was initially applied in $3D$ PET [113], and later in $3D$ SPECT [114, 115, 116]. Since then the approach has been frequently used in system design and comparison, especially in PET systems, with some variability in the way the approximation is applied. A particular LSI method is commonly validated for a specific system by comparing its results with the values obtained from the reconstruction of noisy projections.

Other alternative approximations have been proposed in literature as an alternative to the LSI, namely the non-uniform object-space pixelation (NUOP), from Meng and Li [117, 118], and the subsampled FIM, from Fuin, Pedemonte *et al.* [119]. The idea behind these two methods is to approximate the FIM by a smaller matrix, thus making it easier to invert. Yet these approaches have not been widely applied, since until very recently it seemed that the LSI approximation could be used under any circumstances. However, the results from Fuin, Pedemonte *et al.* [119] have challenged this idea, by showing that the LSI does not correctly reflect the effect of activity outside the central field of view (CFOV) in the IQ of a reconstructed SPECT image.

In this chapter we analyze the assumptions behind the LSI and the imaging situations in which they could be violated, and we compare its performance when predicting several figures of merit for IQ with that of the NUOP and subsampled FIM approaches, which do not require such conditions for validity. We will first investigate the case of a standard parallel-hole SPECT system, and then a single-pinhole system. Our goal is to show the necessity of considering alternative approaches to the LSI approximation of the FIM, even in cases where intuitively its assumptions might seem to be valid.

4.2 Methods

Section 2.5.2 reviews the theoretical framework behind Fessler's FIM-based analytical evaluation of the LIR and covariance. The final results which we use as a basis for this chapter are equations (2.31) and (2.32), corresponding to the LIR and the covariance, respectively.

Unfortunately, in $3D$ emission tomography it is commonly not feasible to perform these FIM-based calculations directly. This is because we need to invert an $N \times N$ matrix, $[\mathbf{F} + \beta\mathbf{R}]$, and N, the total number of voxels in the image, is a very large number. To alleviate this issue, researchers have suggested additional approximations that could be applied to the FIM in order to simplify the calculation of (2.31)-(2.32), which we present in the following subsections.

4.2.1 Local Shift-Invariance

The most wide-spread method used in shift-variant PET and SPECT systems for the approximation of the FIM in expressions (2.31)-(2.32) is the local shift-invariance (LSI) approach [112, 113]. Its application involves two main assumptions [113]:

1st: If we take a single column of the FIM with an index j, $\mathbf{F}^j$, and represent it in $3D$ image-space, the column elements with a high value will be constrained to the vicinity of the voxel of index j. In other words, the correlation between voxel j and voxels which are not very close to it is negligible;

2nd: FIM columns corresponding to neighbor voxels are very similar between each other, after the corresponding voxel shift (local shift-invariance).

If these assumptions are correct, then the following approximations should be valid:

a) The 1st assumption implies that the main contributions to the calculation of the LIR (2.31) and covariance (2.32) corresponding to voxel j should come from the FIM column of index j and the columns associated with the neighboring voxels. As such, only these columns need to be accurately computed;

b) From the 2nd assumption, we can approximate the FIM columns associated with the neighboring voxels by a shifted version of $\mathbf{F}^j$;

c) From a) and b) it follows that the result given by (2.31)-(2.32) is not considerably changed if the FIM is to be replaced by a Toeplitz-block-Toeplitz matrix whose jth column is equal to $\mathbf{F}^j$ (and its other columns are $3D$ Toeplitz shifts);

d) Finally, the 1st assumption also implies that, as long as voxel j is far enough from the edge of the image, the column elements close to the edges should be close to zero. As such, the Toeplitz-block-Toeplitz matrix from c) can be replaced by a circulant-block-circulant (CBC), since for the relevant columns (jth and neighbors) the two will be equivalent. Note that this approximation is therefore not valid for points close to the edge of the image.

From this sequence of approximations, we get to the core of the LSI approach: it replaces the FIM in (2.31)-(2.32) by a CBC matrix. The reason why we want to write the FIM in such a way is because a circulant matrix is diagonal in Fourier space, and its diagonal elements, the eigenvalues λ_k, are simply given by the Fourier transform of its first column. As such, the LSI approximation of the FIM can be written as

$$\mathbf{F}_{LSI}(j) = \mathbf{Q}^{-1} \mathrm{diag} \left[\lambda_k^F \right] \mathbf{Q}, \tag{4.1}$$

with $\mathbf{Q}$ the $3D$ discrete Fourier transform (DFT) matrix and

$$\lambda^F = \mathbf{QF}_{LSI}(j)^1, \tag{4.2}$$

which can be easily computed from column $\mathbf{F}^j$ using fast DFTs (the superscript ^{1} denotes the first column). A similar approximation can be done for the Hessian matrix $\mathbf{R}$, whose eigenvalues we denote by λ_k^R, and since in this chapter we consider a first-order homogeneous quadratic prior $\mathbf{R}$ is already nearly CBC. Using these approximations, computing the inverse becomes trivial, and it can be shown [113] that the elements of LIR (2.31) and the covariance (2.32) of voxel j are then approximated by

$$l_{j'}^{j}(\hat{\mathbf{f}}) \approx \mathbf{e}^{j'T}\mathbf{PQ}^{-1}\mathrm{diag}\left[\frac{\lambda_k^F}{\lambda_k^F + \beta\lambda_k^R}\right]\mathbf{Qe}^j, \tag{4.3}$$

$$Cov_{j'}^{j}(\hat{\mathbf{f}}) \approx \mathbf{e}^{j'T}\mathbf{PQ}^{-1}\mathrm{diag}\left[\frac{\lambda_k^F}{\left|\lambda_k^F + \beta\lambda_k^R\right|^2}\right]$$

$$\mathbf{QP}^T\mathbf{e}^j, \tag{4.4}$$

where $|\cdot|$ denotes the complex modulus, which is in general much faster to compute than (2.31)-(2.32).

In practice, additional adaptations have been proposed to apply the LSI approach, with different purposes. First of all, there is the issue that this approximation may lead to unphysical results, such as negative variance values – and in fact it does in the cases we consider here – due to the fact that the CBC approximation of the FIM will in general no longer have non-negative real eigenvalues; to solve this, we consider the solutions which have been proposed in literature [113, 104], as well as a few methods which seem intuitive to us. Secondly, some steps have been suggested in order to improve the accuracy and stability of the method [104, 120]. Lastly, some have suggested additional approximations to speed up the calculations [113, 116], but we have not considered those here in order to limit the degree of approximation. Since the adjustment of the eigenvalues is required in order to use the LSI approach, but different sources use different methods, we consider the 3rd main assumption of the approach as being the validity of the chosen adjustment method. In the following we describe the five methods which we test in this chapter to compute the eigenvalues λ_k^F to be used in (4.3)-(4.4).

1) Non-Negative Real Part of Eigenvalues The first method we consider is to keep only the real part of the eigenvalues (4.2), and then replace the negative values by zero

$$\lambda_k^F \to \max\left(0, \Re\left(\lambda_k^F\right)\right). \tag{4.5}$$

2) Absolute Value of Eigenvalues Another option is to consider the complex magnitude of the eigenvalues

$$\lambda_k^F \to \left|\lambda_k^F\right|. \tag{4.6}$$

3) Symmetric FIM This was the first method actually proposed for $3D$ shift-variant systems, by Qi and Leahy in [113], where it was tested in a PET system. The approach consists of making the FIM both CBC and symmetric, since the original FIM is symmetric and the LSI approximation will (in general) break this symmetry. To do this we take $\mathbf{F}^j$ (seen as a $3D$ image), we shift its voxels so that voxel j becomes the center voxel, and then force this image to be symmetric with regards to the center (in $3D$) by equating the value of each pair of symmetric elements to their maximum [113]. This is our new approximation for $\mathbf{F}^j$ (but with voxel j in the center), and to obtain $\mathbf{F}_{LSI}(j)^1$ we circulantly shift the image so that our original voxel j becomes voxel 1. To get the eigenvalues (4.2), we apply a $3D$ DFT to this new image. Finally, we take the real part of the λ_k^F's and the negative values are truncated to zero, as before in (4.5). Note that making the column itself symmetric is necessary in order to make the CBC approximation of the FIM symmetric.

4) Eigenvalues with Positive Real Part Another technique is to remove the eigenvalues with a non-positive real part

$$\lambda_k^F \to \begin{cases} \lambda_k^F, & \Re\left(\lambda_k^F\right) > 0 \\ 0, & \Re\left(\lambda_k^F\right) \leq 0 \end{cases}. \tag{4.7}$$

This has been suggested, in a slightly different form, by Vunckx *et al.* [104], in the context of pinhole SPECT. The reason behind it is that the authors found that "frequencies with $\Re\left(\lambda_k^F\right) < 0$ have a negative influence on the accuracy and the stability of the approximations" [104].

5) Eigenvalues with Positive Real Part & Spatial Window In addition to the previous method, in [104] a spatial window function $W(j)$ is applied, with j the voxel of interest chosen, which the authors also found to improve their results in pinhole SPECT [104, 120]. The value of this function at a voxel k, with $3D$-coordinate vector $\vec{x}_k$, is given by [120]

$$W(j)_k = \max\left(0, 1 - \frac{|\vec{x}_j - \vec{x}_k|}{n}\right), \tag{4.8}$$

where $|\cdot|$ is the vector magnitude and n the linear dimension of the image-space, so $W(j)_k$ decreases from 1 to 0 as the distance between voxels j and k increases. The idea here is to reduce the effect of the LSI approximation errors, which should be larger for points further away from the point of interest, and so before we apply the CBC approximation we weigh each element k of the column image $\mathbf{F}^j$ by the corresponding value of the spatial window function $W(j)_k$. This weighted column is then used to compute the eigenvalues λ_k^F, and to conclude we apply (4.7) like in the previous method.

In order to obtain the LSI-based values, before inserting the eigenvalues (4.2) in equations (4.3)-(4.4) we apply one of the methods $1-5$ described here. From this point on we refer to these methods as LSI - M1 to M5, respectively.

4.2.2 Non-Uniform Object-Space Pixelation

In the non-uniform object-space pixelation (NUOP) method, suggested by Meng and Li [117], the image-space is divided in non-uniformly sized "voxels". In particular, the voxel size increases as we go to regions further away from the region of interest (ROI). In this way we keep approximately the same IQ in the ROIs as when the image is divided into voxels with the smallest size considered, but the system modeling becomes much more efficient [117]. In other words, this means that we can reduce the size of the image-space from N to P, with $P < N$, thereby reducing the size of the FIM to $P \times P$, while still obtaining a good evaluation of IQ in the ROIs using (2.31)-(2.32).

To apply the NUOP, we start with a uniform image-space, of size N, whose voxels have the smallest size that we want to consider. Afterwards the image-space is divided in regions according to how many voxels we want to group together to form larger voxels (the rebinning strategy). We then go through the entire image-space (N voxels), starting with the regions that will correspond to the largest voxels. Neighboring voxels within the same region and with a similar activity value are grouped together to form a cube (when possible), and this larger voxel is given a new index $m \in \{1, \dots, P\}$ in the non-uniform image-space. For a more detailed explanation of the algorithm see [117].

We use the approach described in [118], where an $N \times P$ transformation matrix $\mathbf{S}$ is introduced. This matrix has only one non-zero element per row l, $l \in \{1, \dots, N\}$. This element has value 1 and corresponds to column m, with $m \in \{1, \dots, P\}$ the index that voxel l takes in the new (non-uniform) image-space. In general, each index m corresponds to several l indices ($P < N$). The $M \times P$ NUOP system matrix can then be given by

$$\mathbf{H}_{NUOP} = \mathbf{HS}. \tag{4.9}$$

To have a mean projection $\overline{\mathbf{g}} = \mathbf{Hf} = \mathbf{H}_{NUOP}\mathbf{f}_{NUOP}$, the NUOP image is related to the original image vector $\mathbf{f}$ by

$$\mathbf{f} = \mathbf{S}\mathbf{f}_{NUOP}. \tag{4.10}$$

From these we get a FIM

$$\mathbf{F}_{NUOP} = \mathbf{H}_{NUOP}^{T}\mathrm{diag}\left(\frac{1}{\overline{g}_i}\right)\mathbf{H}_{NUOP} = \mathbf{S}^T\mathbf{FS}, \tag{4.11}$$

and the NUOP Hessian matrix of the penalty is defined as

$$\mathbf{R}_{NUOP} = \mathbf{S}^T\mathbf{RS}. \tag{4.12}$$

Applying (4.10) to the vector $\mathbf{P}^T\mathbf{e}^j$ we get

$$\mathbf{P}^T\mathbf{e}^j = \mathbf{S}\left(\mathbf{P}^T\mathbf{e}^j\right)_{NUOP}, \tag{4.13}$$

and since the $P \times P$ matrix $\mathbf{S}^T\mathbf{S}$ is equal to the identity matrix for the columns corresponding to the voxels which keep the same size in the NUOP, i.e. the points in the ROI, we have

$$\mathbf{S}^T\mathbf{P}^T\mathbf{e}^j = \mathbf{S}^T\mathbf{S}\left(\mathbf{P}^T\mathbf{e}^j\right)_{NUOP} = \left(\mathbf{P}^T\mathbf{e}^j\right)_{NUOP} \tag{4.14}$$

as long as j is the index of a voxel inside the ROI. We can then write the NUOP equivalent of (2.31)-(2.32), for voxels j and j' inside the ROI, as

$$\begin{aligned} I^{j}_{j'}(\hat{\mathbf{f}}) \approx\, & \mathbf{e}^{j'T}\mathbf{PS}[\mathbf{F}_{NUOP} + \beta\mathbf{R}_{NUOP}]^{-1} \\ & \mathbf{F}_{NUOP}\mathbf{S}^{T}\mathbf{e}^{j}, \qquad (4.15) \\ Cov^{j}_{j'}(\hat{\mathbf{f}}) \approx\, & \mathbf{e}^{j'T}\mathbf{PS}[\mathbf{F}_{NUOP} + \beta\mathbf{R}_{NUOP}]^{-1}\mathbf{F}_{NUOP} \\ & \left([\mathbf{F}_{NUOP} + \beta\mathbf{R}_{NUOP}]^{-1}\right)^{\dagger}\mathbf{S}^{T}\mathbf{P}^{T}\mathbf{e}^{j}, \qquad (4.16) \end{aligned}$$

where the FIM, the Hessian matrix and the $\mathbf{e}^{j}$ / $\mathbf{P}^{T}\mathbf{e}^{j}$ vector were replaced by their corresponding versions in the NUOP. Formulas (4.15) and (4.16) can significantly increase the efficiency of the calculation of the LIR and the covariance at voxel j, since they only require the inversion of a $P \times P$ matrix. This matrix is easily computed using the system matrix $\mathbf{H}$, the projection data $\overline{\mathbf{g}}$ and expressions (4.11) and (4.12).

Note that, in order to guarantee the accuracy of this approach, only voxels with similar activity values can be grouped together. This is the main assumption behind the NUOP, and so the user can include this condition in the algorithm to ensure the best results. However, with a realistic phantom it is usually necessary to relax this condition (outside of the ROI) in order to reach a sufficient speed up.

4.2.3 Subsampled Fisher Information Matrix

In the Subsampled FIM approach, put forward by Fuin, Pedemonte *et al.* [119], we select a subset $G \subset \{1, ..., N\}$ of the voxel indices which is distributed in a "grid" that in general covers the whole image-volume. Then the FIM is reduced to the matrix elements corresponding to pairs of voxels that belong to the subset G. This means that we are in essence considering only the impulse responses / correlations between the voxels in this subset for the approximation of the LIR (2.31) and the covariance (2.32). The user is free to design the grid according to the desired level of accuracy, but when computing an element (j, j') we should make sure that $j, j' \in G$.

Mathematically, the subsampled FIM method can be described in a similar way as we used for the NUOP approach in Section 4.2.2. We define a transformation matrix $\mathbf{T}$, with $N \times N_G$ elements, which selects only the vector elements or the matrix columns corresponding to the indices of the image voxels which belong to the grid G. Then, following similar steps as the ones we discussed for the NUOP, the approximated

LIR and covariance become

$$\begin{aligned} l^j_{j'}(\hat{\mathbf{f}}) \approx\, & \mathbf{e}^{j'T}\mathbf{P}\mathbf{T}[\mathbf{F}_{sub}+\beta\mathbf{R}_{sub}]^{-1} \\ & \mathbf{F}_{sub}\mathbf{T}^T\mathbf{e}^j, \qquad (4.17) \\ Cov^j_{j'}(\hat{\mathbf{f}}) \approx\, & \mathbf{e}^{j'T}\mathbf{P}\mathbf{T}[\mathbf{F}_{sub}+\beta\mathbf{R}_{sub}]^{-1}\mathbf{F}_{sub} \\ & \left([\mathbf{F}_{sub}+\beta\mathbf{R}_{sub}]^{-1}\right)^{\dagger}\mathbf{T}^T\mathbf{P}^T\mathbf{e}^j, \qquad (4.18) \end{aligned}$$

where we just replaced $\mathbf{F}$ and $\mathbf{R}$ in (2.31)-(2.32) by their subsampled counterparts, $\mathbf{F}_{sub} = \mathbf{T}^T\mathbf{F}\mathbf{T}$ and $\mathbf{R}_{sub} = \mathbf{T}^T\mathbf{R}\mathbf{T}$, and applied $\mathbf{e}^j_{sub} = \mathbf{T}^T\mathbf{e}^j$.

Both the NUOP and subsampled FIM approaches share the fundamental assumption that in the regions where the sampling is sparse there are no abrupt changes in voxel value, so that we can use a single value for a group of voxels. As explained in Section 4.2.2, we can make a grid that avoids this issue by forcing it to have a finer sampling in regions with more variability. On the other hand, although the formulation presented here for the two techniques is similar, the corresponding transformation matrices $\mathbf{T}$ and $\mathbf{S}$ are inherently different because $\mathbf{T}$ has exactly N_G non-zero elements, while $\mathbf{S}$ has N. In essence, the difference between the two schemes is that in the subsampled approach the approximation is made at the level of the FIM, by only keeping some of the matrix elements, whereas in the NUOP it is made at the level of the image-space (in fact, it was originally presented as a method to speed up reconstruction [117]). Furthermore, the subsampled approach disregards voxels which do not belong to the grid, whereas the NUOP takes them into account (by averaging them out to get the new voxel value), which makes the subsampled approach easier to implement but slightly less accurate.

4.3 Parallel-hole SPECT

4.3.1 Simulations

4.3.1.1 System Modeling and Phantom

In this section we analytically simulate a SPECT system with similar settings to the Triple Head Human SPECT system Prism 3000 NewTec (Inter Medical), with the LEHR parallel-hole collimator. The holes have a square shape, with height 27 mm, width 1.3 mm and septal thickness

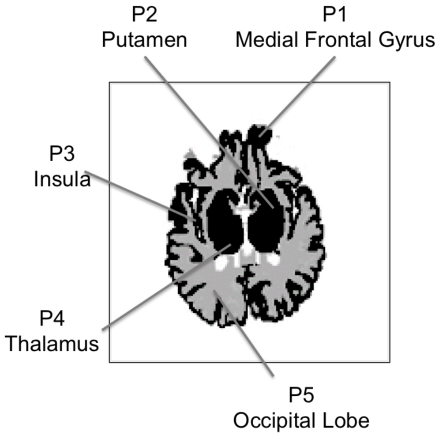

Figure 4.1: A transaxial view of the phantom considered (Hoffman), showing the voxels at which the CRC and variance are computed.

0.18 mm. The detectors are composed of 146 × 160 pixels (transaxial × axial) of 1.48 mm × 1.48 mm size, with a 1.5 mm intrinsic resolution. The image-space in the reconstruction is divided in $(1.48\,\mathrm{mm})^3$ voxels and has a total dimension of 146 × 146 × 98 voxels. The reconstruction FOV is a cylinder of 21.6 cm diameter and 14.5 cm height.

The system is modeled using the method described in Section 3.3.1 to obtain the system matrix $\mathbf{H}$. This is then used for both the analytical calculations of the figures of merit for image quality and the reconstructions.

The phantom considered is the digital Hoffman phantom with a total activity of 50 MBq of ^{99m}Tc-ECD, assuming a gray-to-white-matter ratio of 4:1 and a 5% brain uptake of a total injected activity of 1 GBq [121]. Only the 9 central transaxial slices of the phantom are considered, in order to reduce the calculation time. We compute the CRC and the variance at five voxels of interest P_1 to P_5, located on the central transverse plane of the image at the locations shown in Fig. 4.1. These voxels are chosen at some regions of interest in the brain: the Medial Frontal Gyrus (P_1), the Putamen (P_2), the Insula (P_3), the Thalamus (P_4) and the Occipital Lobe (P_5).

The scanning protocol consists of rotating the 3 cameras around the object for a total of 120 angular positions (1° angular step size), at a distance of 12.5 cm from the center (measured from the collimator surface). The total scanning time is 30 min.

Table 4.1: NUOP Rebinning Strategy

Distance to center of ROI (nr. voxels)	Rebinned voxels
15	$1 \times 1 \times 1$
$15 - 30$	$4 \times 4 \times 4$
> 30	$8 \times 8 \times 8$

4.3.1.2 Figures of Merit for Image Quality

We evaluate two figures of merit (FOMs) for IQ – the CRC and the variance – at the voxels of interest P_1 to P_5, after convergence of the PF-PML algorithm, both using a gold standard reference method and the different approximation methods described in Section 4.2. We chose a first-order uniform quadratic prior $R(\mathbf{f})$ [57] (see Section 2.3.4) with a regularization parameter $\beta = 10^{-6}$, and a filtering operator $\mathbf{P}$ corresponding to a $3D$ Gaussian blurring with $1\,\mathrm{cm}$ FWHM. The regularization parameter β is relatively large, to make sure that $[\mathbf{F} + \beta \mathbf{R}]$ is invertible even after possible numerical errors, since $\mathbf{F}$ itself is in general not invertible.

The gold standard for the CRC is based on a reconstruction of the noiseless projection of the original phantom, $\overline{\mathbf{g}}_1 = \mathbf{Hf}$, and a reconstruction from the noiseless projection of the original phantom with an extra impulse δ at voxel j, $\overline{\mathbf{g}}_2 = \mathbf{H}\left(\mathbf{f} + \delta \mathbf{e}^j\right)$, using formula (2.22)

$$l^j(\hat{\mathbf{f}}_{PML}) \approx \frac{\hat{\mathbf{f}}_{PF-PML}(\overline{\mathbf{g}}_2) - \hat{\mathbf{f}}_{PF-PML}(\overline{\mathbf{g}}_1)}{\delta}, \tag{4.19}$$

where the impulse δ was taken as having the same value as the original voxel intensity [122]. Then the CRC is simply the jth element of vector l^j. The gold standard for the variance is based on the reconstruction of 1000 noise realizations of the projection data, $\mathbf{g}$. These are independent realizations of pseudo-random data generated from the Poisson distribution with mean $\overline{\mathbf{g}}$. In both calculations, the reconstruction is done by running 1000 iterations of the one-step-late algorithm [53].

In the NUOP approach, the rebinning strategy was chosen as described in Table 4.1 [117, 118]. This table shows the maximum size of the group of adjacent voxels which are rebinned to the same voxel according to the region of image-space.

Lastly, the subsampled FIM is computed over two different grids G_1 and G_2, indicated as Sub FIM - G_1 and G_2 respectively. By not being limited to one type of grid, we can evaluate the accuracy of the method in a more general way. To be consistent with the literature, we consider a uniformly distributed grid G_1, spanning only a few axial slices around the voxel of interest, as described in [119]. This grid contains the image voxels whose indices in $3D$ have the same parity as the voxel of interest when summed (i.e. if the sum of the indices of the voxel of interest is an odd number, choose the voxels whose sum of indices is also odd). On the other hand, since the grid can be chosen in any way the user sees fit, we also consider a grid G_2 which is denser in the ROI, built, just like the NUOP, according to Table 4.1: we select one voxel per $N \times N \times N$ cube, such that within each region the grid points are uniformly selected. We expect this kind of grid to provide better accuracy at least for images in which the activity is mostly concentrated inside the ROI, which occurs in most situations studied in this chapter.

The error of all the calculation methods is computed for each voxel of interest, as a percentage of the gold standard value.

4.3.2 Results and Discussion

To evaluate the different FIM methods for approximating the gold standard, we present here the estimation results of the CRC and variance at the voxels shown in Fig. 4.1. We start with the LSI-based methods (M1 to M5), whose CRC and variance values are shown in Fig. 4.2 and 4.3 respectively. We can see that the CRC values are in general slightly overestimated by the methods, with the exception of LSI - M3 which shows a different behavior for P1 and P2. The relative error of the methods is in general very small, as confirmed by the values in Table 4.2 (error under 4%). As for the variance, the estimations are less accurate, as also seen in Table 4.3, which was to be expected since this FOM is more sensitive to the approximations of the FIM [120]. In particular, the LSI approaches usually overestimate the gold standard value. In this case, the approaches produce more distinct accuracies, with LSI - M3 showing the worst results (between 6% and 30%) and LSI - M4 and M5 with relatively low error values (under 4%).

In Fig. 4.4 and 4.5 we show the CRC and variance values corresponding to the alternative approximation methods (NUOP and subsampled approach), and the relative errors are again shown in tables 4.2 and 4.3. We observe that the NUOP and Sub FIM - G_2 methods show a very low error in both cases (always lower than 1%), which is lower than any LSI-based method at any voxel of interest. The Sub FIM - G_1 method

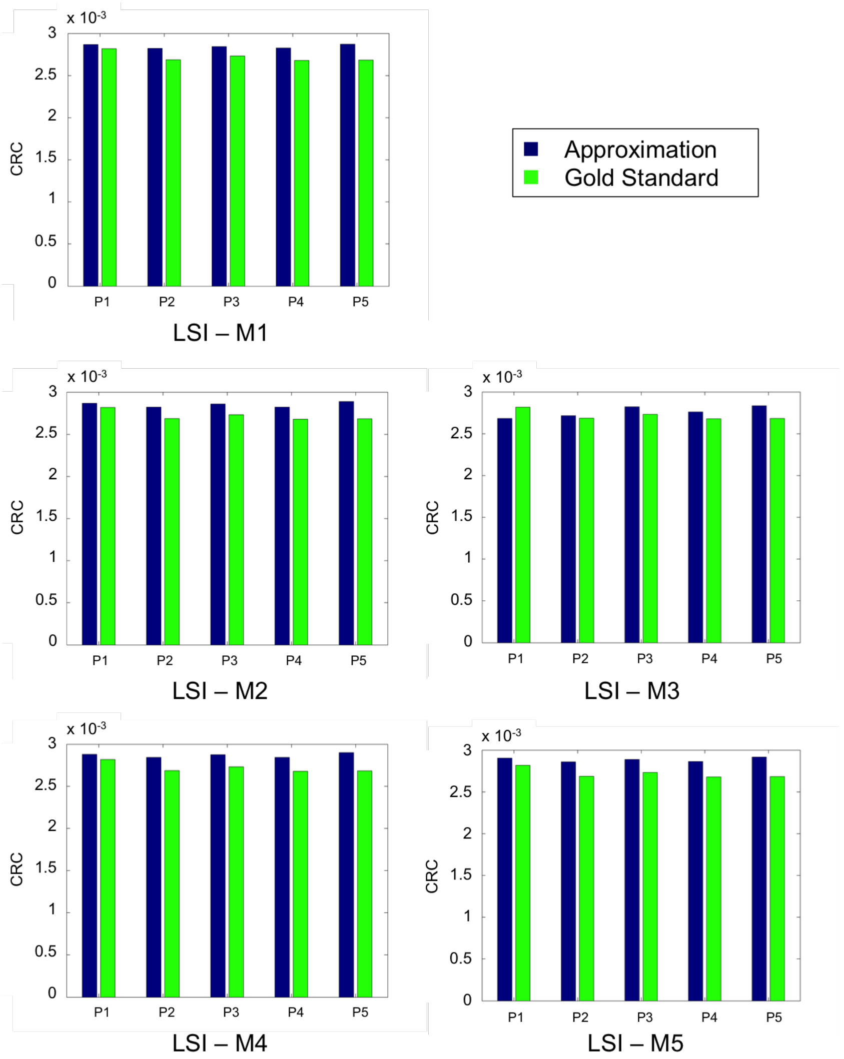

Figure 4.2: CRC values given by the different LSI approximation methods (blue) versus the gold standard value (green), where each subfigure corresponds to a different approximation method and each bar in the subfigure corresponds to a different voxel of interest.

performs a little worse, but it is still quite low (under 3%).

From this analysis, the first conclusion is that all the methods analyzed for approximating the FIM are quite reliable for the calculation of the CRC and variance with equations (2.31) and (2.32). This was to be expected for the LSI-based approaches, since there are many sources in

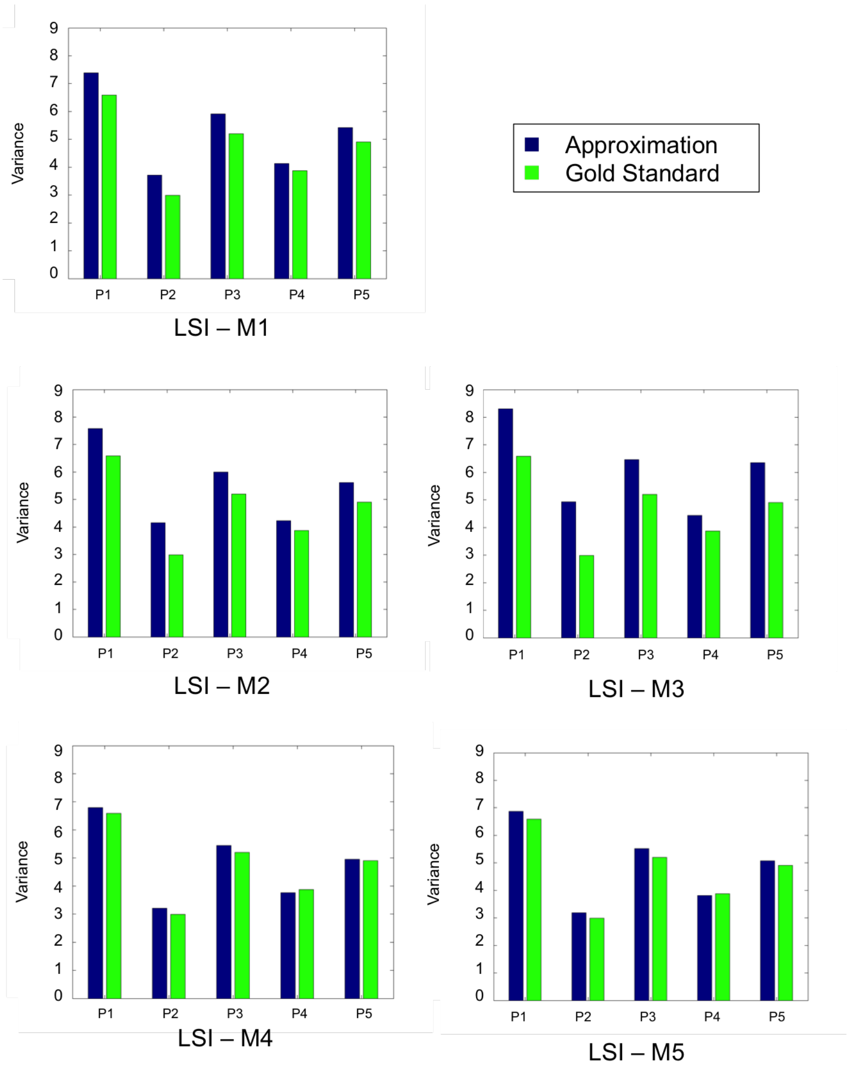
LSI – M1

LSI – M2

LSI – M3

LSI – M4

LSI – M5

Figure 4.3: Variance values given by the different LSI approximation methods (blue) versus the gold standard value (green), where each subfigure corresponds to a different approximation method and each bar in the subfigure corresponds to a different voxel of interest.

literature documenting their use in parallel-hole SPECT imaging [116, 123, 119], and was confirmed to be the case for the alternative methods as well. The LSI methods are clearly less accurate for the computation of the variance than of the CRC. The best performing methods are the NUOP and subsampled approaches based on a grid that is finer

Table 4.2: Error (%) of the CRC obtained from each approximation method at the voxels of interest.

VOI	LSI M1	LSI M2	LSI M3	LSI M4	LSI M5	NUOP	Sub FIM G_1	Sub FIM G_2
P_1	0.77	0.79	2.16	0.95	1.39	0.25	2.03	0.11
P_2	2.23	2.22	0.44	2.57	2.83	0.11	1.00	0.43
P_3	1.84	2.07	1.49	2.35	2.60	0.37	0.68	0.37
P_4	2.43	2.37	1.33	2.72	3.05	0.13	0.72	0.27
P_5	3.08	3.40	2.49	3.60	3.84	0.29	0.52	0.22

around the voxel of interest, and, from the LSI-based methods, M4 and M5 provide the best results, confirming the previous observations of [104, 120], and showing that the particular method chosen for the LSI approach does make a difference in the results.

A more extensive discussion of the different approaches is carried out in Section 4.4.3, after exploring the methods of evaluation of IQ in the context of a pinhole SPECT system.

4.4 Pinhole SPECT

4.4.1 Simulations

4.4.1.1 System Modeling

We treat the very simple case of a single-head single-pinhole system which rotates around the phantom. The SPECT scanner is identical to the one described in [118]. The gamma camera is composed of a 64×64 detector with $0.7\,\mathrm{mm} \times 0.7\,\mathrm{mm}$ pixels, with a $2.1\,\mathrm{mm}$ intrinsic resolution, and a tungsten collimator. These are located $60\,\mathrm{mm}$ and

Table 4.3: Error (%) of the Variance obtained from each approximation method at the voxels of interest.

VOI	LSI M1	LSI M2	LSI M3	LSI M4	LSI M5	NUOP	Sub FIM G_1	Sub FIM G_2
P_1	5.35	6.71	11.62	1.41	1.92	0.28	1.01	0.43
P_2	10.91	17.45	29.15	3.44	3.03	0.10	1.12	0.42
P_3	6.05	6.78	10.79	2.03	2.69	0.10	0.22	0.03
P_4	3.00	4.17	6.56	1.30	0.66	0.07	1.22	0.37
P_5	4.74	6.51	13.23	0.54	1.63	0.03	1.36	0.27

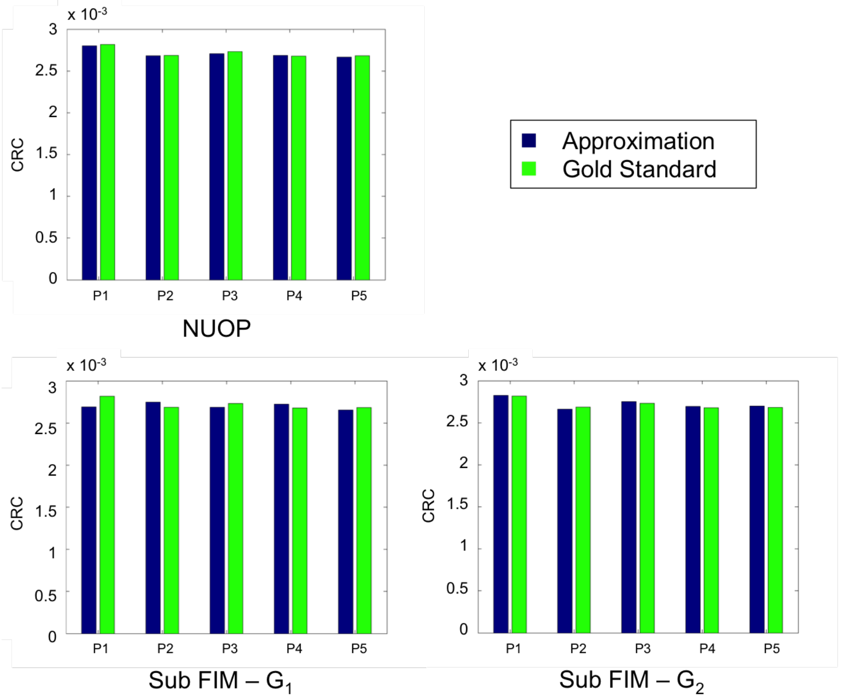

Figure 4.4: CRC values given by the NUOP and subsampled approximation methods (blue) versus the gold standard value (green), where each subfigure corresponds to a different approximation method and each bar in the subfigure corresponds to a different voxel of interest.

15 mm from the center of the image-space, respectively, which results in a 3-fold magnification factor. The pinhole diameter is 0.3 mm, and its opening angle is 90°. The camera rotates around the object for 64 minutes, along a circular orbit. To study the influence of the number of angles, and possible under-sampling, we considered sampling over 32, 64 and 128 equally-spaced projection angles.

The image-space in the reconstruction is divided in $(0.2\,\mathrm{mm})^3$ voxels and has a total dimension of 65^3 voxels.

The forward and backprojections used for the reconstructions were made on-the-fly, using a GPU-implementation of the distance-driven algorithm [65], where a factor was added to account for the pinhole sensitivity. The distance-driven algorithm was chosen because the forward projector is matched with the backprojector (the backprojection is equivalent to applying the transpose of the system matrix), and therefore

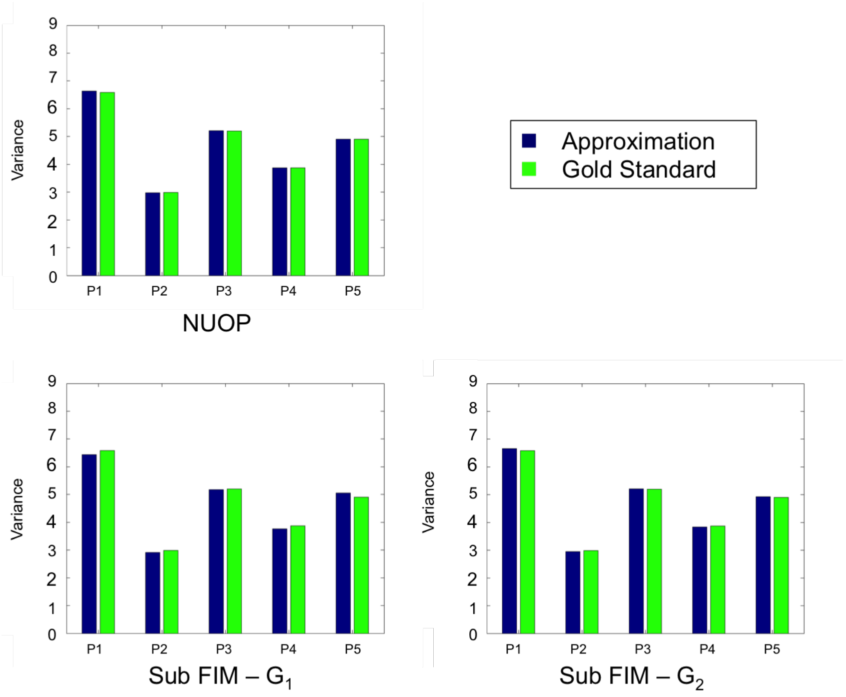

Figure 4.5: Variance values given by the NUOP and subsampled approximation methods (blue) versus the gold standard value (green), where each subfigure corresponds to a different approximation method and each bar in the subfigure corresponds to a different voxel of interest.

we are not making further approximations in our implementation. We did not model the pinhole resolution in the forward and backprojector; for the sensitivity correction, however, the pinhole diameter was taken into account [124, 12]. The same algorithm was also used to compute the full system matrix **H** for the analytical calculations.

4.4.1.2 Phantoms

In this section we describe the three objects which we have considered for imaging, and the corresponding ROIs.

The first object occupies a single slice of 0.2 mm thickness (1 voxel) centered at the pinhole's plane of rotation. It consists of a small disk of 1 mm radius at the center of image-space, within a circular low-activity background of 6 mm radius (Fig. 4.6 (a)). Both regions have a uniform activity distribution and the total activity in the phantom is

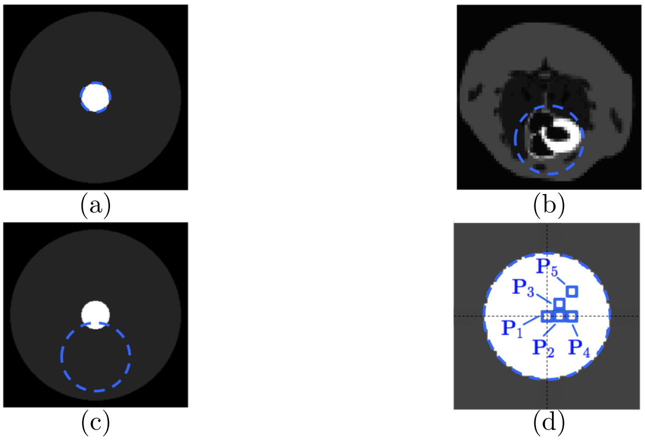

(a) (b)

(c) (d)

Figure 4.6: Phantoms and ROIs (dashed blue lines). (a) The disk phantom. (b) The MOBY phantom. (c) The disk phantom with the second ROI considered. (d) A zoomed-in view of the transaxial slice through the sphere phantom, showing the voxels at which the CRC and variance are computed.

200 kBq, with the background intensity being 1% of the intensity inside the smaller disk. In a first study we consider the ROI to be the disk itself.

The second object is a transverse slice through the MOBY phantom [125], again of 0.2 mm thickness, scaled to fit our image-space (Fig. 4.6 (b)). The total activity in the phantom is also 200 kBq. The ROI is a disk of 2.4 mm radius centered at voxel [34, 18], containing the heart. We also consider this same ROI in the disk phantom (Fig. 4.6 (c)), in order to see how the underlying image can influence the accuracy of the approaches, while keeping everything else equal.

Lastly, we consider an object that occupies the full $3D$ image-volume. It consists of a 1 mm radius sphere at the center of image-space, within a 6 mm radius sphere with an activity density of 1% of that of the small sphere (so Fig. 4.6 (a) also represents a transaxial slice through this phantom). The total activity in the image is 750 kBq. In this case the ROI is the small central sphere, but we only compute the CRC and variance at five voxels of interest P_1 to P_5 (Fig. 4.6 (d)), which are contained within the central transverse plane of the image.

In all the cases considered except one (disk phantom with off-center ROI) the high activity voxels are concentrated within a small neighborhood of the points of interest; this was chosen in order to remove the influence of high activity regions far from the voxels of interest, which have already been shown to decrease the accuracy of the LSI approximation [119]. We also chose points of interest located far enough from the edges of the image, so that the edge effect caused by approximating a Toeplitz matrix by a circulant matrix is not as pronounced.

4.4.1.3 Experiments

4.4.1.3.1 FIM Columns In this section we consider a SPECT system and imaging protocols for which the assumptions of the LSI might not be very accurate. In some cases this is clear from the shape of the FIM columns, so we start by evaluating the images of the FIM columns at the points of interest.

4.4.1.3.2 Figures of Merit for Image Quality In a second phase, we evaluate certain figures of merit (FOMs) for IQ – the CRC, the LIR (off-diagonal impulse responses), the variance and the covariance (off-diagonal correlations) – in the ROI, after convergence of the PF-PML algorithm, both using a gold standard reference method and the different approximation methods described in Section 4.2. The prior chosen is the same as described in Section 4.3.1.2, and the Gaussian filter has a 0.7 mm FWHM.

In the case of the disk and MOBY phantoms, since the problem is reduced to a $2D$ image-space, the CRC and variance values are computed at all the voxels in the ROI considered, whereas for the sphere phantom, due to the increased computational burden, these values are only computed at 5 voxels in the ROI (Fig. 4.6 (d)). The LIR and the covariance are computed between the central point of the ROI and all voxels in the transaxial plane within a 1mm radius of the center.

The gold standard for the LIR for voxel j, l^j, is computed as described in Section 4.3.1.2, using 1000 iterations of the one-step-late reconstruction algorithm. The gold standard for the covariance is based on the reconstruction of 10000 noise realizations of the projection data.

For the analytical methods requiring matrix inversion, instead of computing and storing the inverse matrix $[\mathbf{F} + \beta \mathbf{R}]^{-1}$ we solved a system of linear equations [90]. Compared to performing matrix inversion, solving a linear system is less prone to numerical errors and more efficient for the number of voxels we consider.

The NUOP and subsampled strategies used are as described in Section 4.3.1.2. Furthermore, for the $3D$ sphere we only consider the 9 central transaxial slices of the image.

4.4.1.3.3 Mean errors

We also calculate the root mean squared error (RMSE) of the estimations of each FOM, over the voxels at which they are computed. This gives us a measure of the accuracy of each analytical method (LSI, NUOP and subsampled FIM), relative to the gold standard. We present the RMSE as a percentage of the reference value of the FOM at the central voxel, to see the relative magnitude of the error. Additionally, for the LIR and covariance, before computing the RMSE, we normalize the estimated values so that the value for the central voxel of the ROI is the same as in the gold standard, since for these FOMs we are more interested in the global shape of the estimated values than in quantitative accuracy.

4.4.2 Results

4.4.2.1 FIM Columns

We start our study by investigating the actual shape of the FIM columns corresponding to some voxels of interest. In Fig. 4.7 we note, first of all, that in the images of $\mathbf{F}^j$ there is a concentration of higher valued matrix elements along the scanning directions, which is more pronounced in the 32-angle sampling case. Also along the scanning directions, there is a visible mismatch between $\mathbf{F}_{LSI}(j)^{j'}$ and $\mathbf{F}^{j'}$, but the difference is quite small compared to the peak value of $\mathbf{F}^{j'}$ ($\sim 10\times$ and $\sim 100\times$ lower for the 32- and 128-angle samplings respectively). Note, however, that, for j' corresponding to voxel index $[34, 33]$, we have $\mathbf{F}^{j'} - \mathbf{F}_{LSI}(j)^{j'} \approx 34\%$ at the position corresponding to j', which is considerable, and this happens in both the 32- and the 128-angle samplings. For voxel index $[34, 18]$, on the other hand, the intensity and shape of $\mathbf{F}_{LSI}(j)^{j'}$ and $\mathbf{F}^{j'}$ around the peak are much closer. In fact, the results in the shape of the FIM columns for both phantoms using voxel $[33, 18]$ (Fig. 4.7 (b) and (c)) are very similar, in contrast with the results based on voxel $[33, 33]$ (Fig. 4.7 (a)). This, combined with the observation that the results in Fig. 4.7 (a) are almost identical to those obtained in [126] for the sphere phantom, leads us to conclude that the main factor influencing the shape and local variability of the FIM columns is in fact the position of the point of interest and not so much the phantom itself. We do notice though, by looking at the line profiles, that in Fig. 4.7 (c) the increase in value of $\mathbf{F}^j$ towards the edges, as well as the value of $\mathbf{F}^{j'} - \mathbf{F}_{LSI}(j)^{j'}$ around the

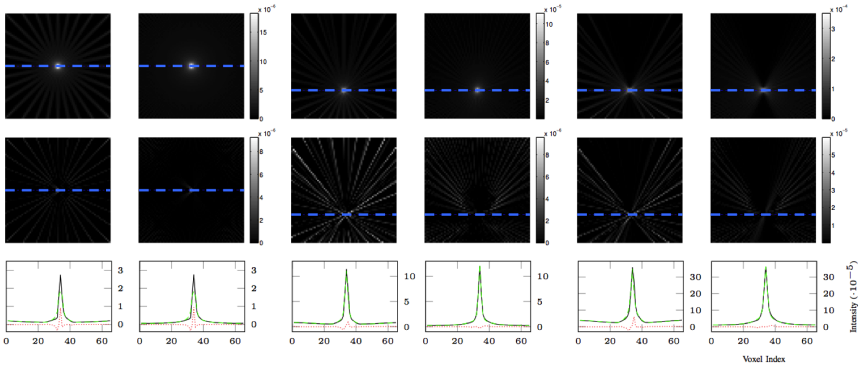

(a) Disk Phantom (b) MOBY Phantom (c) Disk Phantom (ROI at [33, 18])

Figure 4.7: Subfigures (a)-(c) show images corresponding to the jth column of the FIM using the phantoms and ROIs in Fig. 4.6 (a)-(c) respectively. The first column corresponds to the 32-angle sampling and the second to the 128-angle sampling. On the top row is the $2D$ representation of FIM column $\mathbf{F}^j$, where j is the index of the central voxel of the ROI (voxel index $[33, 33]$ or $[33, 18]$); the second row shows the difference between $\mathbf{F}^{j'}$, the FIM column associated with the neighbor voxel j' (voxel index $[34, 33]$ or $[34, 18]$), and $\mathbf{F}_{LSI}(j)^{j'}$, the column obtained by shifting $\mathbf{F}^j$ to voxel j'; on the third row we plot the line profiles through the blue dashed line of $\mathbf{F}^{j'}$ (black), $\mathbf{F}_{LSI}(j)^{j'}$ (dashed green) and $\mathbf{F}^{j'} - \mathbf{F}_{LSI}(j)^{j'}$ (dotted red). The grey scale corresponds to both images in its row.

peak, are more pronounced than in (b).

4.4.2.2 Figures of Merit for Image Quality

In order to visually evaluate the accuracy of the different FIM-approximation methods, in Fig. 4.8 we put side by side images of the FOMs for the gold standard and each FIM approximation method. We only show the results for one phantom because the general behavior and the conclusions we draw are similar for the other phantoms, and we only show the values for the 32-angle sampling protocol because this is where the largest estimation errors occur.

In the CRC images and profiles we can see that LSI - M1, M3 and M4 give somewhat lower values than the gold standard, but the general shape of the estimations is similar (quite uniform). For the LIR and covariance, the NUOP and both subsampled FIM methods show a very good match for all the voxels, and the LSI-based methods are very accurate around the center of the ROI (after normalization); the accuracy

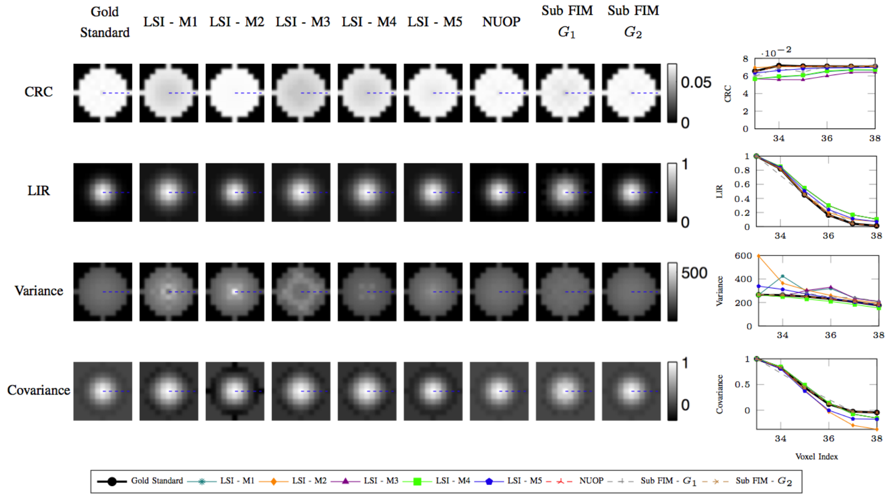

Figure 4.8: Images of each FOM considered for the central ROI in the disk phantom (Fig. 4.6 (a)), for the 32-angle sampling protocol. Each column corresponds to a different FIM calculation method, the first one being the reference method. On the right-hand-side of each row is a line profile through the dashed half-line depicted on each image, with each color corresponding to a different FIM calculation method. The LIR and Covariance estimations have been normalized such that the value at the central point of the ROI becomes 1. Also in these two cases, the subsampled FIM - G_1 estimation is only computed at points within the same grid as the central point, which are then used to obtain the values at the other points by interpolation.

of the LSI methods decreases as the distance from the center increases, but the FOM values also become much smaller. Finally, the variance seems to be the FOM for which the approximation methods perform the worst, in particular some of the LSI methods: on the LSI-based images we can distinguish certain patterns which are not present on the reference method, and which are different for each LSI method; on the line profiles we see quite inaccurate estimations at certain voxels, especially by LSI - M1, M2 and M3.

4.4.2.3 Mean errors

To quantify the accuracy of each FIM-approximation method, in Fig. 4.9 to 4.12 we present their RMSE (in % of gold standard value at the central voxel) for the FOM estimations. In all the figures, and for all the cases considered, we observe that the error given by the NUOP and

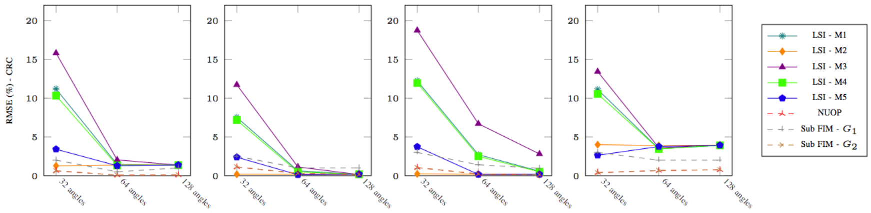

(a) (b) (c) (d)

Sampling	LSI - M1	LSI - M2	LSI - M3	LSI - M4	LSI - M5	NUOP	Sub FIM - G_1	Sub FIM - G_2
32-angles	10.52	1.42	14.94	10.00	3.04	0.80	2.63	0.79
64-angles	2.07	1.41	3.37	1.94	1.33	0.31	1.23	0.31
128-angles	1.50	1.41	2.06	1.49	1.42	0.28	1.24	0.28

(e)

Figure 4.9: RMSE (%) of the CRC obtained from each approximation method against the sampling protocol. Subfigures (a)-(d) show a plot of the error obtained for each phantom and ROI in Fig. 4.6 (a)-(d), respectively, as a function of the angular sampling protocol. Note that the values for the NUOP and Sub - G_2 methods are almost indistinguishable from each other. Subfigure (e) shows a table with the RMSE values averaged over all the phantoms.

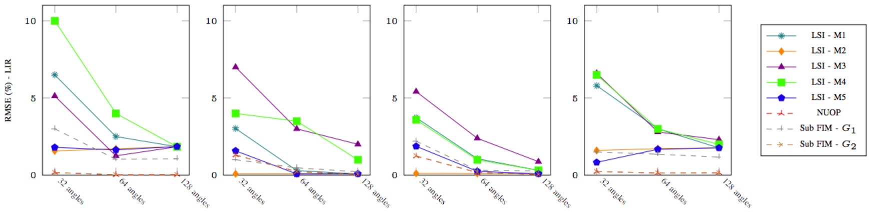

(a) (b) (c) (d)

Sampling	LSI - M1	LSI - M2	LSI - M3	LSI - M4	LSI - M5	NUOP	Sub FIM - G_1	Sub FIM - G_2
32-angle	4.76	0.84	6.04	6.02	1.52	0.73	1.93	0.74
64-angle	1.72	0.90	2.36	2.87	0.91	0.14	0.80	0.14
128-angle	1.00	0.95	1.75	1.29	0.95	0.07	0.68	0.07

(e)

Figure 4.10: RMSE (%) of the (off-diagonal) LIR obtained from each approximation method against the sampling protocol.

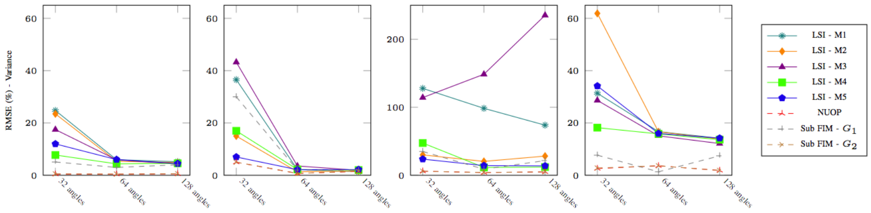

(a) (b) (c) (d)

Sampling	LSI - M1	LSI - M2	LSI - M3	LSI - M4	LSI - M5	NUOP	Sub FIM - G_1	Sub FIM - G_2
32-angle	55.11	32.59	50.91	22.60	19.23	3.50	19.44	3.58
64-angle	30.82	10.93	43.27	8.49	9.59	2.19	3.83	2.20
128-angle	23.61	12.15	63.38	8.08	8.67	2.22	8.75	2.25

(e)

Figure 4.11: RMSE (%) of the variance obtained from each approximation method against the sampling protocol. Note that the y-axis in subfigure (c) is scaled differently than in the others, since the variance values are much higher in this case.

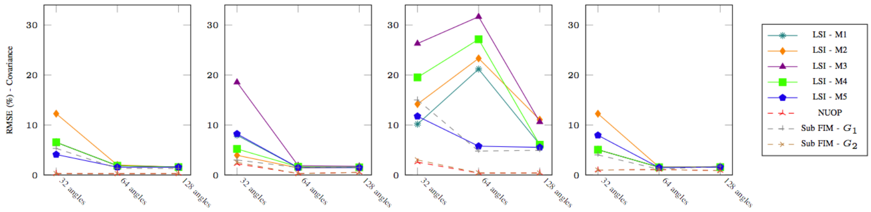

(a) (b) (c) (d)

Sampling	LSI - M1	LSI - M2	LSI - M3	LSI - M4	LSI - M5	NUOP	Sub FIM - G_1	Sub FIM - G_2
32-angle	7.43	10.66	14.11	9.08	8.00	1.52	6.84	1.70
64-angle	6.52	7.08	9.23	8.05	2.58	0.51	2.19	0.52
128-angle	2.72	3.94	3.88	2.68	2.54	0.52	2.38	0.51

(e)

Figure 4.12: RMSE (%) of the (off-diagonal) covariance obtained from each approximation method against the sampling protocol.

Sub FIM - G_2 approaches is nearly identical, and that they are in almost all cases the best performing approaches (their highest RMSE is about 5%, in Fig. 4.11. (b) and (c) - 32 angles), followed by Sub FIM - G_1. It is also noticeable that when using a 32-angle sampling the 5 LSI-based methods give very different error values, but in general these become much more similar and in some cases a lot lower when the sampling is increased. We also observe that, on average (tables), the accuracy of all the methods increases considerably with the increase in sampling, and that the difference between the 32- and 64-angle sampling protocols is larger than that between the 64- and 128-angle sampling protocols, with a few exceptions.

In Fig. 4.9 we see the RMSE obtained for the CRC over the ROI of each phantom. The worst performing method is, for all the phantoms, LSI - M3, followed by LSI - M1 and M4 which are very similar. These methods give an error of 10 to 15% on average for the lower sampling case, whereas the better performing methods give between 0.8 and 3%. When the sampling increases, however, all the methods give a very low error value (up to 2% on average for the 128-angle sampling).

Fig. 4.10 shows the RMSE for the LIR between the central point and the remaining points of the ROI, after normalizing the values of the different estimates to have the same value at the central voxel. The RMSE never goes over 10%, which is quite low. Once again, methods LSI - M1, M3 and M4 seem to give the worst approximations, but their order depends on the phantom. In both the LIR and CRC plots, LSI - M2 outperforms even the alternative methods in phantoms (b) and (c); if we take the average error over the four phantoms, LSI - M2 shows a better agreement with the gold standard than the remaining LSI-based methods, and for the 32-angle sampling it even outperforms Sub FIM - G_1.

The RMSEs for the variance over the ROI, presented in Fig. 4.11, are in general much higher than in the other FOMs evaluated. For phantom (c), LSI - M3 even reaches an error of over 200% and the error values remain quite high with increasing angular sampling. Among the LSI methods there is not one method which consistently performs the best/worst; on average though, LSI - M3 gives the largest errors (50-63%), and LSI - M4 and M5 give the lowest errors (8-23%), which are roughly the same as for Sub FIM - G_1 except in the 64-angle sampling. The NUOP and Sub FIM - G_2 perform consistently better, with an average RMSE of 2-3.5%.

Finally, in Fig. 4.12 we present the RMSE values for the covariance between the central point and the ROI voxels, after normalization. The approximation methods perform generally worse than for the CRC and LIR, but better than for the variance. In phantom (c) the methods perform again particularly poorly, and in 4 of the LSI-based methods the accuracy decreases when the sampling increases to 64-angles. If we look at the average over all phantoms, for the 32-angle sampling the LSI-based methods give errors between 14% (M3) and 7% (M1), which decrease to 2.5-4% for the 128-angle sampling; the error of Sub FIM - G_1 goes from 7 to 2%; and finally for the NUOP and Sub FIM - G_2 it goes from 2 to 0.5%.

4.4.2.4 Efficiency

In terms of efficiency, for the settings described in Section 4.4.1.3, the fastest methods to compute the FOMs based on one voxel were those based on the LSI approximation, where the most computationally expensive step was an FFT of a $65 \times 65 \times 65$ or 65×65 image. For the NUOP and the subsampled FIM approaches, the computation time was of the order of a few minutes for the $3D$ image and less than a minute for the $2D$ images, using a single-threaded implementation on CPU. In any case, all of these approaches are much faster than the reconstruction-based approach, which takes days to perform 10000 reconstructions in our GPU-implementation, even for the 32-angle sampling strategy (a time reduction of $\sim 10^4$).

4.4.3 Discussion

In this section we tested the accuracy of the different approaches of approximation of the FIM described in Section 4.2 on the calculation of several FOMs for the evaluation of IQ in a single-pinhole system. All the approaches analyzed are rooted on the same base expressions, (2.31) and (2.32), so if the assumptions behind the different methods are valid they should lead to the same estimations. In this subsection we will analyze and combine the results shown in Section 4.4.2 in order to derive conclusions for each type of approximation of the FIM, and in the last subsection we give some general recommendations about choosing the right method for a given situation.

4.4.3.1 Local Shift-Invariance Approach

In pinhole SPECT, which is the focus of this subsection, the most extensive validation tests have been done by Vunckx *et al.* in [104]. Following this work, the same approach has been applied to other pinhole SPECT systems, usually by first testing its validity at a few points or for a few cases and then assuming it to hold for the remaining ones [127, 128, 129]. However, the LSI approximation, regardless of the particular method used, is based on two main assumptions which are not explicitly tested in literature (see Section 4.2.1). As such, we first wanted to understand what these assumptions actually entail, and in doing so try to explain the origin of discrepancies between the gold standard and the LSI-based FOM values common to the 5 methods tested. The presence of streaks of higher intensity along the scanning directions in the FIM columns, whose value increases radially outward, within the image-space, stems from the fact that the system sensitivity is higher for elements close to the camera position. This effect could contradict the 1st assumption of the LSI approach, which assumes that column elements far from the point of interest are negligible, and therefore cause the inaccuracy of approximations a), c), and finally d) in Section 4.2.1. This happens regardless of the phantom and point of interest considered, but its intensity seems to diminish when we increase the amount of sampling, so we will refer to this as “sampling-dependent effects” on the FIM columns. This observation is consistent with the fact that in most cases the LSI-based estimation errors considerably decrease with increased sampling. The 2nd assumption of the LSI approximation, on the other hand, says that columns corresponding to neighboring points are identical (up to a shift), and it has a direct impact on the validity of approximations b), c) and d). This assumption seems to be quite accurate in the case of the off-center ROI, especially in the higher sampling scenarios. On the other hand, it seems to be considerably violated for the central points of interest, regardless of the sampling protocol used, so we will refer to this as “voxel-dependent effects” on the FIM columns. These effects should then be mostly responsible for the estimation error that remains in the 64- and 128-angle sampling, and this is corroborated by the fact that in the case of the MOBY phantom, which seems to be the least affected by this issue, the LSI-based FOM estimations for these samplings are usually lower than in the other cases.

Looking now more closely at the FOM estimation images and error plots, we note that the general accuracy of the approximation can also be significantly affected by the phantom itself. For example, in the case of the disk phantom with an off-center ROI, the LSI-based methods show considerably high estimation errors, even for the higher sampling protocols, for all the FOMs with the exception of the LIR, for which there is a relatively low RMSE for all the phantoms. This is especially clear in Fig. 4.11 (c) and 4.12 (c), where most LSI-based approaches show a very different behavior compared to the other phantoms. From the analysis of the FIM columns, there were some indications that this could be the case: the columns showed relatively high values outside of the neighborhood of the voxel of interest, indicating important correlations with these voxels. The reason for this is that most points in the ROI have a very low activity compared to the central high activity region (1%), and so the FOM values will be highly affected by the high activity region which is neglected by the LSI due to its local nature (as in the cases investigated in [119]).

We also observe that, especially when using a lower angular sampling, there can be large discrepancies between the values given by the 5 different LSI approximation methods. This means that the different possible versions of the "3^{rd} main assumption" mentioned in Section 4.2.1, for correcting the eigenvalues, are not equivalent, and therefore not equally valid. In fact, the particular steps proposed in literature are mostly based on the fact that they led to better results (more consistent with reconstruction-based values) for the particular FOM, system settings and image under study, which is not necessarily true in other cases. In the system we consider in this section, it seems that the accuracy of the LSI is highly sensitive to this 3^{rd} assumption, and not just the previous two. Furthermore, it is not clear which LSI approximation method gives the best results: for each phantom, voxel of interest, angular sampling and FOM considered there is a different method which performs best.

Finally, we evaluate the accuracy of the LSI-based methods with respect to each FOM. In the calculation of the CRC, LSI - M2 and M5 show very low error values, and the remaining methods give an error of 10 to 15% for the 32-angle sampling but they become much more accurate with increased sampling. The variance calculations produce the highest discrepancies, with LSI - M3 reaching an RMSE of more than 200% in Fig. 4.11 (c). This difference in behavior of the LSI estimations for the CRC and variance is consistent with the observation which has previously been made in literature [120] that the variance seems to be much more sensitive to issues in the approximation of the FIM than the CRC, when a small β is used, since then $[\mathbf{F} + \beta\mathbf{R}]^{-1}\mathbf{F} \approx I$. As for the off-diagonal LIR estimations, all the methods seem to behave quite well (RMSE under 10%), indicating a good match of the LIR shape once the values have been normalized. The covariance estimations also show a relatively good fit (see Fig. 4.8), but worse than for the LIR, which was to be expected since the estimations of the CRC were better than those of the variance. By looking at the profiles in Fig. 4.8 it is clear that, for the LIR and covariance, as we go further away from the point of interest the LSI approximation becomes less accurate, which makes sense since it is based on the FIM column at the voxel of interest. However, the LIR and covariance for these points come close to 0, so the error is also not very significant. Note that, in Fig. 4.9 (b)-(c) and 4.10 (b)-(c), LSI - M2 shows error values even lower than the NUOP and subsampled FIM - G_2 (it is the only method to do so), but this behavior is not consistent throughout the results. In general, and if we focus on the average FOM estimations, LSI - M5 performs well in all FOM estimations (compared to the remaining LSI methods) and LSI - M3 gives consistently either the worst or in the order of the worst accuracy.

4.4.3.2 Alternative Approaches

We examine the results for the NUOP approach and the subsampled FIM - G_2 together because they gave roughly the same results in terms of accuracy and efficiency, which is due to the fact that the NUOP and subsampling strategies chosen are identical and that the images did not have much variation outside the ROI (see the last paragraph of Section 4.2.3). In all the cases considered, these approaches match the gold standard extremely well, and perform in general much better than any LSI method. The only exceptions are in the estimation of the CRC and LIR, where in some cases LSI - M2 shows a lower RMSE, but even in these cases their error is under 2%. This high accuracy was to be expected, since the NUOP and subsampled approaches do not make such strict assumptions on the shape that the FIM must have as the LSI approach. Even though they are also local approximations, putting more weight on voxels close to the voxel of interest, they take the FIM columns corresponding to a larger number of voxels in the image into account, so their accuracy should in general be at least as good as using an LSI-based approach.

We also used a uniform sampling grid, G_1, with the subsampled FIM approach. This is a grid which has not been adapted to the particular case to be studied, so it can be used for any ROI and even for computing the IQ throughout the entire image. It is natural that using a standard uniform grid G_1 we obtain less accurate results than with a grid which was specifically selected for the task at hand, but we wanted to see if those results are still "good enough". We observe that this approach shows in general a relatively good accuracy, usually better or of the order of the best-performing LSI, but worse than the NUOP and subsampled FIM - G_2.

For all the alternative methods, the higher accuracy in the CRC and LIR estimations compared to the variance and covariance estimations, respectively, can again be explained by the fact that for a small β we have $[\mathbf{F} + \beta\mathbf{R}]^{-1}\mathbf{F} \approx I$. The general increase in accuracy with the finer sampling, on the other hand, and the fact that it stabilizes after a certain amount of sampling (64 angles), is likely due to the fact that the null-space of $\mathbf{F}$ in the lowest sampling case is larger, thereby making the inversion of $[\mathbf{F} + \beta\mathbf{R}]$ more unstable.

4.5 Final Remarks and Guidelines for Method Selection

In this chapter we analyzed the accuracy of FIM-based methods for fast assessment of IQ in two kinds of SPECT systems: parallel-hole and single-pinhole SPECT systems.

Our results indicate several shortcomings of the popular LSI approximation of the FIM, in particular in situations involving low angular sampling. These issues are not always easy to determine, as the exact influence of the LSI assumptions on the accuracy of the FOM estimations is still quite hard to understand. It has already been discussed in literature [119] that it is not appropriate to use the LSI when there are important correlations between the voxel of interest and other voxels outside of its close neighborhood. This is also the reason why the accuracy of the LSI on the LIR and covariance rapidly decreases as we consider elements further away from the voxel of interest. Even when we do not consider these cases, this chapter shows that it is still important to look at the FIM columns for the particular imaging case before using the LSI approach, to look for obvious violations of the assumptions. We have observed that there are sampling-dependent effects on the shape of the FIM, which seem to lead to higher errors in cases with low or uneven angular sampling (e.g. a non-uniform time distribution along the angles). With higher sampling, we do not observe such a strong discrepancy in the computed FOM values, which is probably the reason why in the literature LSI methods have been successfully used to predict variance and CRC in pinhole SPECT: most of the systems used are multi-pinhole systems and/or the scanning protocol uses at least 60 angles (which is the case in the protocol analyzed in Section 4.3 and some of the protocols in Section 4.4). This also explains why the LSI approach has been found to be much more stable in $3D$ PET than SPECT [120], since in PET scanners the angular sampling is a lot denser. Finally, the LSI approach has been applied in a few different ways in literature, which seems to indicate the need to adjust the method to the particular system under study – it is not universally applicable. In this chapter we observed that LSI - M5 [104, 120] was the method that provided the most acceptable error values in general, whereas LSI - M3 [113] seemed to be the least reliable.

We found that even though the observed accuracy of all the methods investigated is sensitive to the phantom, ROI, and FOM considered, the NUOP and subsampled FIM methods gave consistently better results than the LSI for the imaging problem under study. With the grids considered they were slower to compute, but still allowed for a high speed increase compared to the reconstruction-based method, and this speed could also be improved by considering coarser rebinning / subsampling strategies. These methods have not been as extensively tested as the LSI yet, but our investigation indicates that they could be more robust when it comes to changes in the system or protocol. This robustness can be quite important in system design and especially in adaptive SPECT. Additionally, they allow the user to regulate the trade-off between accuracy and computational speed by considering a larger or smaller FIM, which is not possible with the LSI methods unless the voxel size is changed.

For the cases not examined in this chapter, we expect that the NUOP and subsampled approaches will, on average, provide more accurate estimates of the FOMs for IQ than an LSI-based method, especially using a strategy which has been adapted to the task, and in particular for the calculation of the variance. This is because they do not impose such restrictive requirements on the FIM in order to work, and they take the values of the FIM at more voxels into account. Unlike the LSI, we also have control over their accuracy: if we keep the sampling high enough in the high-variability regions in the image, we make sure that the fundamental conditions for the NUOP and subsampled approach to be valid are being met, and we can then gradually remove this condition until we get the required computation speed. If a similar rebinning / subsampling strategy is chosen for both methods, the main difference between the two alternative approaches is that the NUOP takes all values into account (but averages them out), whereas the subsampled approach skips some of them, so in the presence of high-variability regions with sparse sampling the NUOP is likely to give the most accurate results. If we are interested in observing a small ROI and we do not expect the activity far from this region to have a significant effect on its IQ, then it should be best to define a fine pixelation / subsampling around this region and let it become coarser as we go further away, as we have done for the NUOP approach and the subsampling grid G_2. On the other hand, in situations, such as described in [119], in which there are important correlations with voxels far from the ROI, it might be best to define a uniform pixelation / subsampling distribution over the image-space, such as in subsampling grid G_1. This kind of grid would also be useful to evaluate the global IQ [119], and not just in a small ROI, in a more efficient manner than using the LSI approach, which involves recomputing the λ_k^F for each voxel j considered in the image. As a more general approach, Meng *et al* have proposed strategies for choosing the most appropriate rebinning scheme, which take the “relative importance” of each voxel for the IQ at the ROI into account, by using the FIM [117].

Nevertheless, whichever strategy is chosen, the influence of the FIM approximation on the evaluation of IQ is complex and we cannot give an error bound for a given method, or even predict with certainty which of them will provide the best results. As has been stressed throughout this chapter, each method is based on specific assumptions, and the accuracy of these assumptions depends on the specific imaging problem and how the method is chosen (the rebinning / subsampling strategy, the eigenvalue correction...). With the examples shown here we see how crucial it is that we understand the assumptions being made before applying a given method, and how this can affect the accuracy of the results. Furthermore, we should not forget that all these methods are based on the same expressions (2.31) and (2.32) [57, 90], which involve additional approximations. Therefore, in order to have a reasonable assurance that the error in estimating the IQ will be lower than a certain threshold we have to compare it with gold standard values, at least for a few settings.

4.6 Summary and Original Contributions

Inspired by recent results indicating that the LSI implicitly assumes things about the nature of the FIM which are not always valid [119], in this chapter we investigated the accuracy of the FIM-based calculation of FOMs for IQ using the LSI approximation in standard parallel-hole and pinhole SPECT systems and protocols. We also wanted to see if alternatives suggested in literature, the NUOP and subsampled FIM, could perform better.

We show that it is not very hard to break the conditions of validity of the LSI approach, and we should therefore be very careful when applying the LSI approximation. In order to trust the results of the approximation, one should present a proper justification as to why that particular application method of the LSI may be used in that particular situation.

Finally, we found that, in this particular case, the NUOP and subsampled FIM approaches result in estimations which are in general much closer to the gold standard values than the LSI, and so they seem to be much better suited for this application if a good accuracy is required. Due to the fact that they do not require such restrictive assumptions as the LSI, we also believe that these methods are likely to be more reliable in general, at least for pinhole SPECT, for comparing different systems and protocols. We do stress that our study is not all-encompassing, and whichever the approximation method chosen it should be used carefully.

The first system investigated, using parallel-hole collimation, was of particular interest because in Chapter 6 it is compared to a cylindrical parallel-hole system developed in Chapter 5 of this dissertation. From the results in this chapter we picked the subsampled FIM method with grid G_2 to perform the comparison of the IQ of the two systems, in terms of the FOMs validated here.

The portion of this chapter on pinhole SPECT has resulted in a peer-reviewed A1 journal publication [130], and a conference proceeding [126]. Parts of this work have also been used in the context of Adaptive SPECT and submitted for a book chapter [131] (to be published), as well as published in a conference proceeding [132] and a conference abstract [133]; however, this line of investigation did not prove fruitful.

Chapter 5

Parallel-hole Collimator Concept for Stationary SPECT Imaging

In this chapter we develop a new concept for a SPECT collimator that avoids rotation of the gamma-camera. Chapters 6 and 7 will build on the results of this chapter. The proposed collimator concept is first introduced in Section 5.2.1. Then, in Section 5.2.2, three possible designs are described, that correspond to a human full-body, a human brain and a small-animal full-body imaging system. These three systems are simulated using the method developed in Chapter 3 for modeling complex collimator geometries. Finally, we describe the simulations performed in Section 5.2.3 and show the obtained results in Section 5.3.

5.1 Introduction

As described in Chapter 2, the collimator is a fundamental part of any SPECT system. It is positioned in front of the radiation detector, to determine the direction of incidence of gamma-photons on the detector. Up until recently, the available collimator production techniques have greatly limited the different types of collimators possible to manufacture. Parallel-hole and fanbeam collimators have traditionally been produced by stacking sheets of folded lead foil to make hexagonally-shaped aperture holes. Pinhole and multi-pinhole collimators, on the other hand, usually involve the introduction of pinholes into a solid plate of heavy metal or alloy, by drilling or other traditional machining methods. Another important collimator fabrication technique is casting, or molding, which can be used to produce a larger variety of collimator geometries, but it is still limited to designs for which a mold can be removed from the collimator. Fortunately, the advent of metal additive manufacturing has opened the doors to a much wider freedom in collimator design [33, 34]. Two important examples of this are the lofthole collimator [37], a variation on the traditional pinhole collimator that allows a higher detector coverage without multiplexing, and the artificial compound-eye (ACE) gamma camera [134], with closely packed micro-pinhole apertures for high sensitivity, dense angular sampling, and compact SPECT imaging.

In this context, we now propose a new type of collimator geometry for stationary SPECT imaging (i.e. fixed detector and collimator), based on parallel-hole collimation. A stationary system does not require large and expensive rotation mechanisms, it has simple mechanics (table translation) and is easy to calibrate, avoiding rotation-related degradation of image quality and system idle time due to its mechanical motion. Current stationary SPECT systems are based on multi-pinhole collimators. A few systems have been proposed for clinical imaging of organs such as the brain [24] and the heart [19], but with very low angular sampling. In small-animal imaging, systems such as the FASTSPECT [14, 15] and the U-SPECT [16, 17] have their pinholes focused towards the center of the system, making the field of view with enough angular sampling for artifact-free reconstruction quite small compared to the collimator bore, and much smaller than the full size of the system. In the case of the U-SPECT, the scanning protocol involves moving the animal both axially and transaxially for full-body imaging.

The novel collimator described in this chapter, on the other hand, uses parallel-hole apertures to obtain full angular sampling of objects coming quite close to the collimator bore using only axial bed translations, thereby making it more compact and light than current stationary SPECT systems. These characteristics make the proposed type of collimator especially suited for applications with spatial restrictions, such as SPECT-MR inserts. The system can also be used in continuous bed motion acquisition mode, analogous to other medical imaging modalities such as spiral CT and the Siemens FlowMotion in PET [135].

Here we investigate the feasibility of using the proposed geometry for three frequent SPECT scanning applications: human full-body, human brain and small-animal full-body imaging.

5.2 Methods

5.2.1 The Concept

The novel collimator geometry for stationary SPECT imaging we propose is inspired by cylindrical parallel-hole collimator design of the CERASPECT system [136], a rotating brain-SPECT scanner. The proposed system consists of a collimator body of heavy metal surrounding the field-of-view (FOV), which is surrounded by a ring of gamma-ray detectors. The parallel collimator apertures within each transaxial slice, or set of slices, only accept radiation coming from e.g. 3 different angles. The orientation of the apertures in subsequent slices, or sets of slices, changes incrementally by rotating the slice(s) over a fixed angle. As a result, an axial translation of the object through the proposed collimator is equivalent, in terms of angular sampling, to the rotation of a traditional collimator while keeping the object fixed (see Fig. 5.1).

In Fig. 5.1 we show a possible design for such a collimator, the design which we explore in this chapter, and how the different directions are sampled during the imaging scan. The outer shape of the collimator is determined by the desired detector geometry, which is in this case

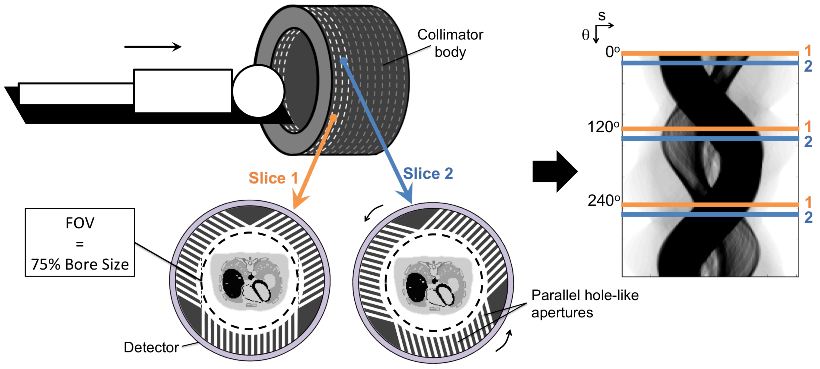

Figure 5.1: Schematic representation of a collimator design (not to scale) using the proposed concept. It shows the collimator body, sections through the system at two transaxial slices and the sinogram of a section of the object being imaged, obtained by translation through the system, with the lines corresponding to the two slices indicated. This system gives three sampling directions per slice and allows reconstruction of 75% of the transaxial area of the bore, and is approximately equivalent, in terms of the resulting sinogram, to a rotating parallel-hole SPECT system.

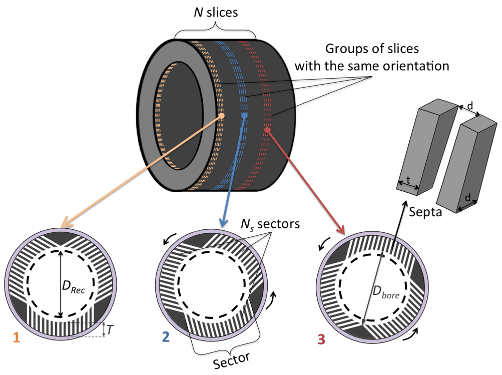

Figure 5.2: Schematic representation of the type of SPECT system simulated in this chapter (not to scale), with some of the symbols and designations used.

cylindrical. The collimator body (see Fig. 5.2) can be divided into N imaginary transaxial slices, each containing N_s sectors of parallel holes (at least 2), where one sector of holes defines one sampling angle. In our design we consider several consecutive slices with the same orientation (schematically shown in different colors in Fig. 5.2), which we shall call a "group of slices", and from one group to the next the collimation directions are rotated by a constant angular increment around the center of the system, such that if we take all the slices together a range of $360°$ is spanned.

5.2.2 Simulated Systems

In this chapter we simulate three systems of the type described in Section 5.2.1, for different imaging scales: full-body, brain and small-animal imaging. As shown in Fig. 5.1 and 5.2, the collimators have a cylindrical shape and each transaxial slice has three sectors of parallel holes, which gives us a useful FOV of $\sim 75\%$ of the total transaxial area inside the collimator bore. The simulated collimator material is lead, and each aperture hole can be obtained by removing a square prism from the main body (Fig. 5.2). The simulated detectors are continuous NaI 3/8" crystals, of cylindrical shape, with an inner diameter and height equal to the outer shape of the collimator.

The parameters of the three different systems are listed in Table 5.1, and some of these are represented in Fig. 5.2. The penetration and resolution are computed using the formulas described in Section 2.2.2. For the full-body system, we chose the system parameters to be similar

Table 5.1: The parameters of the full-body, brain and small-animal systems simulated in this work.

System	Full-body	Brain	Small-animal
Reconstruction diameter D_{Rec} (cm)	54.20	26.74	5.42
Collimator bore diameter D_{bore} (cm)	62.58	30.88	6.25
Collimator thickness T (cm)	4.00	1.98	0.40
Hole width d (mm)	1.42	0.68	0.1
Septal thickness t (mm)	0.12	0.08	0.054
Maximum penetration for 140 keV (%)	1.5	5.9	5.0
Detector resolution (mm)	3	1.5	0.3
Target resolution at the center of the FOV (mm)	13.1	6.39	1.05
Number of sectors per slice N_s	3	3	3
Number of holes per sector N_h	352	352	352
Number of slices N (# groups × # slices per group)	40×8	40×2	40×8
Angular increment between subsets	3°	3°	3°
System axial length L (cm)	49.28	6.08	4.93

to a modern commercial full-body SPECT system: the GE Discovery NM/CT 670, with its low energy/high resolution parallel-hole collimator. In particular, the transaxial reconstruction FOV and the target resolution at the center of the image space are very similar in both systems. The brain and small-animal systems were scaled down such that the diameter of the reconstruction FOV would be about 50% larger than the minimum required to image the Hoffman phantom (18 cm) and the MOBY phantom (3.5 cm), respectively, to account for subject size variability. For the brain system, this resulted in a scaling factor of roughly 2, and for the small-animal system a factor of 10. However, the ratio between the septal thickness t and the hole width d needed to be increased to keep the septal penetration for 140 keV photons (^{99m}Tc) under 6%.

The standard sampling for rotating parallel-hole systems is 120 uniformly spaced angles over 360°. In our systems this would correspond to having 40 groups of slices rotated by 3° from each other, since they comprise 3 sectors of parallel-holes per collimator slice. This should allow us to achieve a sufficient angular sampling of the radiation source by stepping it through the collimator with an incremental translation equal to the thickness of a group of identical collimator slices. In the full-body and small-animal systems we chose to have 8 slices per group (oriented in the same direction), in order to reduce the number of steps of the scanning protocol; in the brain system, however, we only have 2 slices per group, in order to allow the entire brain to go through the scanner, since the shoulders would not fit inside the collimator bore.

5.2.3 Simulations

In this section we describe the different experiments which we do to investigate the performance of the proposed stationary SPECT systems. In all the experiments the entire cylindrical detector is divided into 1440×320 pixels ($\mathsf{transaxial} \times \mathsf{axial}$ dimensions), and the transaxial image-space ($D_{Rec} \times D_{Rec}$ from Table 5.1) into 176×176 voxels. For the reconstructions and to compute the sensitivity map, we use a system matrix (specific to each of the three systems) obtained using the method described in Chapter 3, Section 3.3. This method has been validated in Section 3.3 using Monte Carlo simulations. The reconstructions are performed using MLEM, without post-smoothing. The characteristics of the three simulated systems can be found in Table 5.1, and the corresponding $(\mathsf{voxel}, \mathsf{pixel})$ pitches were $(3.08, 1.54)\,\mathsf{mm}$, $(1.52, 0.76)\,\mathsf{mm}$ and $(0.308, 0.154)\,\mathsf{mm}$ for the human full-body, human brain and small-animal SPECT systems, respectively.

5.2.3.1 Sensitivity, Resolution and Noiseless Reconstructions

The analytical model is then used in Section 5.3.1 to predict the system performance and to generate noiseless reconstructions. The system sensitivity is computed for each voxel in the reconstruction FOV, for one bed position, as well as its mean value over the FOV. Then, noiseless reconstructions of the following objects are shown after 200 MLEM iterations: a) a hot-rod Derenzo phantom, where each sector contains cylinders of a height of 80 voxels and a range of different diameters (shown in Fig. 5.4 (a)); b) a cylindrical uniform phantom, of a height of 60 voxels and diameter close to D_{Rec}. In both phantoms, the activity regions have a voxel value of 1. The phantoms' axis is oriented along the axial scanner direction, and in the scanning protocol each step corresponds to the thickness of a group of transaxial slices of the collimator. These noiseless reconstructions allow us to check for artifacts, and the Derenzo phantom allows us to estimate the actual resolution after reconstruction for our system.

5.2.3.2 Noisy Reconstructions

Finally, in Section 5.3.2 we perform reconstructions from noisy projection data corresponding to realistic phantoms and protocols based on realistic values of scanning time and total injected activity, to test the performance of the systems in more practical scenarios. The reconstructed images shown correspond to 50 iterations of MLEM.

For the full-body system, the phantom used is the male XCAT phantom [137], with organ activity uptake values for ^{99m}Tc-HMDP (bone imaging) obtained from [138]. The total activity simulated is 740 MBq and the total scanning time is 30 *min*, corresponding to a realistic clinical procedure for bone imaging. The scanning is done by regular bed-shifts of 12.32 mm, corresponding to one subset of 8 collimator slices, giving a total of 180 bed positions for the full-body scan.

For the brain system, we use a Hoffman phantom with a total activity of 50 MBq of ^{99m}Tc-ECD, assuming a gray-to-white-matter ratio of 4:1 and a 5% brain uptake of a total injected activity of 1 GBq [121]. For a realistic clinical protocol, we consider the total scanning time to be 30 *min*. The total number of bed positions used is 139, and each bed-shift is 1.52 mm.

For the small-animal system, we consider the MOBY phantom [125, 137], and simulate an injection of 134 MBq of ^{99m}Tc-tetrofosmin for a 45 *min* scan, as proposed in [139] for myocardial perfusion scanning of mice (here we use the same scanning time for full-body imaging). The relative organ activity distribution is based on [139]. The scanning procedure is composed of 128 bed positions with 1.232 mm shifts.

5.3 Results

5.3.1 Sensitivity, Resolution and Noiseless Reconstructions

The analytically determined (collimator) sensitivity of the human full-body system to each voxel in the reconstruction FOV (a cylinder of 49.3 cm length and 54.2 cm diameter), is shown in Fig. 5.3 (for one bed position). For the other systems, a very similar sensitivity map is obtained, but with different sensitivity values per voxel. We can see that the central region of the transaxial FOV has a higher sensitivity than the edges. The mean voxel sensitivity throughout the entire reconstruction FOV (one bed position) is 166 cps/MBq, 148 cps/MBq

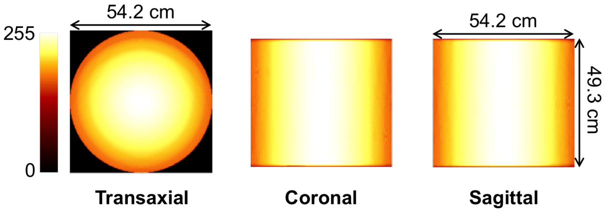

Figure 5.3: Sensitivity map for the human full-body system. For each voxel, the intensity in the image represents the geometric sensitivity of the system to that voxel. The values of the color scale are given in cps/MBq.

and 40 cps/MBq for the full-body, brain and small-animal systems respectively, and the maximum sensitivities achieved are 255 cps/MBq, 226 cps/MBq and 62 cps/MBq.

Next we present the results from noiseless reconstructions. First we show the reconstruction of a hot rod Derenzo phantom, in Fig. 5.4, for each of the three simulated systems. We see that at the center of the FOV the resolution after reconstruction is about 11 mm, 5.5 mm and 0.9 mm for the full-body, brain and small-animal systems respectively.

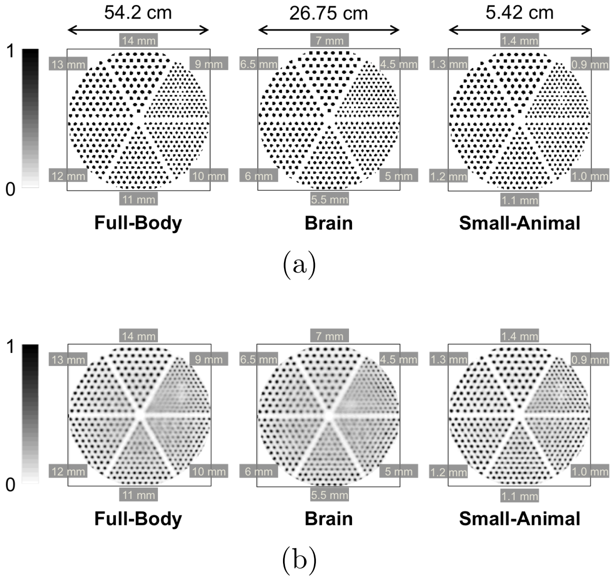

(a)

(b)

Figure 5.4: Transaxial view of the hot-rod Derenzo phantom (a) and its noiseless MLEM reconstruction (b), for the three systems considered.

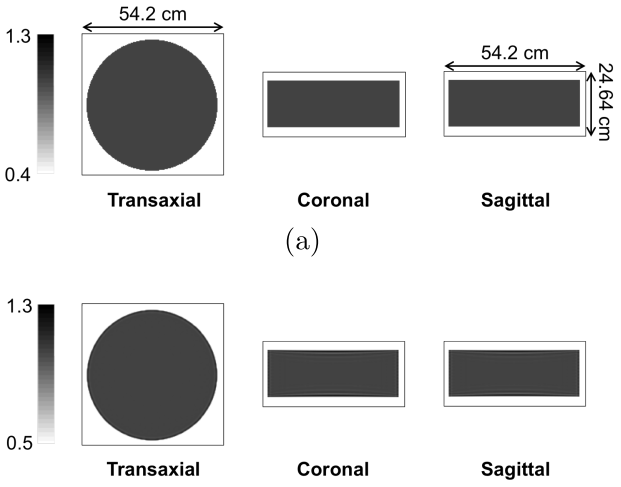

(a)

(b)

Figure 5.5: The uniform cylindrical phantom (a) and its noiseless MLEM reconstruction (b).

Towards the edges of the FOV there is an improvement in resolution. In Fig. 5.5, the reconstruction of a uniform cylindrical phantom using the human full-body system is shown. The image shows good uniformity and therefore indicates that with this system and sampling protocol we have enough angular sampling throughout the desired FOV. The reconstruction of a uniform phantom using the other two systems gave similar results.

5.3.2 Noisy Reconstructions

In this section we show the reconstruction results obtained for the three simulated systems (Section 5.2.2) and corresponding phantoms and protocols (Section 5.2.3.2).

In Fig. 5.6 the original XCAT phantom and the reconstructed image obtained with our full-body SPECT system can be seen. The sections show, in each direction, the average intensity projection over 176 image slices, for a better visualization of the bone structure. We can see that the reconstructed image matches the ground truth very closely.

In Fig. 5.7 and 5.8 we show a transverse, coronal and sagittal section through the Hoffman and MOBY phantoms, respectively, and corresponding reconstructions. In these cases the main structures seen in

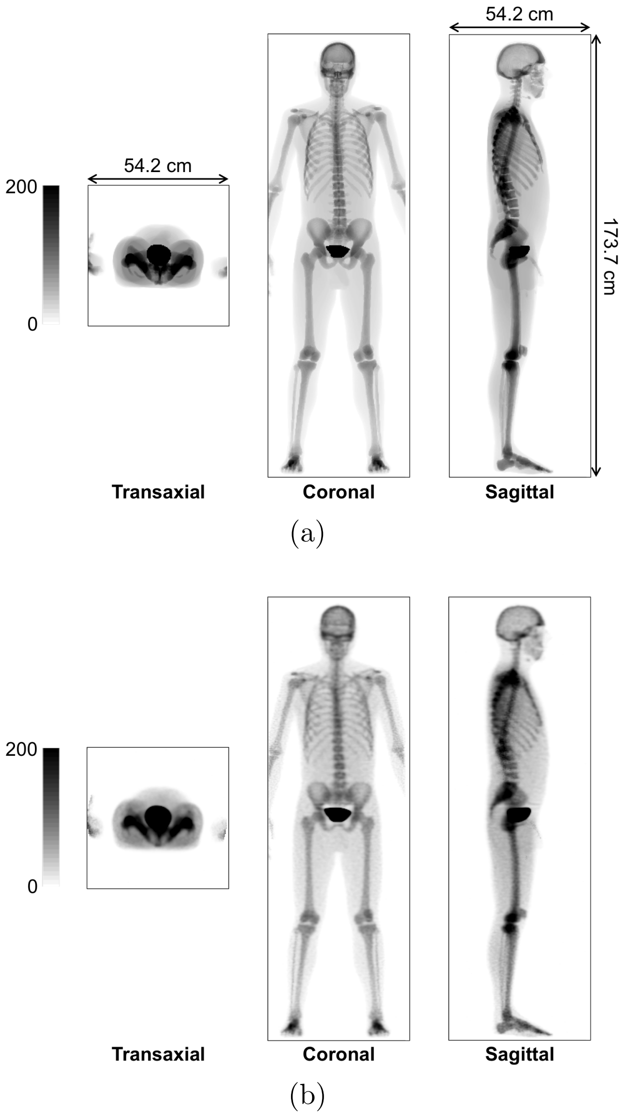
54.2 cm
54.2 cm
200
0
173.7 cm
Transaxial
Coronal
Sagittal
(a)
200
0
Transaxial
Coronal
Sagittal
(b)

Figure 5.6: The XCAT phantom (a) and its MLEM reconstruction from noisy projections (b). The values of the grey scale are given in Bq.

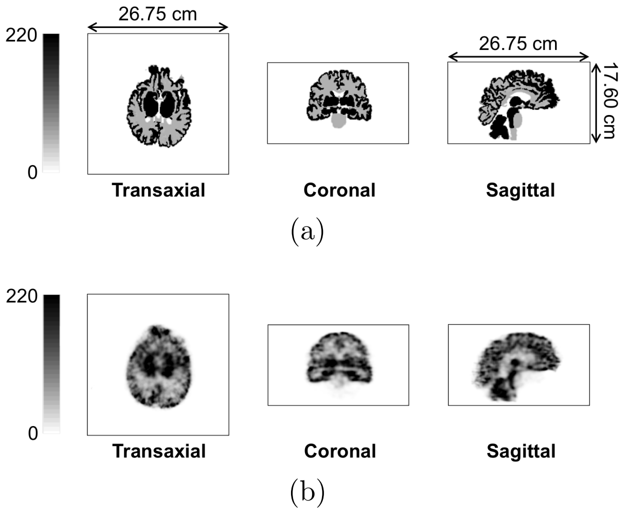

Figure 5.7: The Hoffman phantom (a) and its MLEM reconstruction from noisy projections (b). The values of the grey scale are given in Bq.

the original image can also be seen in the reconstructions, but there are more visible differences between the two images than before. In particular, comparing Fig. 5.6 and 5.8 we see that the latter looks much more noisy.

Sampling artifacts were seen in none of three cases.

5.4 Discussion

In this chapter we have proposed a new type of collimator for stationary SPECT imaging (Section 5.2.1), based on parallel-hole collimation instead of pinholes, that allows a large FOV to be reconstructed using only translation of the bed along the longitudinal scanner axis. We tested, using simulations, particular designs for three different purposes: full-body, brain and small-animal imaging.

We first evaluated the behavior of the system sensitivity and resolution throughout the reconstruction FOV, for the three different systems. We observed that the sensitivity is higher at the center of the FOV, which is explained by the fact that this part is always “seen” by the central part of the collimator sectors, and there the aperture holes are much shorter than the ones at the edges of the sector. The fact that the resolution improves as we go towards the edge of image-space is consistent with

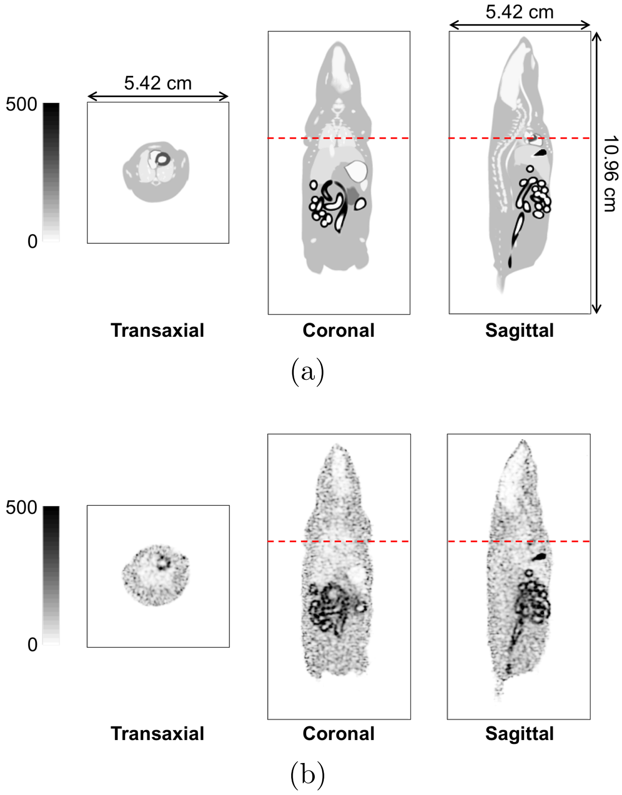

Figure 5.8: The MOBY phantom (a) and its MLEM reconstruction from noisy projections (b). The transaxial slice is taken through the dashed red lines. The values of the grey scale are given in Bq.

the previous observation that the sensitivity decreases, and can be explained by the fact that longer aperture holes result in lower sensitivity but have an improved resolution. In order to counteract this effect but keep the same global geometry, one could think of a design where the aperture hole width becomes larger as its length increases, such that the sensitivity and resolution are more uniform throughout the FOV. The resolutions obtained after reconstruction are slightly better than the predicted target resolution (shown in Table 5.1 and obtained using analytical formulas), which was to be expected. Note that in the simulations the collimator penetration was not modeled, so we would expect the real system to result in slightly worse resolution and higher sensitivity values, especially for the central points in the brain and small-animal systems, for which the penetration is the highest.

We also performed a noiseless reconstruction of a uniform phantom, and observed that the system is indeed able to reconstruct objects with a diameter of about 75% of the transaxial area of the bore (as we expected given the collimator geometry) without sampling artifacts, using only axial bed shifts.

Finally, we tested the feasibility of using the three systems in more practical settings. We performed reconstructions from noisy data based on realistic activity levels and scanning times, and the systems themselves were also designed for realistic target image resolutions, similar to what is used in clinical/preclinical practice, for a fair assessment of the systems. The full-body human system shows particularly good results under realistic scanning conditions. However, we should be careful because in these simulations we did not consider the effect of scatter or attenuation within the phantoms, and for a truly realistic assessment of the system performance this should be considered, especially in the human full-body scan. The other systems do not show as good of a reconstruction for the corresponding protocols, and the main reason for this is because when scaling down the systems we needed to increase the size of the septal thickness relative to the hole width to limit the septal penetration, which results in less sensitivity for an equivalent resolution. This is corroborated by the sensitivity values observed in Section 5.3.1, where the small-animal system shows a mean voxel sensitivity 4× lower than the full-body system. In fact, the mean geometric sensitivity obtained in the small-animal system (40 cps/MBq) is quite low compared to state of the art SPECT systems for a similar image resolution, which also have a smaller FOV. However, it was not the aim of this chapter to develop the best system design for each specific imaging application but rather to show that imaging is possible with this kind of system.

From these results, it seems viable to use the proposed collimator concept in practice, even though our simulations are somewhat simplified. In the next chapters we will continue to explore these types of SPECT systems and compare their performance with standard systems. We would also like to point out that although we only considered collimator designs using parallel collimator holes, this is not the only option. We can use other kinds of collimation with this same principle of having different transaxial slices of the collimator correspond to apertures oriented along different directions, which achieve full sampling by longitudinal bed translations. For example, to use the detectors optimally, it could be better to use fanbeam or conebeam collimation. The shape of the collimator and the apertures, as well as their configuration, can be adapted to the user's needs: it is only limited by the detector geometry, as long as full angular sampling of any part of the object can be achieved through bed-translations along the longitudinal scanner axis alone. Another design option would be, instead of (or in addition to) having groups of consecutive transaxial collimator slices with the same orientation, to separate the collimator along the axial direction in e.g. 2 parts, each of those parts having slices spanning $360°$ with sufficient sampling. In this case the scanning protocol can start with the imaging object half-way through the scanner instead of at the beginning, resulting in an improved sensitivity of the system to the object during the scan.

This new SPECT collimator concept has some limitations, compared to other types of systems. In particular, the fact that there is a fixed collimator bore which should be large enough to accommodate most patient sizes means that we are not able to have the collimator as close to the patient as in conventional rotating SPECT systems, which would result in a better sensitivity-resolution trade-off. This is most problematic for human full-body imaging, where the range of body sizes is rather large. To improve this we could consider making the system oval shaped, instead of circular. Another limitation is that, since it is based on parallel-hole collimation, it is not as suited for imaging smaller regions of interest as (multi-)pinhole collimation (in terms of sensitivity-resolution trade-off).

Based on these observations, human brain imaging could be the most promising application for the technology. However, it also presents particular advantages that can be useful in many clinical and preclinical applications. Firstly, one of the most likely uses of such a system would be in SPECT-MR scanners, due to its very efficient use of space. Secondly, it allows for very compact clinical and preclinical systems, therefore saving both space and material costs. Thirdly, this new type of collimator could be placed in already existing SPECT scanners to replace other collimators, since it only requires longitudinal movement of the patient bed, thereby making it practical to use and possibly more cost-effective (the system developed in Chapter 7 is an example of this). Lastly, it could allow us to build the first full-body human stationary SPECT scanner.

5.5 Summary and Original Contributions

In this chapter we have presented a new type of collimator and corresponding acquisition method for stationary SPECT imaging. The collimator is based on parallel-holes with a varying angular alignment, arranged in transaxial slices, and the acquisition method consists of step-wise longitudinal bed translation.

We developed three different systems, for specific clinical and preclinical applications, and then performed simulations to investigate their behavior and performance in realistic scanning protocols. From the results we conclude that the system could be used for stationary SPECT imaging in practice, and we discuss possible applications and advantages of the system.

These findings are quite promising, and show that we could indeed use parallel-hole collimation for very compact stationary imaging. In chapters 6 and 7, two concrete applications for this type of system are further explored: human brain imaging and small-animal imaging.

The work described in this chapter has been published in a peer-reviewed A1 journal [110]. There is also a patent application [140] for the collimator concept presented.

Chapter 6

Comparison Study: New Stationary System vs Rotating System in Clinical Brain Imaging

In this chapter we compare the performance of a stationary SPECT system based on the concept proposed in Chapter 5 with a standard triple-head system for clinical brain imaging, based on simulated reconstructions and the measures of image quality described in Chapter 4. The methodology for the simulations is described in Section 6.2, and the results and implications are discussed in Section 6.3.

6.1 Introduction

In order to reconstruct a 3D image of the radioisotope distribution in the object being imaged using a SPECT system, it is necessary for each point in the distribution to be "seen" by the system from a sufficient number of different angles; this condition is referred to as sampling completeness. Sampling completeness is usually achieved by rotating the collimator/detector-pair(s) (the gamma-camera(s)) around the patient. To avoid rotation of at least one of the components of the gamma-camera (detector or collimator), alternative SPECT systems have been proposed. One option is to keep the detectors stationary and move only the collimators, which can be done for example by using slant-hole collimators [141, 142] or by a rotating annular/cylindrical collimator such as in the brain-dedicated system CERASPECT from DSI [136, 143]. Another idea is to have stationary collimators and perform synthetic collimation, which requires either a radial motion of the detectors or multiple detectors behind each other (stacked-detector acquisition) [144, 145, 106]. Finally, many systems have been proposed, the so-called stationary SPECT systems, which have fixed detectors and collimator(s) surrounding the field of view: the FASTSPECT, the U-SPECT, etc. [24, 14, 15, 16, 17, 19, 18].

SPECT systems which require some form of movement of heavy components of the SPECT scanner have several drawbacks. In order to have an acceptable image quality we need a high precision positioning of the gamma-cameras, which requires rather large and expensive rotation mechanisms. Furthermore, this positioning is never perfect, which leads to a degradation of the final image obtained due to the incorrect calibration of the SPECT system after rotation. Also for the same reason, a rotating SPECT scanner needs to be frequently re-calibrated by a qualified expert, which brings additional costs. As such, it is generally preferable to use stationary systems.

In Chapter 5 we introduced a novel collimator concept for fully-stationary SPECT imaging, with a design that allows us to reconstruct a transaxial field-of-view which comes close to the collimator bore, using only bed translations along the longitudinal scanner axis. As mentioned in Section 5.4, such a system would be particularly suited for human brain imaging, due to the relatively small variation in head sizes and the fact that we are usually interested in imaging a considerably large field of view (the entire brain). In this chapter we use the same collimator concept to develop a system with similar settings (hole diameters, sizes, etc.) as a standard clinical SPECT system, and we perform a comparative analysis of the performance of the two systems for brain imaging. The comparison is done with simulations and analytical methods that assume that both systems are perfect (and not taking the practical issues associated with a rotating gamma camera into account).

6.2 Simulations

6.2.1 The Systems

We simulate two systems: a standard rotating parallel-hole SPECT and a stationary parallel-hole SPECT. For a fair comparison, we designed the stationary system to have similar properties (in terms of resolution, sensitivity and FOV) to the rotating system.

The rotating system is based on the Triple Head Human SPECT system Prism 3000 NewTec (Inter Medical), and its settings are described in Section 4.3. The stationary system has a cylindrical shaped collimator and detector, and 3 hole sectors N_s per slice, as in Fig. 5.1. Both collimators are made of lead, with square prisms as aperture holes. The hole width and the septal thickness are the same in both cases ($d = 1.3\,\mathsf{mm}$ and $t = 0.18\,\mathsf{mm}$). The thickness of the stationary collimator is $T = 23.7\,\mathsf{mm}$. The mean aperture height (averaged over the whole collimator) is approximately equal to the height of the (uniform) parallel-holes in the rotating system (27 mm). In both cases, the collimator is placed at a distance of 12.5 cm from the center of the image-space, and the reconstruction FOV is a cylinder of 10.8 cm radius (values based on [136, 143]).

The stationary system has $N_h = 146$ holes in each of its 3 sectors, arranged in 40 slices rotated by 3° from each other (a total of 120 angles). In order to have a faster scan, we repeat this set of 40 slices 4 times, for a total axial length of 160 slices, or 23.68 cm (note that this is a different strategy than the one adopted in Chapter 5 of grouping slices with the same rotation angle together). This also means that we use the system more efficiently, because we start the scan with the object almost completely inside the collimator (less loss of sensitivity compared to the previous arrangement).

The detectors are continuous NaI 3/8" crystals, with a 1.5 mm intrinsic resolution, divided in pixels of $1.48\,\mathsf{mm} \times 1.48\,\mathsf{mm}$ size. In the rotating system we have 3 146×160 detectors, whereas in the stationary system there is a single cylindrical detector divided in 630×160 pixels. The reconstruction image-space is divided into $146 \times 146 \times 98$ voxels of size $(1.48\,\mathsf{mm})^3$.

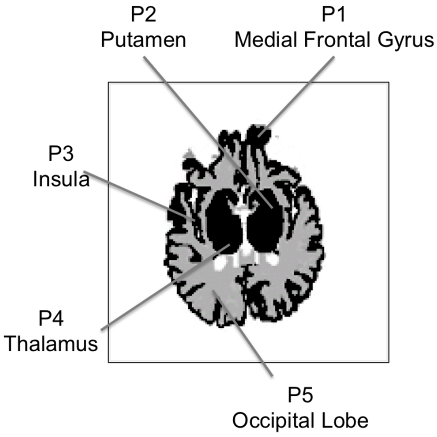

Figure 6.1: A transaxial view of the phantom considered (Hoffman), showing the voxels at which the CRC, variance and CNR are computed (this is the same as in Chapter 4, Section 4.3.1.1).

6.2.2 Evaluation of Image Quality

We model the systems detailed in Section 6.2.1 using the method described and validated in Section 3.3.1. With this method we obtain the system matrix, which is used both for the reconstructions and the analytical evaluation of image quality. The scanning protocol for the rotating system consists of rotating the cameras in intervals of $3°$, and for the stationary system the length of the bed shifts corresponds to the hole pitch in the axial direction. This means that in terms of total angular sampling the two scans should be equivalent.

To evaluate the performance of the systems, we first analyze their sensitivity and resolution throughout the FOV. We obtain the sensitivity map by applying the transpose of the system matrix to a uniform projection of value one, which results in an image whose voxel values correspond to the sum of the sensitivity values of each detector pixel to that image voxel. Then we perform a noiseless reconstruction of a hot-rod Derenzo phantom, with rod diameters between 5 and 10 mm, based on 200 MLEM iterations, in order to compare the resolution.

Finally, we consider a 30 *min* scan of the Hoffman phantom, as described in Section 4.3.1.1 (shown again in Fig. 6.1). It is reconstructed using a PF-PML reconstruction with regularization parameter $\beta = 10^{-6}$ and a 1 cm FWHM post-filtering. We evaluate the CRC, variance, and finally the contrast-to-noise ratio CNR ($CNR = CRC/\sqrt{var}$), at the five

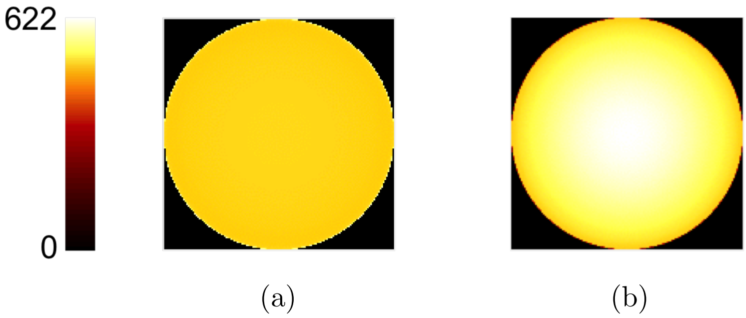

Figure 6.2: Central transaxial slice of the sensitivity map for (a) the rotating system and (b) the stationary system. For each voxel, the intensity in the image represents the geometric sensitivity of the system to that voxel. The values of the color scale are given in cps/MBq.

voxels of interest P_1 to P_5 shown in Fig. 4.1. The convergence value of these figures of merit is computed using formulas (2.31) and (2.32), where the FIM is approximated with the subsampled FIM method with grid G_2 (see sections 4.2.3 and 4.3.1.2). This method showed extremely accurate results in all the cases analyzed in Chapter 4, and in particular it was validated for the rotating SPECT system used here, so we assume it is valid in the case of the stationary system as well.

6.3 Results and Discussion

We start by comparing the two systems in terms of sensitivity (Fig. 6.2) and resolution (Fig. 6.3). We first note that the sensitivity and resolution values have more variation in the case of the stationary system than in the rotating system, as we go from the center to the edge of the field of view. This can be explained by the fact that the height of the holes varies (the holes directed at the center of the FOV are shorter than the ones looking at the edges), whereas their width is kept constant. As we chose the average hole height of the stationary system to be the same as the rotating system, the holes looking at the center will be shorter, and those looking at the edges will be longer. This is consistent with the fact that, in the center, we observe a better sensitivity (622 cps/MBq instead of 500 cps/MBq) but worse resolution (7 mm instead of 6 mm). From this comparison we cannot say that one system is better than the other, merely that the rotating system provides a more uniform

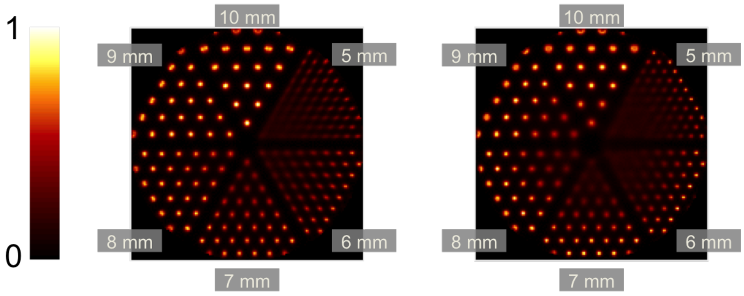

(a) (b)

Figure 6.3: Transaxial view of the reconstructed hot-rod Derenzo phantom for (a) the rotating system and (b) the stationary system.

acquisition of information from the image-space.

For a more quantitative comparison, we show in Fig. 6.4, 6.5 and 6.6 respectively, the CRC, variance and CNR values at 5 representative voxels in the central transaxial slice of the Hoffman phantom (the blue bars represent the rotating system, the red bars the stationary system). As the CRC and variance are measures of resolution and sensitivity, we would expect that the central points (P_2 and P_4) have a higher CRC (better resolution) for the rotating system, as well as a higher variance (worse sensitivity). This is indeed what we observe in Fig. 6.4 and 6.5. The only voxel for which this is not the case is P_1, the voxel furthest from the center, which can be explained by the fact that this point is seen in the stationary system by holes that are longer and closer to the object, compared to the rotating system.

In Fig. 6.6 we see that the CNR, a measure of the overall image quality (resolution-sensitivity trade-off), achieved at each voxel is very similar in both systems. This makes sense, since the points at which there is higher CRC in one system are compensated by a higher variance as well. We observe a small advantage of the rotating system at P_4 (a central point) and a small advantage of the stationary system for voxels P_1 and P_5. This second observation can be explained by the fact that at more external points the stationary system has the advantage of being closer to those points, on average, due to the fact that the cylindrical shape better matches the shape of the human head. However, these differences are quite small, and the rotating system could be further improved with body-contouring, so we cannot definitely conclude that the stationary system provides better image quality for certain parts of the image.

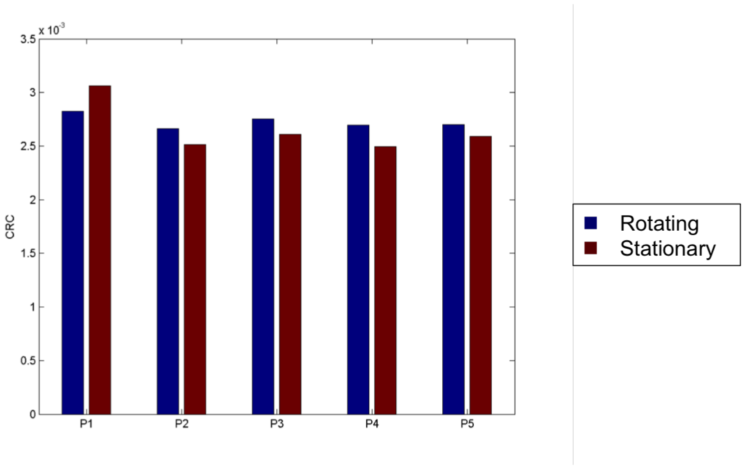

Figure 6.4: The CRC value, computed with the subsampled FIM method with grid G_2, at 5 representative voxels (P_1 to P_5) in the central transaxial slice of the Hoffman phantom. The blue bars represent the values obtained with the rotating system, the red bars the stationary system.

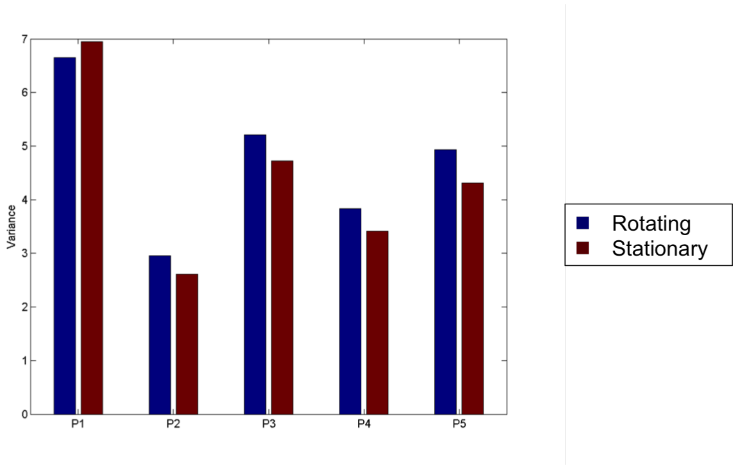

Figure 6.5: The variance value, computed with the subsampled FIM method with grid G_2, at 5 representative voxels (P_1 to P_5) in the central transaxial slice of the Hoffman phantom. The blue bars represent the values obtained with the rotating system, the red bars the stationary system.

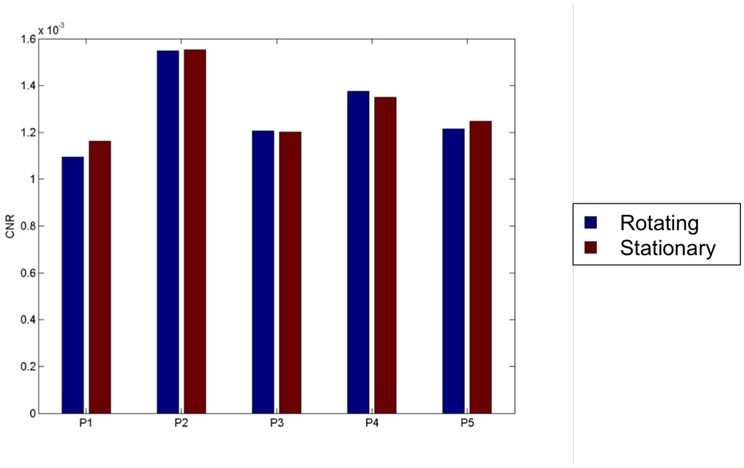

Figure 6.6: The CNR value, computed with the subsampled FIM method with grid G_2, at 5 representative voxels (P_1 to P_5) in the central transaxial slice of the Hoffman phantom. The blue bars represent the values obtained with the rotating system, the red bars the stationary system.

What these results do show is that, in an ideal situation, the image quality provided by the stationary system proposed is similar to that of a standard clinical rotating SPECT system. However, we expect that the movement-related issues (artifacts, time loss, resolution loss...), which are not accounted for here, would more negatively impact the image quality of the rotating system in real practice, since it requires the rotation movement of a heavier object (the entire gamma-camera, as opposed to the patient bed). As such, there would be an advantage to using the proposed system in clinical practice.

6.4 Summary and Original Contributions

In this chapter we performed a comparison study between a standard clinical SPECT system and a system based on the collimator concept proposed in Chapter 5. The two systems were chosen so as to have similar resolution properties on average and the same FOV. We assumed all movements of the systems were perfectly modeled and did not take any time from the scanning. We compared the CRC, variance and CNR at 5 voxels of interest in the central transaxial slice of the Hoffman phantom. From this we observed that for outer points in the phantom the stationary system might have a small advantage (the CNR is higher by a few percentage points) over the rotating system, using standard circular rotation.

In general the image quality of the two systems in the ideal scenario is comparable, so we expect that in practice the stationary system could provide improved image quality. At the moment, however, the cost of producing the collimator would be quite high, at least using our current methods (metal additive manufacturing). As such, we are initially further exploring the concept for small-animal imaging, which we describe in the next chapter, where the collimator is much smaller.

A paper based on this chapter is being prepared for submission to a peer-reviewed A1 journal.

Chapter 7

Collimator Geometry for Highly Compact, Stationary Small-Animal SPECT Imaging

In this chapter we propose a hexagonal collimator geometry, based on the new concept introduced in Chapter 5. This collimator is designed to be used in the compact stationary microSPECT system that has been developed by our group [18]. In Section 7.2.1 the proposed system is presented. Then we describe the simulations performed and the results obtained in sections 7.2.2-7.2.3 and 7.3, and Section 7.4 is the discussion of them. Finally, some brief comments are made on the on-going work of printing the prototype of the proposed collimator and its experimental validation (Section 7.5).

7.1 Introduction

In Chapter 5 we have introduced a new collimator concept for fully-stationary SPECT imaging, i.e. requiring no rotation or translation of either the collimator or the detectors. This concept is based on parallel-holes with a varying angular alignment, arranged in transaxial slices, and it requires only longitudinal bed translations. Because it is stationary, it avoids the drawbacks associated with moving heavy parts of the system during the scanning; because it is based on parallel-holes it allows a larger FOV to be reconstructed, compared to previously proposed fully-stationary systems occupying an equivalent volume. As previously discussed, such a system can be much more compact than standard SPECT systems: compared to rotating SPECT scanners, it does not require space for the rotation mechanism; compared to stationary scanners (based on multi-pinhole collimation), we can bring the collimator and detectors much closer to the object to be imaged, due to the different way the sampling is done. As such, this concept could be very useful for situations in which saving space and material cost is of importance. Furthermore, the fact that the collimator bore is fixed is not as problematic in small-animals as in human (full-body) imaging, because there is less variability in their size.

In the last decade, our research group MEDISIP has been at the forefront of the movement towards highly compact small-animal SPECT systems [146, 18, 147]. This movement has been driven by the development of high-resolution detectors [148, 108, 149], which means that we can reduce the amount of pinhole magnification to achieve the target resolution in the image, and even use minification. Another driver has been the appearance of new techniques for collimator manufacturing [33, 34, 37], as discussed in Section 5.1. These developments have led to the creation of MOLECUBES [150], a spin-off company that develops modular benchtop preclinical imaging systems.

In this chapter we develop a variation of the collimator shown in Chapter 5. The final goal is to use this collimator in the detector setup of the microSPECT system presented in [18], in order to allow the system to image larger mice and rats, which is not possible with the current lofthole collimator.

7.2 Methods

7.2.1 System Design

The system developed in this chapter uses the same collimation principle as described in Chapter 5. In Chapter 5 we described one of the most simple possible designs for such a collimator, based on a cylindrical geometry. However, cylindrical detectors are not standard. Here we test a system (schematic representation in Fig. 7.1) that is designed to fit inside a hexagonal set of detectors, described in [18], made of six 49 mm × 49 mm detector modules with a 0.8 mm of resolution.

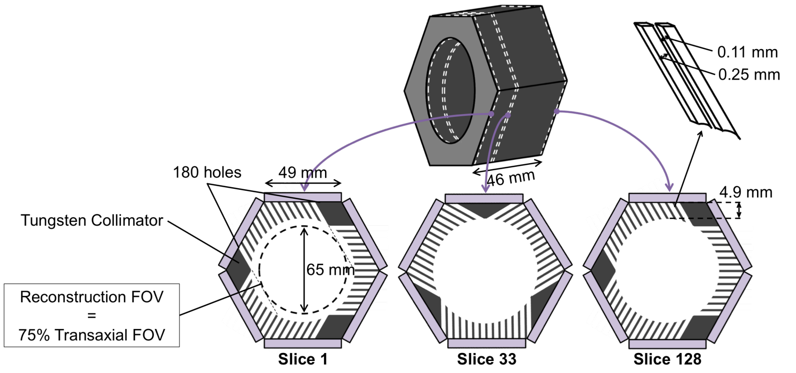

Figure 7.1: Schematic representation of the SPECT system developed in this chapter (not to scale), which has a hexagonal detector setup. It shows the collimator body, sections through the system at slices 1 (first), 33 and 128 (last), and a zoomed-in view of two neighbor collimator holes. This system gives three sampling directions per slice and allows reconstruction of about 75% of the full transaxial FOV.

The collimator body material is tungsten, and its thickness (measured perpendicular to the hexagon side) is $T = 4.9\,\mathrm{mm}$. Each slice has $N_s = 3$ sectors of parallel holes (defining 3 sampling directions), which gives us a reconstruction FOV of diameter $D_{Rec} \approx 65\,\mathrm{mm}$ (enough for an average-size rat). The aperture holes are square prisms, as before, with a width $d = 0.2537\,\mathrm{mm}$ and a transaxial septal thickness $t = 0.1077\,\mathrm{mm}$. These values for d and t were computed for a predicted resolution (averaged over all slices) of $R_{mean} \approx 2\,\mathrm{mm}$ in the center of the FOV and an allowable septal penetration factor of 0.05 for the shortest hole height (so all other holes have less than 5% penetration). This results in $N_h = 180$ holes per section in each slice. Due to the non-symmetrical shape of the collimator, the hole height varies: for example, for the central hole of each row the height a ranges from $4.9\,\mathrm{mm}$ to $11.46\,\mathrm{mm}$. The total axial length of the collimator is chosen to be $L = 46\,\mathrm{mm}$, because even though the detectors span $49\,\mathrm{mm}$ we discard a $\sim 1.5\,\mathrm{mm}$ strip along their edges due to imperfections in the detector manufacturing. This gives us $N = 128$ separate transaxial slices of apertures with an axial separation slightly larger than the septal pitch ($0.1094\,\mathrm{mm}$). We considered only one slice per angular direction, i.e. there is rotation of sampling direction between every adjacent slice. Therefore, the angular increment between the hole directions in subsequent slices is $\Delta\alpha = 120°/128 \approx 0.94°$. If we choose the bed position stepping as having the same size as the thickness of a

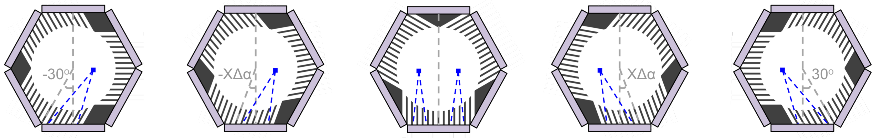

Slice 1 Slice 33-X Slice 33 Slice 33+X Slice 65

Figure 7.2: The system symmetries which we use to reduce the number of system matrix elements computed. The figure shows schematic representations of several transaxial slices of the collimator. In each slice, a voxel is shown with the corresponding projection. For the slices on the left the voxel position is symmetric to the voxel position for the slices on the right, with respect to the line perpendicular to the bottom detector, and the projections corresponding to these voxels are also symmetric, for the corresponding slice.

transaxial slice, this corresponds to a very fine sampling.

As a final note, we can see that in this system the collimator and detectors come very close to the object to be reconstructed: we are able to achieve full angular sampling in a transaxial FOV whose diameter (65 mm) is larger than the detector size of 49 mm. The total system height, including the 4 mm-thick detectors, is 92.8 mm, its width is 106 mm and its axial length is about 49 mm. Even though this is a simplified value (other components need to be added for the scanner to function), this makes it a much more compact system than current stationary SPECT scanners, as well as less expensive to produce (less detectors and collimator material).

7.2.2 System Matrix

In the simulations described in this chapter (sensitivity map and reconstructions), the system matrix elements are computed using the analytical model described in Chapter 3, Section 3.3. Furthermore, certain strategies were used to speed up the calculation of the system matrix elements, which we describe here. First of all, for each detector pixel we only loop over a few collimator holes, which we have determined to be the only ones through which photons can reach the pixel. Secondly, we exploit symmetries in the system (Fig. 7.2). Note that on slice 33 the portion of the collimator that projects onto each detector is symmetric with respect to a line going through the center of that detector (dashed gray line in Fig. 7.2). This means that two voxels whose locations are symmetric with regards to this line will have the same projection onto the detector, but symmetric with respect to the line. Similarly, since the angular shift between consecutive slices ($\Delta\alpha$) is constant, this means that the voxel projections onto the detector through collimator slice number 33-X ($\alpha = \alpha_{33} - \mathsf{X}\Delta\alpha$) will be symmetric to those of voxels at symmetric locations through slice number 33+X ($\alpha = \alpha_{33} + \mathsf{X}\Delta\alpha$), with respect to that same line, for $\mathsf{X} \leq 32$. As such, if we compute the detector response to photons coming from the image space through the holes in slice 33-X, then by simple symmetry operations and a linear shift in the axial direction we obtain the equivalent for slice 33+X. By repeating this reasoning for all the slices in the collimator, we only need to do the explicit sensitivity calculations for about half of the total number of collimator holes. Note that since we have discrete projection- and image-spaces, to take advantage of the symmetries in the axial direction we considered the voxel pitch as having the size of the hole pitch in the axial direction, and the pixel pitch as half of this value. Finally, also thanks to the system symmetry, we do the explicit system matrix calculations for only 1 of the 6 detectors. To obtain the projection corresponding to the other 5 detectors, we merely rotate the image accordingly, using bilinear interpolation, and for 3 of the detectors we also need to change the order of the collimator slices to obtain the correct projection.

7.2.3 Simulations

In this section we describe the different experiments which we perform to investigate the performance of the proposed stationary small-animal SPECT system. In all the experiments we consider a useable detector area of $46\,\mathsf{mm} \times 46\,\mathsf{mm}$, which is divided into 256×256 pixels of $0.18155\,\mathsf{mm}$ pitch. The image-space is defined as $180 \times 180 \times 180$ voxels of $0.3631\,\mathsf{mm}$ pitch, resulting in a $\sim 65\,\mathsf{mm} \times 65\,\mathsf{mm} \times 65\,\mathsf{mm}$ cube, but we only allow non-zero values for voxels inside a $65\,\mathsf{mm}$-diameter cylinder (the reconstruction FOV). For the reconstructions we apply 200 iterations of MLEM, using the system matrix computed with the method described in Section 7.2.2.

7.2.3.1 Sensitivity, Resolution and Noiseless Reconstructions

We first compute the system sensitivity for each voxel in the reconstruction FOV, for one bed position. We do this using the analytical system matrix, since it gives the sensitivity of a each detector pixel to each image voxel. With this data we determine the mean sensitivity value over the FOV.

Noiseless projection data is also reconstructed. The three phantoms considered are: a) a cylindrical uniform phantom, of 14.5 mm height and 65 mm diameter; b) a hot-rod Derenzo phantom, where each sector contains cylinders of 14.5 mm height and diameters ranging from 1 mm to 2 mm; c) a cold-rod Derenzo phantom, where the rods described in b) are removed from a uniform cylinder of 14.5 mm height and 65 mm diameter. In all phantoms, the activity regions have a value of 1. The phantoms' symmetry axis is oriented along the axial scanner direction, and the scanning protocol consists of 42 steps along the axial direction, with each step corresponding to the thickness of 4 transaxial slices of the collimator ($\sim$ 1.5 mm). These noiseless reconstructions allow us to check for artifacts (which could be caused, in particular, by insufficient sampling), and the Derenzo phantoms allow us to estimate the actual resolution after reconstruction for our system.

7.2.3.2 Noisy Reconstructions

Finally, we perform reconstructions from realistic (noisy) projection data, to test the performance of the system in practice. We simulate again a cylindrical uniform phantom, as described in section 7.2.3.1, with a total activity of 75 MBq of ^{99m}Tc and a scanning time of 1 *min* per bed position. The reconstructed phantom is post-smoothed with a Gaussian filter of 1 mm FWHM. Then we simulate a ROBY phantom [137], i.e. a digital representation of a rat, scaled down to fit inside the 65 mm-diameter cylindrical FOV, resulting in an image of $180 \times 180 \times 720$ voxels. The total activity injected is 75 MBq of ^{99m}Tc-tetrofosmin, where the relative organ activity distribution is based on [151]. In this case, one bed shift corresponds to 5 collimator slices, i.e. $\sim$ 1.8 mm, for a total of 168 bed positions in a 1 hour scan. Here we apply a 2 mm FWHM Gaussian post-smoothing, due to the fact that the scan in shorter and that the same activity is distributed over a longer phantom, as well as more concentrated on specific areas of the phantom, so the projections will be more noisy (less counts).

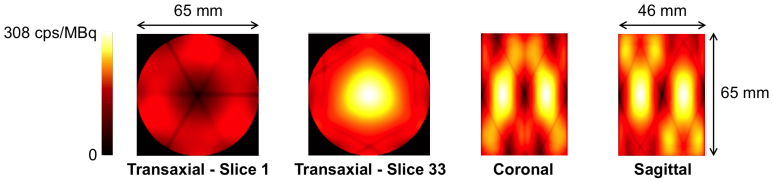

Figure 7.3: Sensitivity map for one bed position. For each voxel, the intensity in the image represents the total sensitivity of the system (including detector efficiency) to that voxel.

7.3 Results

7.3.1 Sensitivity, Resolution and Noiseless Reconstructions

The analytically determined sensitivity of the system to each voxel in the reconstruction FOV, a cylinder of 46 mm length and 65 mm diameter, is shown in Fig. 7.3 (for one bed position). Note that this is not only the pure geometric (collimator) sensitivity, it is scaled down to take the 80% detector efficiency into account. What we see, first of all, is that the sensitivity profile is quite different for the different collimator slices, which is due to the fact that the heights of the collimator apertures vary from slice to slice. We can observe that the highest sensitivity values are achieved in the center of the FOV, and the collimator slices in which this occurs (e.g. slice 33) are the ones in which aperture holes (in particular, those looking at the center of the FOV) achieve the smallest possible hole height (see Fig. 7.1). We also see straight dark lines in the figure, along different directions according to the transaxial slice; these are the backprojection lines from the edges of the detector modules, which we have discarded as we would in a real experiment. These change position according to the aperture holes that project onto that part of the detector in that slice (see Fig. 7.1). Averaging along the axial direction (since the phantom will be translated along this direction), the mean sensitivity at the center is 182 cps/MBq (incorporating the detector efficiency), and at a point on the outer edge of the reconstruction FOV it is 100 cps/MBq. The average sensitivity over the entire reconstruction FOV is 148 cps/MBq.

Next we present the results from noiseless reconstructions. First we have, in Fig. 7.4, the reconstruction of the cylinder, which shows good uniformity and therefore indicates that with this system and sampling protocol we have enough angular sampling throughout the desired FOV

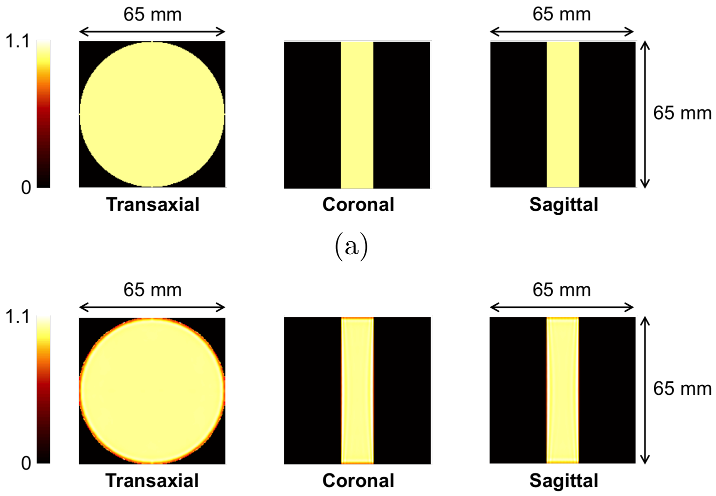

(a)

(b)

Figure 7.4: The uniform cylindrical phantom (a) and its noiseless MLEM reconstruction (b).

of 65 mm diameter. Then we show the reconstruction of a hot and a cold Derenzo phantoms, in Fig. 7.5 and 7.6 respectively, and from these we deduce that the resolution after reconstruction is about 1.6 mm at the center and about 1 mm for the outer points. The fact that the resolution improves as we go towards the edge of image-space is consistent with the previous observation that the sensitivity decreases. It can be intuitively explained by the fact that photons originating in rods which are close to the collimator will go through a small number of aperture holes in at least one side of the collimator, so the system is better able to distinguish them.

7.3.2 Noisy Reconstructions

The reconstructions from noisy projection data obtained from the uniform cylinder and the ROBY phantom are represented in Fig. 7.7 and 7.8, respectively. They both show good agreement with the corresponding phantom, and no sampling artifacts. In the uniform phantom reconstruction, we can clearly observe that the image is less noisy and more blurry in the central region, compared to the edges, which is consistent with the results in Section 7.3.1. In the ROBY phantom reconstruction, for which we use a realistic activity value and total scanning time, we

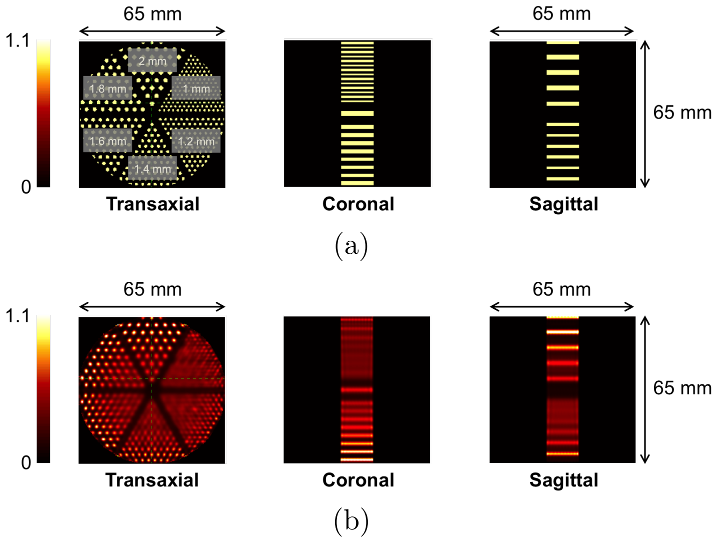
65 mm
1.1
0
2 mm
1.8 mm
1 mm
1.6 mm
1.2 mm
1.4 mm
Transaxial
Coronal
Sagittal
65 mm
65 mm
(a)
65 mm
1.1
0
Transaxial
Coronal
Sagittal
65 mm
65 mm
(b)

Figure 7.5: The hot-rod Derenzo phantom (a) and its noiseless MLEM reconstruction (b). The coronal and sagittal slices are taken through the dashed green lines.

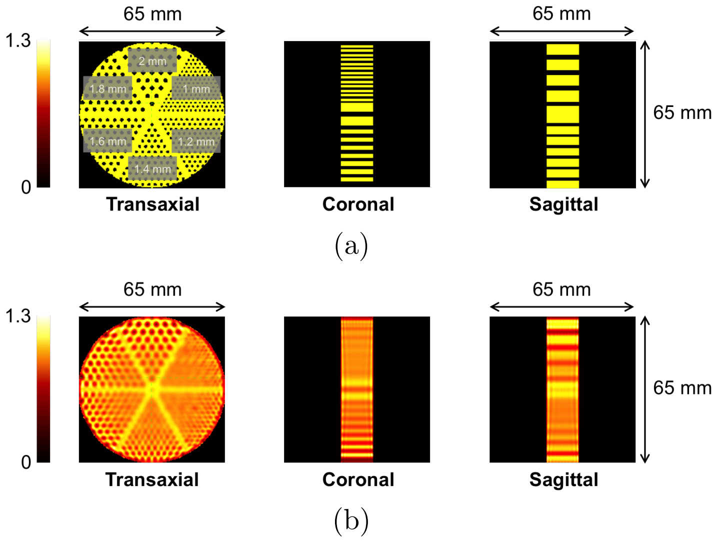
65 mm
1.3
0
2 mm
1.8 mm
1 mm
1.6 mm
1.2 mm
1.4 mm
Transaxial
Coronal
Sagittal
65 mm
65 mm
(a)
65 mm
1.3
0
Transaxial
Coronal
Sagittal
65 mm
65 mm
(b)

Figure 7.6: The cold-rod Derenzo phantom (a) and its noiseless MLEM reconstruction (b). The coronal and sagittal slices are taken through the dashed green lines.

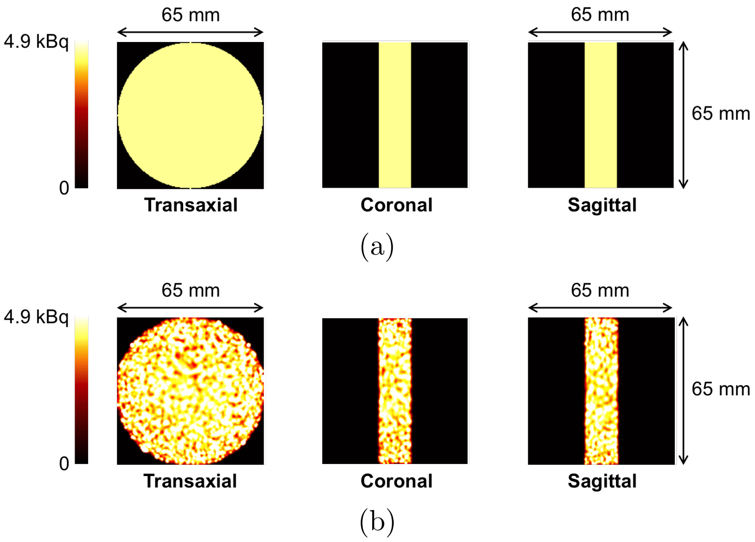
65 mm
4.9 kBq
0
Transaxial
Coronal
65 mm
65 mm
Sagittal
65 mm
4.9 kBq
0
Transaxial
Coronal
65 mm
65 mm
Sagittal

(a)

(b)

Figure 7.7: The uniform cylindrical phantom (a) and its MLEM reconstruction from noisy projections (b).

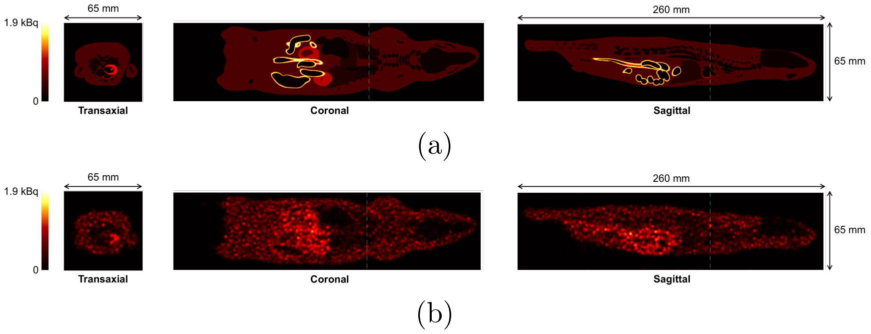
65 mm
1.9 kBq
0
Transaxial
Coronal
260 mm
65 mm
Sagittal
65 mm
1.9 kBq
0
Transaxial
Coronal
260 mm
65 mm
Sagittal

(a)

(b)

Figure 7.8: The ROBY phantom (a) and its MLEM reconstruction from noisy projections (b). The transaxial slice is taken through the dashed green lines.

can distinguish the most relevant structures in the body, but the image is quite noisy. This reflects that to achieve this resolution our system is designed to have quite a low sensitivity.

7.4 Discussion

In this chapter we have developed a new system to be used for highly compact, fully stationary small-animal SPECT imaging, based on the collimator concept first presented in Chapter 5. We performed reconstructions from noiseless and noisy simulated projections of several phantoms. We conclude that the system could be used to image objects with a diameter of about 65 mm (about the size of a rat), corresponding to about 75% of the transaxial FOV, with a resolution of less than 2 mm, using only axial bed shifts. This is true also for a realistic whole-body rat scan, even though it results in quite noisy images.

For a given point, the sensitivity-resolution trade-off may not be as advantageous as in other currently available small-animal SPECT systems. As an example, we can compare the system's performance with the U-SPECT-II [17], a standard stationary small-animal SPECT system, using its rat collimator with 1 mm-diameter pinholes, which allows imaging of rats with a maximum diameter of 62.5 mm, similarly to our system (65 mm). Our simulations indicate a mean sensitivity of 182 cps/MBq for points with a 1.6 mm resolution. The U-SPECT-II, on the other hand, is reported as having a mean point sensitivity of 700 cps/MBq for a resolution of 0.8 mm [17]. The reason why the U-SPECT-II is able to achieve this has to do with the fact that it focuses on a small region of the FOV and uses a high magnification factor, but this also means that it occupies a much larger volume than our system to image a similar-sized object: the inner volume of the detector arrangement is of 42575 cm^3 for the U-SPECT-II (3 50.8 cm × 38.1 cm detectors arranged in a triangle) and only 306 cm^3 in our system (6 4.9 cm × 4.9 cm detectors arranged in a hexagon). Note also that the point sensitivity of 700 cps/MBq in the U-SPECT-II is valid only for the central FOV (that which is seen by all its pinholes), a cylinder of diameter 27 mm and length 11 mm; this value will be lower for the remaining FOV (which is covered by less pinholes), and to do a true comparison of the two systems it would be necessary to compute the mean sensitivity and resolution values over the entire FOV, but this information is not provided for the U-SPECT-II system in literature.

Because the system is so compact and the phantom comes so close to the collimator and detector, it has the particular property that the resolution improves as we go from the center to the edges of image-space. The opposite happens with the sensitivity (averaged over all transaxial aperture slices). This effect is similar to what had been already observed in Chapter 5.

We conclude that it is viable to use such a system in practice, and even though there are other small-animal systems, both moving and stationary, which provide a better sensitivity-resolution trade-off, our system presents particular advantages that can be useful in many practical situations. Due to its stationary nature, it should be less time-consuming or prone to motion artifacts than non-stationary SPECT scanners, as well as allow simultaneous MRI imaging. Compared to previously suggested fully-stationary SPECT systems, it is able to achieve full angular sampling of a much larger portion of the entire system's volume, and using only longitudinal bed translations. Because of its much more efficient use of space compared to the other stationary (as well as non-stationary) SPECT systems which have been proposed until now, it allows us to have much more compact preclinical systems, therefore saving both space and material costs. This new type of collimator can also easily be placed in already existing SPECT scanners to replace other collimators, since it only requires longitudinal movement of the patient bed, thereby making it cheap and practical to use, and its small size makes it particularly suitable for the integration of SPECT with MRI scanners. Due to the large FOV but poor sensitivity-resolution trade-off achieved, one could also use the system for a low-resolution full-body scout scan and then use a multi-pinhole collimator for high-resolution imaging of a smaller region-of-interest. This should reduce the artifacts that usually appear in multi-pinhole systems at undersampled regions of the FOV.

7.5 Manufacturing and Preliminary Experimental Results

Based on this design, we investigated the possible manufacturing methods for the collimator. It is not possible to achieve such an intricate geometry with molds (at least not directly), so we explored the option of production via metal additive manufacturing [33, 34], with the company Layerwise (Belgium). This is a 3D Printing technique in which a thin layer of metal powder (in our case tungsten powder) is laid down

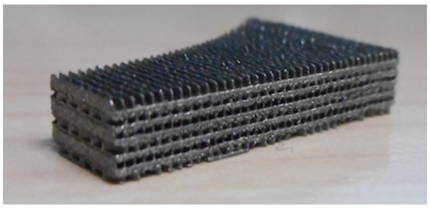

Figure 7.9: Test piece of the collimator, printed using metal additive manufacturing, where the printing was done along the axial direction.

on a horizontal plane, then a laser selectively melts the parts which we want to keep in the final product, and afterwards a new layer of powder is added on top and the process is repeated until the product is complete. The unwanted parts (those that should not be filled) remain in powder form and are removed after the process. For a more in-depth explanation of this process see [33].

Because each layer is built on top of the previous, the walls of the aperture holes (empty areas of the collimator) need to have enough support, and this posed certain restrictions to the design. Our first idea was to build the collimator in one piece, by printing one transaxial slice at a time, i.e. the tungsten powder layers were set along the transaxial direction of the collimator. This meant that the septa between the transaxial slices had to be at least 0.5 mm, and therefore thicker than in the original design. The first test piece printed using this method is shown in Fig. 7.9, which contains a portion of 6 transaxial slices. In the picture one can clearly see that more material is present between the slices than between apertures belonging to the same slice. In this design, besides the loss in detector usage from the additional collimator material between slices, the layers collapsed too much over each other, and many apertures were even completely obstructed. As such, it was decided that this option was not viable.

The second attempt at printing the collimator was based on stacking the metal powder layers parallel to one of the collimator faces that connects to a detector plate. However, in this case the aperture holes could not be at an angle lower than 60° with the horizontal plane, in order for their walls to have enough support. This rule would necessarily be violated if we would print the collimator in one piece only, so we decided to divide it in 3 parts. These parts connect at the point in each slice where two sectors of aperture holes come together. A schematic view of one such piece is shown in Fig. 7.10. This last design process was

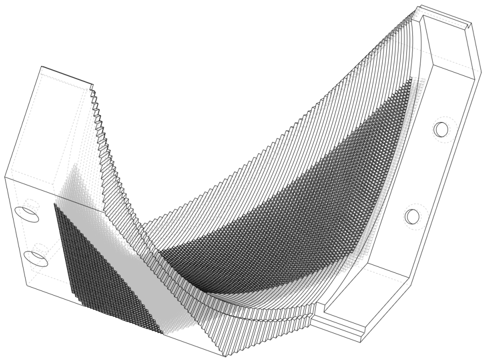

Figure 7.10: Schematic drawing of one of the 3 pieces in which the collimator was divided in order to be printed.

followed and the 3 pieces making the full collimator were manufactured by the additive manufacturing company Layerwise (Belgium). Pictures of the finished product can be seen in Fig. 7.11.

This first collimator prototype was inserted inside the existing detector setup that is currently being used with a multi-lofthole collimator [18]. A system matrix with 1 mm voxels was measured by point source measurements acquired in a 2 mm grid, followed by interpolation, within a cylinder of 49 mm diameter. One of the first reconstruction images is shown in Fig. 7.12. These initial results are still very preliminary, and require further refinement. We can see extra activity at the edges of the field of view, which is probably related to inconsistencies between the real system and the model that is used in the reconstruction: activity that is placed outside of the allowed image-space will tend to accumulate at the edges. However, these results indicate that the system is indeed able to achieve enough sampling for stationary reconstruction, at least in the central part of image-space.

7.6 Summary and Original Contributions

In this chapter we have proposed a novel system and acquisition method for stationary SPECT imaging. Using tilted parallel holes, we are able to enlarge the transaxial surface where there is complete angular sampling, while keeping the system very compact, compared to current SPECT systems. The collimator is designed to fit in a pre-existing hexagonal detector setup.

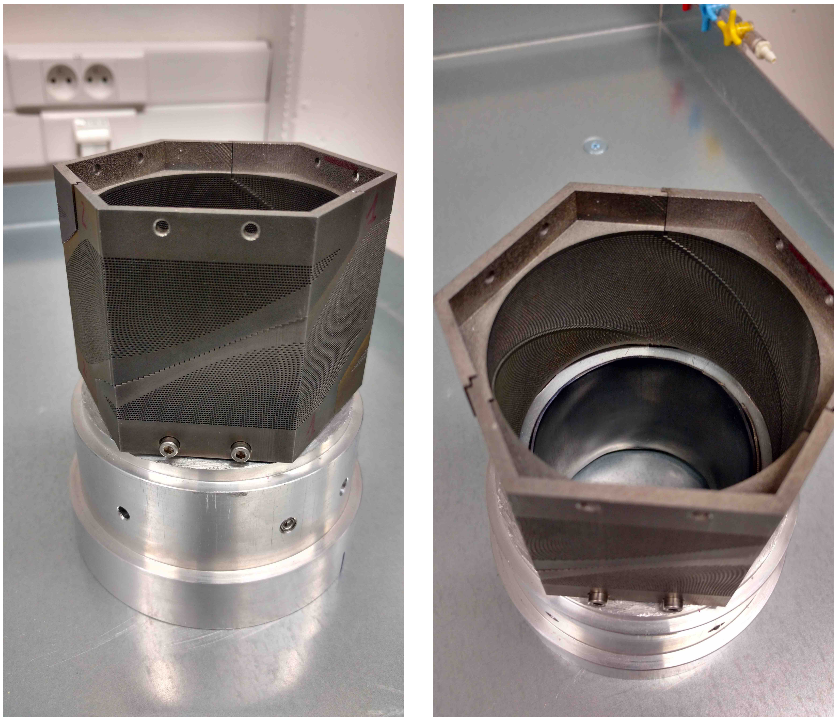

Figure 7.11: Photos of the full collimator from two different views, showing the three printed parts fitted together.

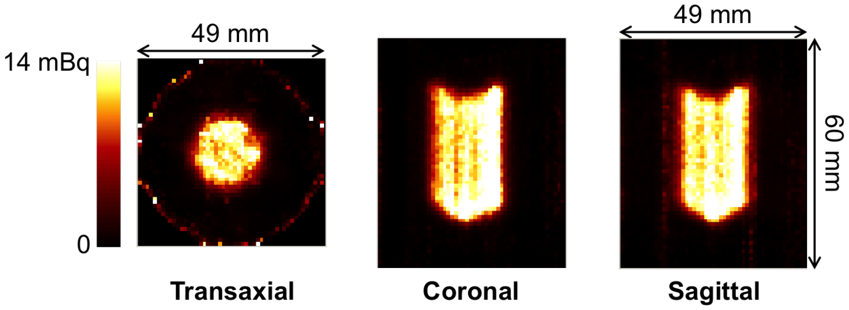
14 mBq
0
49 mm
49 mm
60 mm
Transaxial
Coronal
Sagittal

Figure 7.12: Reconstruction of a partially filled 20 ml syringe, scanned with 675 μm axial bed steps while keeping the system stationary. The images shown result from 50 MLEM iterations.

We simulated noiseless and realistic reconstructions using a possible system configuration and scanning protocol for small-animal imaging. From the results we concluded that the system could be used to image objects with a diameter of about 75% that of the circle inscribed in the collimator, with a resolution of 1.6 mm after reconstruction.

These results led us to design and print a prototype collimator, which is in the process of experimental validation.

The developments discussed in this chapter have been published in a conference abstract [152] and have also contributed to the patent application [140]. The final collimator design that we produced was performed by Roel Van Holen. The computation of the experimental system matrix and the reconstruction using the initial prototype have been performed by Karel Deprez.

Chapter 8

Conclusion

8.1 Summary

This dissertation treated the development of innovative SPECT systems. In a first stage we developed an accurate and efficient approach for modeling such systems. Secondly, we investigated techniques for evaluating the quality of the images obtained with SPECT systems, which can help guide their design and compare their performance with other systems. Thirdly, we proposed a new type of collimator for stationary SPECT imaging whose innovative design presents several advantages compared to state of the art systems. Finally, we investigate several applications of this new collimator concept for SPECT imaging.

We will now give a summary of the research described in each chapter of this thesis, along with the main results and conclusions.

To start off, in **Chapter 2** we described some fundamental concepts within SPECT imaging which help the reader understand the remainder of the thesis. We first explained the process of image acquisition using a SPECT scanner, and the basic components of the system. One of these components is the collimator, which being one of the main focal points of the dissertation we proceeded to analyze in more detail. We defined the concepts of collimator FOV, sensitivity and resolution, and derived them for the two types of collimator considered in this thesis (pinhole and parallel-hole). We also gave an idea of the latest developments in collimator production techniques and how they have been shaping a new era of collimator design. In the following section we spoke about image reconstruction algorithms: we first introduced the imaging problem, then the important class of iterative image reconstruction, and then we described the commonly used MLEM and PML algorithms (the reconstruction algorithms applied in this dissertation). Next we explained what system modeling means in the context of SPECT imaging, and the three most important types of methods for doing so: analytical, Monte Carlo and experimental methods. Finally, we discussed different methods for the assessment of IQ in SPECT: sensitivity-resolution trade-off, objective assessment of IQ, and the FIM-based approximation of the local impulse response and covariance.

In **Chapter 3** we developed analytical approaches for modeling collimator response. The computations themselves are much faster than Monte Carlo or experiment-based methods, and are versatile enough to be applicable to many different geometries. The chapter was divided into two parts: the first treating pinhole-type collimators, and the second for parallel-hole-type collimators. In the first part we derived formulas for the total point sensitivity of a pinhole with circular exit and a lofthole with square exit, and validated them using a simple ray-tracer. The analytical formulas showed a very good match with the ray-tracer, which is especially relevant in the Low Sensitivity and No Sensitivity regions, where the standard formula does not predict the correct behavior. In the second part we described a method to compute the sensitivity of each detector bin to a point source for non-standard shapes of parallel-holes. We validated it for a cylindrical and hexagonal systems with holes that gradually change direction as we move along the axial direction, with realistic Monte Carlo simulations. We observed that our analytical modeling matches the projection data from Monte Carlo simulations very closely, both in terms of shape and number of counts. Based on these results, we used the methods described in this chapter throughout the rest of the dissertation for system modeling and reconstructions.

In **Chapter 4** we investigated different approximation methods for the FIM-based calculation of the local impulse response and covariance, a popular approach for evaluation of image quality in SPECT. These approaches, which have previously been proposed by different authors, are the so-called LSI, NUOP and subsampled FIM. We described the theoretical framework and the assumptions behind them, and then compared them to a gold standard method in the case of standard parallel-hole and standard pinhole SPECT systems. We showed that the conditions of validity of the popular LSI approach can easily be broken in such systems, and we should therefore be careful using it. In the cases evaluated here, we found that the NUOP and subsampled FIM approaches performed much better in general, coming quite close to the gold standard values, which could indicate that they are potentially a better alternative to the LSI in approximating the FIM in this context of IQ. This study is, however, not exhaustive, so the conclusions are only valid for the examined systems.

Chapter 5 described a new approach for collimation in stationary SPECT, which is based on parallel-holes with a varying angular alignment, arranged in transaxial slices. This novel collimator design allows for full angular sampling of objects coming quite close to the collimator bore, and the scanning protocol involves only axial bed translations. This means that the system should have the advantages of stationary systems (such as stability, improved image quality...), while being more compact and light compared to current state-of-the-art systems. In this initial study we proposed three different applications for this new type of system, for full human body, human brain and small-animal imaging, respectively. The three systems were cylindrically shaped, for simplicity, and their settings were chosen to be comparable to commercially available SPECT systems. Using the analytical method described in Chapter 3, we modeled the systems and evaluated their sensitivity, resolution and uniformity in reconstructions. The sensitivity and resolution values were similar to what we would obtain from standard parallel-hole SPECT systems with the same settings, but the values obtained were less uniform throughout the FOV, due to the varying collimator aperture heights. From the reconstruction of a uniform phantom we also concluded that the system is able to reconstruct objects occupying about 75% of the transaxial area of the bore without artifacts. Finally, we performed reconstructions from noisy projection data, simulated from a realistic scanning protocol, and obtained images that could be used in clinical/preclinical practice. At the end of the chapter we discussed possible applications and advantages of the system, and concluded that brain and small-animal imaging seem to be some of the most promising applications. This would be further developed in chapters 6 and 7.

Then in **Chapter 6** we took the brain SPECT system proposed in the previous chapter and compared its performance (i.e. the IQ of its images) with a standard rotating parallel-hole system similar to what is used in clinical practice, both systems having the same FOV and average resolution. The sensitivity and resolution properties throughout the FOV are comparable in both systems, the main difference being that they are less uniform in the proposed stationary system, as noted in Chapter 5. As such we moved on to a more quantitative comparison, using the best-performing FIM-based method from Chapter 4 (subsampled FIM method with grid G_2, which was validated for this type of system) to evaluate the CRC, variance and CNR at 5 voxels of interest; in this case, the stationary system showed a slightly better performance based on these FOMs. Although these results cannot be directly generalized, they are an indication that the IQ of the two systems is at least comparable, in this ideal situation and assuming no systems imperfections. In reality, the fact that a system is rotating should create additional inaccuracies in the system modeling, so the IQ might be even worse compared to the proposed stationary system, in addition to the other advantages previously mentioned.

Finally, in **Chapter 7** we developed another variation on the system proposed in Chapter 5, this time a hexagonal collimator design for small-animal imaging. This was done for practical reasons, because it would fit an already available detector setup, thereby making it easier to build the actual system. The system modeling was done once again based on the analytical method developed in Chapter 3, and the system matrix calculation was made more efficient by using the system's symmetries. The system performance was evaluated based on sensitivity and resolution, and the values obtained indicate that the sensitivity-resolution trade-off is not as good as that obtained in other state-of-the-art small-animal SPECT systems. Our system does, however, possess other advantages which we described in the Discussion section, namely the fact that it is much more compact than its stationary counterparts. We also observed the system's ability to reconstruct both noiseless and noisy images, including a realistic scanning protocol for full-body imaging of a rat; we concluded that a system with these dimensions, at least in the ideal case, could be used to image objects with a diameter of about 75% that of the circle inscribed in the collimator, without artifacts, with a resolution of about 1.6 mm or less after reconstruction, which can be useful in practice. At the end of the chapter we briefly described the manufacturing of a prototype of the proposed collimator, based on this design, and the first experimental results obtained, but this work is still in the preliminary stages.

8.2 Future Research

There are several areas in which the research presented in this dissertation could be improved and further explored.

The simulations presented throughout this work could be framed in a more realistic way, which would provide a more accurate view on the performance of the methods and systems under investigation. In particular, collimator penetration/scatter and phantom attenuation/scatter should be modeled, as well as the physical particle interactions (with e.g. Monte Carlo simulations), as these can have a significant influence on the final results, and this was not done in any of the simulation work. This would be especially valuable for the development of the systems proposed in chapters 5 to 7, based on the novel collimator concept, since they are new, untested systems.

The formulas presented in Chapter 3 for the sensitivity of pinhole-type collimators have only been derived for two specific system geometries, so many more geometries remain to be described, and efficient ways of generalizing the calculation could be found. The system modeling of the parallel-hole systems could also include more effects other than the collimator geometry, in particular the modeling of the interaction in the detector.

The studies evaluating the performance of different methods for evaluation of IQ (Chapter 4) and also comparing the performance of two systems (Chapter 6) could be more thorough: more images could be analyzed, more points of interest tested, etc. The main reason this was not done here was due to the very long computing times, but as a consequence the results could not be very conclusive. It is especially important for the nuclear imaging field in general that the LSI, NUOP and subsampled FIM approximations be further validated, since these types of approaches (especially the LSI) are widely used in literature.

From the collimator concept first presented in Chapter 5, many more SPECT system designs can be explored, as the idea could be useful for several applications which were not considered in this thesis. For example, different shapes of collimator body and aperture holes can be used, and the direction of the apertures can be changed to fanbeam or conebeam geometries. Besides the full-body, brain and small-animal systems developed here, it would be very interesting to study the use of the collimator in e.g. a SPECT-MR scanner, or in a low-resolution scout-scan preceding high-resolution imaging on the ROI. Furthermore, the systems proposed here were not optimized but merely based on the settings of currently exiting SPECT systems, so more work can be done on improving their performance (having a collimator bore that more closely matches the body shape, optimizing the aperture dimensions, etc.).

Because of the complex collimator geometry proposed, it would also be important to examine how sensitive the reconstructions are to mismatches between the real system and the system modeling of the projection/backprojection operations. These effects are not considered in this dissertation, since the system modeled is exactly the same in both the projection data and the reconstruction. However, this issue can be avoided by using an experimental system matrix.

Finally, it will be crucial to explore the practical aspects of manufacturing such a collimator. With the current manufacturing method, based on metal additive manufacturing, we are limited to building small collimators (for small-animal imaging), especially due to the high cost and the long manufacturing time. In the future we could explore other manufacturing techniques or ways of performing the additive manufacturing that would make the process less expensive and more efficient.

As explained at the end of Chapter 7, the first prototype of the collimator concept proposed in this dissertation is being experimentally tested, and the results seem promising. If we are able to obtain good results in reconstructions, the collimator could be incorporated in a small-animal SPECT scanner which is being developed at the MEDISIP lab. This would allow the system which is currently rotation-based to be used in stationary mode, and to image rats as well as mice.

8.3 Final Conclusion

Innovative collimator design can be used to improve the performance of SPECT systems for certain applications, and open new doors to what can be done with this medical imaging modality. With the advent of metal additive manufacturing, this area is now rich with new possibilities. In this dissertation we have investigated methods for the modeling and evaluation of IQ in SPECT systems, and with the help of these tools developed a new collimator concept.

We first developed methods to model complex collimator geometries analytically. These methods are both accurate and highly efficient, and can be used in the modeling of many SPECT systems. With the increasing variety in SPECT collimator geometries, such methods can become very useful. In this dissertation they were used to simulate the acquisition of projection data by the scanner as well as to make the system matrix used in reconstructions.

Secondly, we evaluated efficient methods for IQ assessment in SPECT.

In particular, we analyzed approximations of FIM-based figures-of-merit, which are relatively easy and efficient to use. We discovered that, in the cases we studied, the most popular approximation used in literature, the LSI, is outperformed by some less-known approaches, the NUOP and subsampled FIM, which indicates that more care should be taken when applying these approximations.

The later chapters of the thesis deal with the development of a new type of collimator, where parallel-hole apertures are arranged in transaxial slices, each presenting a different angular alignment, such that angular sampling of the object can be achieved by longitudinal translation of the patient bed alone (stationary imaging). This presents several advantages compared to rotating SPECT systems (the standard approach), especially in terms of stability and IQ. Compared to other stationary SPECT systems (based on multi-pinhole collimators), it is able to be more compact, which should save space and also possibly costs in material. We have explored several different designs for the collimator, for full-body, brain and small-animal imaging. We concluded that in all three applications the system could be used to obtain satisfactory reconstructions. The best-performing approach used in the FIM-based evaluation of IQ was used to compare the proposed brain SPECT system with a standard parallel-hole SPECT system, and a slight improvement in IQ was observed, which is a good indication since the rotation-related degradation of IQ was even not considered. For the small-animal SPECT system, we have discovered that the sensitivity-resolution trade-off is not the best, compared to other state-of-the-art SPECT systems, however the system could still be useful due to its other qualities. In fact, we intend to explore the application in small-animal imaging further, and we are working on the experimental validation of the first prototype of the system.

References

[1] https://commons.wikimedia.org/wiki/File:Radiografia_pulmones_Francisca_Lorca.jpg.

[2] https://commons.wikipedia.org/wiki/File:Ct-workstation-neck.jpg.

[3] https://commons.wikimedia.org/wiki/File:UltrasoundBPH.jpg.

[4] https://commons.wikimedia.org/wiki/File:MRI_brain.jpg.

[5] https://commons.wikimedia.org/wiki/File:PET-image.jpg.

[6] http://molecubes.com/gammacube.html.

[7] http://www.infinityugent.be/technology/technologysub.

[8] G. Mariani, L. Bruselli, T. Kuwert, E. E. Kim, A. Flotats, O. Israel, M. Dondi, and N. Watanabe, "A review on the clinical uses of SPECT/CT," *European Journal of Nuclear Medicine and Molecular Imaging*, vol. 37, no. 10, pp. 1959–1985, 2010.

[9] G. C. Kagadis, G. Loudos, K. Katsanos, S. G. Langer, and G. C. Nikiforidis, "In vivo small animal imaging: Current status and future prospects," *Medical Physics*, vol. 37, no. 12, pp. 6421–6442, 2010.

[10] M. M. Khalil, J. L. Tremoleda, T. B. Bayomy, and W. Gsell, "Molecular SPECT Imaging: An Overview," *International Journal of Molecular Imaging*, vol. 2011, 2011, Art. ID 796025.

[11] J. R. Mallard and M. J. Myers, "The performance of a gamma camera for the visualization of radioactive isotopes in vivo," *Physics in Medicine and Biology*, vol. 8, no. 2, pp. 165–182, Jun. 1963.

[12] M. F. Smith and R. J. Jaszczak, “The effect of gamma ray penetration on angle-dependent sensitivity for pinhole collimation in nuclear medicine,” *Medical Physics*, vol. 24, no. 11, pp. 1701–1709, Nov. 1997.

[13] N. U. Schramm, G. Ebel, U. Engeland, T. Schurrat, M. Behe, and T. M. Behr, “High-resolution SPECT using multipinhole collimation,” *IEEE Transactions on Nuclear Science*, vol. 50, no. 3, pp. 315–320, Jun. 2003.

[14] L. Furenlid, D. Wilson, Y.-C. Chen, H. Kim, P. Pietraski, M. Crawford, and H. Barrett, “FastSPECT II: a second-generation high-resolution dynamic SPECT imager,” *IEEE Transactions on Nuclear Science*, vol. 51, no. 3, pp. 631–635, June 2004.

[15] B. Miller, L. Furenlid, S. Moore, H. Bradford Barber, V. Nagarkar, and H. Barrett, “System integration of FastSPECT III, a dedicated SPECT rodent-brain imager based on BazookaSPECT detector technology,” in *IEEE NSS/MIC Conference Record*, Oct 2009, pp. 4004–4008.

[16] F. J. Beekman, F. van der Have, B. Vastenhouw, A. J. A. van der Linden, P. P. van Rijk, J. P. H. Burbach, and M. P. Smidt, “U-SPECT-I: A novel system for submillimeter-resolution tomography with radiolabeled molecules in mice,” *The Journal of Nuclear Medicine*, vol. 46, no. 7, pp. 1194–1200, Jul. 2005.

[17] F. van der Have, B. Vastenhouw, R. M. Ramakers, W. Branderhorst, J. O. Krah, C. Ji, S. G. Staelens, and F. J. Beekman, “U-SPECT-II: An ultra-high-resolution device for molecular small-animal imaging,” *The Journal of Nuclear Medicine*, vol. 50, no. 4, pp. 599–605, Apr. 2009.

[18] R. Van Holen, B. Vandeghinste, K. Deprez, and S. Vandenberghe, “Design and performance of a compact and stationary microSPECT system,” *Medical Physics*, vol. 40, no. 11, pp. 112 501–1–112 501–11, Nov. 2013.

[19] T. Funk, D. L. Kirch, J. E. Koss, E. Botvinick, and B. H. Hasegawa, “A novel approach to multipinhole SPECT for myocardial perfusion imaging,” *The Journal of Nuclear Medicine*, vol. 47, no. 4, pp. 595–602, Apr. 2006.

[20] W. Chang, C. E. Ordonez, H. Liang, Y. Li, and J. Liu, “C-SPECT-A Clinical Cardiac SPECT/Tct Platform: Design Concepts and Performance Potential,” *IEEE Transactions on Nuclear Science*, vol. 56, no. 5, pp. 2659–2671, Oct 2009.

[21] J. Dey, “Improvement of performance of cardiac SPECT camera using curved detectors with pinholes,” *IEEE Transactions on Nuclear Science*, vol. 59, no. 2, pp. 334–347, Apr. 2012.

[22] W. P. M, S. A, and A. J, “Physical and clinical evaluation of high-resolution thyroid pinhole tomography,” *The Journal of Nuclear Medicine*, vol. 37, no. 12, pp. 2017–2020, Dec. 1996.

[23] T. Carlier, A. Oudoux, E. Mirallie, A. Seret, I. Daumy, C. Leux, C. Bodet-Milin, F. Kraeber-Bodere, , and C. Ansquer, “99mTc-MIBI pinhole SPECT in primary hyperparathyroidism: comparison with conventional SPECT, planar scintigraphy and ultrasonography,” *European Journal of Nuclear Medicine and Molecular Imaging*, vol. 35, no. 3, pp. 637–643, Mar. 2008.

[24] W. P. Klein, H. Barrett, I. W. Pang, D. D. Patton, M. M. Rogulski, J. Sain, and W. Smith, “FASTSPECT: electrical and mechanical design of a high-resolution dynamic SPECT imager,” in *IEEE NSS/MIC Conference Record*, vol. 2, 1995, pp. 931–933.

[25] M. C. Goorden, M. C. M. Rentmeester, and F. J. Beekman, “Theoretical analysis of full-ring multi-pinhole brain SPECT,” *Physics in Medicine and Biology*, vol. 54, no. 21, pp. 6593–6610, 2009.

[26] H. O. Anger, *Instrumentation in Nuclear Medicine.* Academic Press Inc., 1967, vol. 1, ch. Radioisotope Cameras, pp. 485–552.

[27] H. Wieczorek and A. Goedicke, “Analytical model for SPECT detector concepts,” *IEEE Transactions on Nuclear Science*, vol. 53, no. 3, pp. 1102–1112, June 2006.

[28] D. L. Gunther, *Emission Tomography: The Fundamentals of PET and SPECT.* Elsevier Academic Press, 2004, ch. Collimator design for nuclear medicine, pp. 153–168.

[29] S. C. Moore, K. Kouris, and I. Cullum, “Collimator design for single photon emission tomography,” *European Journal of Nuclear Medicine*, vol. 9, no. 2, pp. 138–150, Feb 1992.

[30] K. V. Audenhaege, R. V. Holen, S. Vandenberghe, C. Vanhove, S. D. Metzler, and S. C. Moore, “Review of SPECT collimator selection, optimization, and fabrication for clinical and preclinical imaging,” *Medical Physics*, vol. 42, no. 8, pp. 4796–4813, Aug. 2015.

[31] O. V. Makarova, G. Yang, P. T. Amstutz, and C.-M. Tang, “Fabrication of antiscatter grids and collimators for X-ray and gamma-ray imaging by lithography and electroforming,” *Microsystem Technologies*, vol. 14, no. 9, pp. 1613–1619, Jan. 2008.

[32] A. V. Ochon, L. Ploux, R. Mastrippolito, Y. Charon, P. Laniece, L. Pinot, and L. Valentin, “An original emission tomograph for in vivo brain imaging of small animals,” in *IEEE NSS/MIC Conference Record*, 1996, pp. 1325–1329.

[33] K. Deprez, S. Vandenberghe, K. Van Audenhaege, J. Van Vaerenbergh, and R. Van Holen, “Rapid additive manufacturing of MR compatible multipinhole collimators with selective laser melting of tungsten powder,” *Medical Physics*, vol. 40, no. 1, pp. 012 501–1–012 501–11, Jan. 2013.

[34] K. Deprez, S. Vandenberghe, and R. Van Holen, “Accuracy and density of pure tungsten collimators produced by additive manufacturing,” *Journal of Nuclear Medicine*, vol. 54, no. Supplement 2, p. 2165, 2013.

[35] K. Van Audenhaege, S. Vandenberghe, K. Deprez, B. Vandeghinste, and R. Van Holen, “Design and simulation of a full-ring multi-lofthole collimator for brain spect,” *Physics in Medicine and Biology*, vol. 58, no. 18, pp. 6317–6336, Sep. 2013.

[36] K. Van Audenhaege, R. Van Holen, C. Vanhove, and S. Vandenberghe, “Collimator design for a multipinhole brain spect insert for mri,” *Medical Physics*, vol. 42, no. 11, pp. 6679–6689, 2015.

[37] K. Deprez, L. R. V. Pato, S. Vandenberghe, and R. Van Holen, “Characterization of a SPECT pinhole collimator for optimal detector usage (the lofthole),” *Physics in Medicine and Biology*, vol. 58, no. 4, pp. 859–885, Jan. 2013.

[38] S. Matej and R. Lewitt, “Practical considerations for 3-d image reconstruction using spherically symmetric volume elements,” *IEEE*

Transactions on Medical Imaging, vol. 15, no. 1, pp. 68–78, Feb 1996.

[39] A. Yendiki and J. A. Fessler, "A comparison of rotation- and blob-based system models for 3d spect with depth-dependent detector response," *Physics in Medicine and Biology*, vol. 49, no. 11, pp. 2157–2168, May 2004.

[40] P. P. Bruyant, "Analytic and iterative reconstruction algorithms in spect," *The Journal of Nuclear Medicine*, vol. 43, no. 10, pp. 1343–1358, Oct 2002.

[41] M. S. Wernick and J. N. Aarsvold, *Emission Tomography: The Fundamentals of PET and SPECT.* Elsevier Academic Press, 2004.

[42] J. Radon, "Uber die Bestimmung von Funktionen durch ihre Integralwerte langs gewisser Mannigfaltigkeiten," *Berichte Sashsische Akadamie der Wissenschaffen, Leipez, Math-Phys. K1.*, vol. 69, pp. 262–277, Jan. 1917.

[43] A. J. Rockmore and A. Macovski, "A maximum likelihood approach to emission image reconstruction from projections," *IEEE Transactions on Nuclear Science*, vol. 23, no. 4, pp. 1428–1432, Aug 1976.

[44] D. F. Yu and J. A. Fessler, "Mean and variance of single photon counting with deadtime," *Physics in Medicine and Biology*, vol. 45, no. 7, pp. 2043–2056, Jul. 2000.

[45] S. L. A and V. Y, "Maximum likelihood reconstruction for emission tomography," *IEEE Transactions on Medical Imaging*, vol. 1, no. 2, pp. 113–122, Oct. 1982.

[46] K. Lange and R. Carson, "EM reconstruction algorithms for emission and transmission tomography," *Journal of Computer Assisted Tomography*, vol. 8, no. 2, pp. 306–316, Apr. 1984.

[47] H. H. Barrett, D. W. Wilson, and B. M. W. Tsui, "Noise properties of the em algorithm. i. theory," *Physics in Medicine and Biology*, vol. 39, no. 5, pp. 833–846, May 1994.

[48] D. W. Wilson, B. M. W. Tsui, and H. H. Barrett, "Noise properties of the em algorithm. ii. monte carlo simulations," *Physics in Medicine and Biology*, vol. 39, no. 5, pp. 847–872, 1994.

[49] E. Veklerov and J. Llacer, “Stopping rule for the mle algorithm based on statistical hypothesis testing,” *IEEE Transactions on Medical Imaging*, vol. 6, no. 4, pp. 313–319, Dec 1987.

[50] T. J. Herbert, “Statistical stopping criteria for iterative maximum likelihood reconstruction of emission images,” *Physics in Medicine and Biology*, vol. 35, no. 9, pp. 1221–1232, Sep. 1990.

[51] F. J. Beekman, E. T. P. Slijpen, and W. J. Niessen, “Selection of task-dependent diffusion filters for the post-processing of spect images,” *Physics in Medicine and Biology*, vol. 43, no. 6, pp. 1713–1730, Jun. 1998.

[52] E. T. P. Slijpen and F. J. Beekman, “Comparison of post-filtering and filtering between iterations for spect reconstruction,” *IEEE Transactions on Nuclear Science*, vol. 46, no. 6, pp. 2233–2238, Dec 1999.

[53] P. J. Green, “Bayesian reconstructions from emission tomography data using a modified EM algorithm,” *IEEE Transactions on Medical Imaging*, vol. 9, no. 1, pp. 84–93, Mar. 1990.

[54] S. Geman and D. E. McClure, “Bayesian image analysis: An application to single photon emission tomography,” in *Proceedings of the American Statistical Association. Statistical Computing Section*, 1985, pp. 12–18.

[55] T. Hebert and R. Leahy, “A generalized em algorithm for 3-d bayesian reconstruction from poisson data using gibbs priors,” *IEEE Transactions on Medical Imaging*, vol. 8, no. 2, pp. 194–202, Jun 1989.

[56] K. Lange, “Convergence of em image reconstruction algorithms with gibbs smoothing,” *IEEE Transactions on Medical Imaging*, vol. 9, no. 4, pp. 439–446, Dec 1990.

[57] J. A. Fessler and W. L. Rogers, “Spatial resolution properties of penalized-likelihood image reconstruction: Space-invariant tomographs,” *IEEE Transactions on Image Processing*, vol. 5, no. 9, pp. 1346–1358, Sep. 1996.

[58] J. W. Stayman and J. A. Fessler, “Regularization for uniform spatial resolution properties in penalized-likelihood image reconstruc-

tion," *IEEE Transactions on Medical Imaging*, vol. 19, no. 6, pp. 601–615, Jun. 2000.

[59] B. M. W. Tsui, E. C. Frey, X. Zhao, D. S. Lalush, R. E. Johnston, and W. H. McCartney, "The importance and implementation of accurate 3d compensation methods for quantitative spect," *Physics in Medicine and Biology*, vol. 39, no. 3, pp. 509–530, Mar. 1994.

[60] J. Qi and R. H. Huesman, "Effect of Errors in the System Matrix on MAP Image Reconstruction," *Physics in Medicine and Biology*, vol. 50, no. 14, pp. 3297–3312, Jul. 2005.

[61] T. M. Peters, "Algorithms for fast back- and re-projection in computed tomography," *IEEE Transactions on Nuclear Science*, vol. 28, no. 4, pp. 3641–3647, Aug 1981.

[62] P. M. Joseph, "An improved algorithm for reprojecting rays through pixel images," *IEEE Transactions on Medical Imaging*, vol. 1, no. 3, pp. 192–196, Nov 1982.

[63] R. L. Siddon, "Fast calculation of the exact radiological path for a three-dimensional ct array," *Medical Physics*, vol. 12, no. 2, 1985.

[64] B. De Man and S. Basu, "Distance-driven projection and backprojection," in *IEEE NSS/MIC Conference Record*, 2002, pp. 1477–1480.

[65] B. D. Man and S. Basu, "Distance-driven projection and backprojection in three dimensions," *Physics in Medicine and Biology*, vol. 49, no. 11, pp. 2463–2475, Jun. 2004.

[66] Y. Long, J. A. Fessler, and J. M. Balter, "3d forward and backprojection for x-ray ct using separable footprints," *IEEE Transactions on Medical Imaging*, vol. 29, no. 11, pp. 1839–1850, Nov 2010.

[67] A. Ihsani and T. Farncombe, "An adaptation of the distance driven projection method for single pinhole collimators in spect imaging," *IEEE Transactions on Nuclear Science*, vol. 63, no. 1, pp. 140–150, Feb 2016.

[68] I. Laurette, G. L. Zeng, A. Welch, P. E. Christian, and G. T. Gullberg, "A three-dimensional ray-driven attenuation, scatter and

geometric response correction technique for SPECT in inhomogeneous media," *Physics in Medicine and Biology*, vol. 45, no. 11, pp. 3459–3480, Nov. 2000.

[69] C. Vanhove, A. Andreyev, M. Defrise, J. Nuyts, and A. Bossuyt, "Resolution recovery in pinhole SPECT based on multi-ray projections: a phantom study," *European Journal of Nuclear Medicine and Molecular Imaging*, vol. 34, no. 2, pp. 170–180, Feb. 2007.

[70] G. K. Loudos, "An efficient analytical calculation of probability matrix in 2D SPECT," *Computerized Medical Imaging and Graphics*, vol. 32, no. 2, pp. 83–94, Mar. 2008.

[71] F. Boisson, V. Bekaert, A. Reilhac, J. Wurtz, and D. Brasse, "Assessment of a fast generated analytical matrix for rotating slat collimation iterative reconstruction: a possible method to optimize the collimation profile," *Physics in Medicine and Biology*, vol. 60, no. 6, pp. 2403–2419, Mar. 2015.

[72] W. M. C. Foulkes, L. Mitas, R. J. Needs, and G. Rajagopal, "Quantum monte carlo simulations of solids," *Rev. Mod. Phys.*, vol. 73, pp. 33–83, Jan 2001.

[73] A. Rambaut and N. C. Grass, "Seq-gen: an application for the monte carlo simulation of dna sequence evolution along phylogenetic trees," *Computer applications in the biosciences : CABIOS*, vol. 13, no. 3, pp. 235–238, 1997.

[74] I. R. Abubakirov and A. A. Gusev, "Estimation of scattering properties of lithosphere of kamchatka based on monte-carlo simulation of record envelope of a near earthquake," *Physics of the Earth and Planetary Interiors*, vol. 64, no. 1, pp. 52–67, 1990.

[75] H. Zaidi, "Relevance of accurate monte carlo modeling in nuclear medical imaging," *Medical Physics*, vol. 26, no. 4, pp. 574–608, 1999.

[76] J. W. Beck, R. J. Jaszczak, R. E. Coleman, C. F. Starmer, and L. W. Nolte, "Analysis of spect including scatter and attenuation using sophisticated monte carlo modeling methods," *IEEE Transactions on Nuclear Science*, vol. 29, no. 1, pp. 506–511, Feb 1982.

[77] C. E. Floyd, R. J. Jaszczak, C. C. Harris, and R. E. Coleman, "Energy and spatial distribution of multiple order compton scatter

in spect: a monte carlo investigation," *Physics in Medicine and Biology*, vol. 29, no. 10, p. 1217, 1984.

[78] M. Ljungberg and S.-E. Strand, "A monte carlo program for the simulation of scintillation camera characteristics," *Computer Methods and Programs in Biomedicine*, vol. 29, no. 4, pp. 257 – 272, 1989.

[79] D. Lazaro, V. Breton, and I. Buvat, "Feasibility and value of fully 3D Monte Carlo reconstruction in single-photon emission computed tomography," *Nuclear Instruments and Methods in Physics Research Section A*, vol. 527, no. 1, pp. 195–200, Jul. 2004.

[80] D. Lazaro, Z. El Bitar, V. Breton, D. Hill, and I. Buvat, "Fully 3D Monte Carlo reconstruction in SPECT: a feasibility study," *Physics in Medicine and Biology*, vol. 50, no. 16, pp. 3739–3754, Aug. 2005.

[81] Z. El Bitar, D. Lazaro, C. Coello, V. Breton, D. Hill, and I. Buvat, "Fully 3D Monte Carlo image reconstruction in SPECT using functional regions," *Nuclear Instruments and Methods in Physics Research Section A*, vol. 569, no. 2, pp. 399–403, Dec. 2006.

[82] S. Jan, G. Santin, D. Strul, S. Staelens, K. Assie, D. Autret, S. Avner, R. Barbier, M. Bardies, P. M. Bloomfield, D. Brasse, V. Breton, P. Bruyndonckx, I. Buvat, A. F. Chatziioannou, Y. Choi, Y. H. Chung, C. Comtat, D. Donnarieix, L. Ferrer, S. J. Glick, C. J. Groiselle, D. Guez, P.-F. Honore, S. Kerhoas-Cavata, A. S. Kirov, V. Kohli, M. Koole, M. Krieguer, D. J. van der Laan, F. Lamare, G. Largeron, C. Lartizien, D. Lazaro, M. C. Maas, L. Maigne, F. Mayet, F. Melot, C. Merheb, E. Pennacchio, J. Perez, U. Pietrzyk, F. R. Rannou, M. Rey, D. R. Schaart, C. R. Schmidtlein, L. Simon, T. Y. Song, J.-M. Vieira, D. Visvikis, R. V. de Walle, E. Wieers, and C. Morel, "Gate: a simulation toolkit for PET and SPECT," *Physics in Medicine and Biology*, vol. 49, no. 19, pp. 4543–4561, Sep. 2004.

[83] S. Agostinelli, J. Allison, K. Amako, J. Apostolakis, H. Araujo, P. Arce, M. Asai, D. Axen, S. Banerjee, G. Barrand, F. Behner, L. Bellagamba, J. Boudreau, L. Broglia, A. Brunengo, H. Burkhardt, S. Chauvie, J. Chuma, R. Chytracek, G. Cooperman, G. Cosmo, P. Degtyarenko, A. Dell'Acqua, G. Depaola,

D. Dietrich, R. Enami, A. Feliciello, C. Ferguson, H. Fesefeldt, G. Folger, F. Foppiano, A. Forti, S. Garelli, S. Giani, R. Giannitrapani, D. Gibin, J. G. Cadenas, I. Gonzalez, G. G. Abril, G. Greeniaus, W. Greiner, V. Grichine, A. Grossheim, S. Guatelli, P. Gumplinger, R. Hamatsu, K. Hashimoto, H. Hasui, A. Heikkinen, A. Howard, V. Ivanchenko, A. Johnson, F. Jones, J. Kallenbach, N. Kanaya, M. Kawabata, Y. Kawabata, M. Kawaguti, S. Kelner, P. Kent, A. Kimura, T. Kodama, R. Kokoulin, M. Kossov, H. Kurashige, E. Lamanna, T. LampÃ©n, V. Lara, V. Lefebure, F. Lei, M. Liendl, W. Lockman, F. Longo, S. Magni, M. Maire, E. Medernach, K. Minamimoto, P. M. de Freitas, Y. Morita, K. Murakami, M. Nagamatu, R. Nartallo, P. Nieminen, T. Nishimura, K. Ohtsubo, M. Okamura, S. O'Neale, Y. Oohata, K. Paech, J. Perl, A. Pfeiffer, M. Pia, F. Ranjard, A. Rybin, S. Sadilov, E. D. Salvo, G. Santin, T. Sasaki, N. Savvas, Y. Sawada, S. Scherer, S. Sei, V. Sirotenko, D. Smith, N. Starkov, H. Stoecker, J. Sulkimo, M. Takahata, S. Tanaka, E. Tcherniaev, E. S. Tehrani, M. Tropeano, P. Truscott, H. Uno, L. Urban, P. Urban, M. Verderi, A. Walkden, W. Wander, H. Weber, J. Wellisch, T. Wenaus, D. Williams, D. Wright, T. Yamada, H. Yoshida, and D. Zschiesche, "Geant4-a simulation toolkit," *Nuclear Instruments and Methods in Physics Research Section A: Accelerators, Spectrometers, Detectors and Associated Equipment*, vol. 506, no. 3, pp. 250–303, 2003.

[84] B. F. Hutton, I. Buvat, and F. J. Beekman, "Review and current status of spect scatter correction," *Physics in Medicine and Biology*, vol. 56, no. 14, p. R85, 2011.

[85] F. van der Have, B. Vastenhouw, M. Rentmeester, and F. J. Beekman, "System calibration and statistical image reconstruction for ultra-high resolution stationary pinhole spect," *IEEE Transactions on Medical Imaging*, vol. 27, no. 7, pp. 960–971, July 2008.

[86] Z. Liu, G. A. Kastis, G. D. Stevenson, H. H. Barrett, L. R. Furenlid, M. A. Kupinski, D. D. Patton, and D. W. Wilson, "Quantitative analysis of acute myocardial Infarct in rat hearts with ischemia-reperfusion using a high-resolution stationary SPECT system," *The Journal of Nuclear Medicine*, vol. 43, no. 7, pp. 933–939, Jul. 2002.

[87] Y.-C. Chen, L. R. Furenlid, D. W. Wilson, and H. H. Barrett,

"Calibration of Scintillation Cameras and Pinhole SPECT Imaging Systems," *Small-Animal SPECT Imaging*, pp. 195–201, 2005.

[88] J. Y. Hesterman, M. A. Kupinski, L. R. Furenlid, D. W. Wilson, and H. H. Barrett, "The multi-module, multi-resolution system (m3r): A novel small-animal spect system," *Medical Physics*, vol. 34, no. 3, pp. 987–993, 2007.

[89] F. van der Have, B. Vastenhouw, M. Rentmeester, and F. J. Beekman, "System calibration and statistical image reconstruction for sub-mm stationary pinhole SPECT," in *IEEE NSS/MIC Conference Record*, vol. 5, 2005, pp. 2653–2657.

[90] J. A. Fessler, "Mean and variance of implicitly defined biased estimators (such as penalized maximum likelihood): Applications to tomography," *IEEE Transactions on Image Processing*, vol. 5, no. 3, pp. 493–506, Jan. 1996.

[91] D. Gunter, K. Matthews, and C. Ordonez, "The optimal design of non-parallel hole collimators," in *IEEE Nuclear Science Symposium, Conference Record*, vol. 3, 1999, pp. 1344–1348 vol.3.

[92] M. F. Smith, S. Majewski, and A. G. Weisenberger, "Optimizing pinhole and parallel hole collimation for scintimammography with compact pixellated detectors," *IEEE Transactions on Nuclear Science*, vol. 50, no. 3, pp. 321–326, Jun 2003.

[93] R. M. Capote, N. Matela, R. C. ConceiÃ§Ã£o, and P. Almeida, "Optimization of convergent collimators for pixelated spect systems," *Medical Physics*, vol. 40, no. 6, pp. 62 501–1–062 501–13, 2013.

[94] M. C. M. Rentmeester, F. van der Have, and F. J. Beekman, "Optimizing multi-pinhole spect geometries using an analytical model," *Physics in Medicine and Biology*, vol. 52, no. 9, pp. 2567–2581, 2007.

[95] P. Nillius and M. Danielsson, "Theoretical bounds and system design for multipinhole spect," *IEEE Transactions on Medical Imaging*, vol. 29, no. 7, pp. 1390–1400, July 2010.

[96] H. H. Barrett, "Objective assessment of image quality: effects of quantum noise and object variability," *Journal of the Optical Society of America A*, vol. 7, no. 7, pp. 1266–1278, Jul 1990.

[97] H. H. Barrett, J. L. Denny, R. F. Wagner, and K. J. Myers, "Objective assessment of image quality. II. Fisher information, Fourier crosstalk, and figures of merit for task performance," *Journal of the Optical Society of America A*, vol. 12, no. 5, pp. 834–852, May 1995.

[98] H. H. Barrett, C. K. Abbey, and E. Clarkson, "Objective assessment of image quality. III. ROC metrics, ideal observers, and likelihood-generating functions," *Journal of the Optical Society of America A*, vol. 15, no. 6, pp. 1520–1535, Jun 1998.

[99] H. H. Barrett, K. J. Myers, N. Devaney, and C. Dainty, "Objective assessment of image quality. IV. Application to adaptive optics," *Journal of the Optical Society of America A*, vol. 23, no. 12, pp. 3080–3105, Dec 2006.

[100] M. A. Kupinski and E. Clarkson, "Objective Assessment of Image Quality," *Small-Animal SPECT Imaging*, pp. 101–114, 2005.

[101] H. H. Barrett, J. Yao, J. P. Rolland, and K. J. Myers, "Model observers for assessment of image quality," in *Proceedings of the National Academy of Sciences of the United States of America*, vol. 90, no. 21, 1993, pp. 9758–9765.

[102] H. H. Barrett and K. J. Myers, *Foundations of image science.* Wiley-VCH, 2003.

[103] R. E. Carson, Y. Yan, B. Chodkowski, T. K. Yap, and M. E. Daube-Witherspoon, "Precision and accuracy of regional radioactivity quantitation using the maximum likelihood em reconstruction algorithm," *IEEE Transactions on Medical Imaging*, vol. 13, no. 3, pp. 526–537, Sep 1994.

[104] K. Vunckx, D. Beque, M. Defrise, and J. Nuyts, "Single and multipinhole collimator design evaluation method for small animal SPECT," *IEEE Transactions on Medical Imaging*, vol. 27, no. 1, pp. 36–46, Jan. 2008.

[105] H. H. Barrett and W. Swindell, *Radiological Imaging: The Theory of Image Formation, Detection, and Processing*, revised ed. Academic Press, Sep. 1996.

[106] S. Shokouhi, S. D. Metzler, D. W. Wilson, and T. E. Peterson, "Multi-pinhole collimator design for small-object imaging with SiliSPECT: a high-resolution SPECT," *Physics in Medicine and Biology*, vol. 54, no. 2, pp. 207–225, Jan. 2009.

[107] K. Deprez, R. V. Holen, and S. Vandenberghe, "The lofthole: A novel shaped pinhole geometry for optimal detector usage without multiplexing and without additional shielding," in *IEEE NSS/MIC Conference Record*, 2011.

[108] K. Deprez, R. Van Holen, and S. Vandenberghe, "A high resolution SPECT detector based on thin continuous LYSO," *Physics in Medicine and Biology*, vol. 59, no. 1, pp. 153–171, Jan. 2014.

[109] L. R. V. Pato, R. Van Holen, K. Deprez, and S. Vandenberghe, "Geometric sensitivity in the penumbra region of a pinhole: analytic calculation," *Journal of Nuclear Medicine*, vol. 53, no. suppl. 1, May 2012.

[110] L. R. V. Pato, S. Vandenberghe, T. Zedda, and R. Van Holen, "Parallel-hole collimator concept for stationary SPECT imaging," *Physics in Medicine and Biology*, vol. 60, no. 22, pp. 8791–8807, Nov. 2015.

[111] L. R. V. Pato, S. Vandenberghe, P. L. Esquinas, and R. Van Holen, "Analytical modeling of collimator response for a compact stationary parallel-hole spect system," in *Proceedings of the 13th International Meeting on Fully Three-Dimensional Image Reconstruction in Radiology and Nuclear Medicine*, 2015.

[112] J. A. Fessler and S. D. Booth, "Conjugate-gradient preconditioning methods for shift-variant PET image reconstruction," *IEEE Transactions on Image Processing*, vol. 8, no. 5, pp. 688–699, May 1999.

[113] J. Qi and R. M. Leahy, "Resolution and noise properties of MAP reconstruction for fully 3-D PET," *IEEE Transactions on Medical Imaging*, vol. 19, no. 5, pp. 493–506, May 2000.

[114] L.-J. Meng and D. K. Wehe, "Feasibility study of using hybrid collimation for nuclear environmental imaging," *IEEE Transactions on Nuclear Science*, vol. 50, no. 4, pp. 1103–1110, Aug. 2003.

[115] L.-J. Meng, W. L. Rogers, N. H. Clinthorne, and J. A. Fessler, “Feasibility study of compton scattering enchanced multiple pinhole imager for nuclear medicine,” *IEEE Transactions on Nuclear Science*, vol. 50, no. 5, pp. 1609–1617, Oct. 2003.

[116] J. W. Stayman and J. A. Fessler, “Efficient calculation of resolution and covariance for penalized-likelihood reconstruction in fully 3-D SPECT,” *IEEE Transactions on Medical Imaging*, vol. 23, no. 12, pp. 1543–1556, Dec. 2004.

[117] L.-J. Meng and N. Li, “Non-uniform object-space pixelation (NUOP) for penalized maximum-likelihood image reconstruction for a single photon emission microscope system,” *IEEE Transactions on Nuclear Science*, vol. 56, no. 5, pp. 2777–2788, Oct. 2009.

[118] N. Li and L.-J. Meng, “Adaptive angular sampling for SPECT imaging,” *IEEE Transactions on Nuclear Science*, vol. 58, no. 5, pp. 2205–2218, Oct. 2011.

[119] N. Fuin, S. Pedemonte, S. Arridge, S. Ourselin, and B. F. Hutton, “Efficient determination of the uncertainty for the optimization of SPECT system design: A subsampled Fisher information matrix,” *IEEE Transactions on Medical Imaging*, vol. 33, no. 3, pp. 618–635, Mar. 2014.

[120] J. Nuyts, K. Vunckx, M. Defrise, and C. Vanhove, “Small animal imaging with multi-pinhole SPECT,” *Methods*, vol. 48, no. 2, pp. 83–91, Jun. 2009.

[121] A. M. Catafau, “Brain SPECT in clinical practice. part I: Perfusion*,” *Journal of Nuclear Medicine*, vol. 42, no. 2, pp. 259–271, Feb 2001.

[122] K. Vunckx, D. Beque, M. Defrise, and J. Nuyts, “Single and multipinhole collimator design evaluation method for small animal SPECT,” in *IEEE NSS/MIC Conference Record*, 2005, pp. 2223–2227.

[123] L. Zhou, M. Defrise, K. Vunckx, and J. Nuyts, “Comparison between parallel hole and rotating slat collimation: Analytical noise propagation models,” *IEEE Transactions on Medical Imaging*, vol. 29, no. 12, pp. 2038–2052, Dec 2010.

[124] D. Paix, “Pinhole imaging of gamma rays,” *Physics in Medicine and Biology*, vol. 12, no. 4, pp. 489–500, Oct. 1967.

[125] W. P. Segars, B. M. W. Tsui, E. C. Frey, G. A. Johnson, and S. S. Berr, “Development of a 4-D digital mouse phantom for molecular imaging research,” *Molecular Imaging & Biology*, vol. 6, no. 3, pp. 149–59, May 2004.

[126] L. R. V. Pato, S. Vandenberghe, B. Vandeghinste, and R. Van Holen, “Evaluation of the local shift-invariance approximation in pinhole SPECT,” in *IEEE NSS/MIC Conference Record*, 2013.

[127] K. Vunckx, P. Suetens, and J. Nuyts, “Effect of overlapping projections on reconstruction image quality in multipinhole SPECT,” *IEEE Transactions on Medical Imaging*, vol. 27, no. 7, pp. 972–83, Jul. 2008.

[128] L. Zhou, K. Vunckx, and J. Nuyts, “Predicting the variance of ML reconstructions with body contour constraint for multi-pinhole SPECT,” in *IEEE NSS/MIC Conference Record*, 2010, pp. 2376–2380.

[129] J. Lin, “On artifact-free projection overlaps in multi-pinhole tomographic imaging,” *IEEE Transactions on Medical Imaging*, vol. 32, no. 12, pp. 2215–2229, Dec. 2013.

[130] L. R. V. Pato, S. Vandenberghe, B. Vandeghinste, and R. Van Holen, “Evaluation of Fisher information matrix approximation-based methods for fast assessment of image quality in pinhole SPECT,” *IEEE Transactions on Medical Imaging*, vol. 34, no. 9, pp. 1830–1842, Sep. 2015.

[131] L. R. V. Pato, B. Vandeghinste, S. Vandenberghe, and R. Van Holen, *Small-Animal SPECT Imaging (in press)*. Springer Science + Business Media, New York, NY, ch. Fast Evaluation of Image Quality and Bed Position Optimization in Small-Animal Multi-Pinhole SPECT.

[132] L. R. V. Pato, S. Vandenberghe, and R. Van Holen, “Efficient optimization for adaptive SPECT systems based on local shift-invariance,” in *IEEE NSS/MIC Conference Record*, 2012, pp. 2501–2508.

[133] ——, “Efficient optimization based on local shift-invariance for adaptive SPECT systems,” in *Abstracts of the Workshop on Small-Animal SPECT Imaging*, 2012.

[134] X.-C. Lai and L.-J. Meng, “Artificial compound-eye gamma camera for mri compatible spect imaging,” in *IEEE NSS/MIC Conference Record*, 2013.

[135] V. Y. Panin, A. M. Smith, J. Hu, F. Kehren, and M. E. Casey, “Continuous bed motion on clinical scanner: design, data correction, and reconstruction,” *Physics in Medicine and Biology*, vol. 59, no. 20, pp. 6153–6174, Oct. 2014.

[136] F. Zito, A. Savi, and F. Fazio, “CERASPECT: a brain-dedicated SPECT system. performance evaluation and comparison with the rotating gamma camera,” *Physics in Medicine and Biology*, vol. 38, no. 10, pp. 1433–1442, Oct. 1993.

[137] W. P. Segars and B. M. W. Tsui, “MCAT to XCAT: The Evolution of 4-D Computerized Phantoms for Imaging Research,” in *IEEE NSS/MIC Conference Record*, 2009, pp. 1954–1968.

[138] W. Brenner, K. H. Bohuslavizki, N. Sieweke, S. Tinnemeyer, M. Clausen, and E. Henze, “Quantification of diphosphonate uptake based on conventional bone scanning,” *European Journal of Nuclear Medicine*, vol. 24, no. 10, pp. 1284–1290, Oct 1997.

[139] W. Branderhorst, F. van der Have, B. Vastenhouw *et al.*, “Murine cardiac images obtained with focusing pinhole SPECT are barely influenced by extra-cardiac activity,” *Physics in Medicine and Biology*, vol. 57, no. 3, pp. 717–732, Feb. 2012.

[140] L. R. V. Pato, S. Vandenberghe, and R. Van Holen, “Stationary SPECT imaging,” *Patent Application*, no. PCT/EP2015/066710, Jul. 2015.

[141] R. Maddula, R. Clackdoyle, J. Roberts, E. Di Bella, and Z. Fu, “Dynamic cardiac SPECT imaging using a stationary SPECT camera,” in *IEEE NSS/MIC Conference Record*, vol. 5, Oct 2004, pp. 3165–3169.

[142] J. Xu, C. Liu, Y. Wang, E. C. Frey, and B. M. W. Tsui, “Quantitative rotating multisegment slant-hole SPECT mammography

with attenuation and collimator-detector response compensation," *IEEE Transactions on Medical Imaging*, vol. 26, no. 7, pp. 906–916, Jul. 2007.

[143] J. Ouyang, G. E. Fakhri, W. Xia, M. F. Kijewski, and S. Genna, "The design and manufacture of an annular variable-focusing collimator for high sensitivity brain SPECT," *IEEE Transactions on Nuclear Science*, vol. 53, no. 5, pp. 2613–2618, Oct. 2006.

[144] D. W. Wilson, H. H. Barrett, and E. W. Clarkson, "Reconstruction of two- and three-dimensional images from synthetic-collimator data," *IEEE Transactions on Medical Imaging*, vol. 19, no. 5, pp. 412–422, May 2000.

[145] B. S. McDonald, S. Shokouhi, H. H. Barrett, and T. E. Peterson, "Multi-energy, single-isotope imaging using stacked detectors," *Nuclear Instruments and Methods in Physics Research Section A*, vol. 579, no. 1, pp. 196–199, Aug. 2007.

[146] K. Deprez, S. Vandenberghe, B. Vandeghinste, and R. V. Holen, "FlexiSPECT: A SPECT system consisting of a compact high-resolution scintillation detector (SPECTatress) and a lofthole collimator," *IEEE Transactions on Nuclear Science*, vol. 60, no. 1, pp. 53–64, Feb. 2013.

[147] K. Deprez, *Preclinical SPECT imaging based on compact collimators and high resolution scintillation detectors.* PhD Dissertation, Ghent University, 2014.

[148] K. Deprez, R. V. Holen, S. Vandenberghe, and S. Staelens, "Design of a high resolution scintillator based SPECT detector (SPECTatress)," *Nuclear Instruments And Methods in Physics Research Section A - Accelerators Spectrometers Detectors and Associated Equipment*, vol. 648, no. suppl. 1, pp. S107–S110, Jan. 2011.

[149] C. Bouckaert, S. Vandenberghe, and R. V. Holen, "Evaluation of a compact, high-resolution SPECT detector based on digital silicon photomultipliers," *Physics in Medicine and Biology*, vol. 59, no. 23, pp. 7521–7539, Nov. 2014.

[150] "MOLECUBES," http://molecubes.com.

[151] S. Amano, T. Inoue, K. Tomiyoshi, T. Ando, and K. Endo, "In Vivo Comparison of PET and SPECT Radiopharmaceuticals

in Detecting Breast Cancer," *The Journal of Nuclear Medicine*, vol. 39, no. 8, pp. 1424–1427, Aug. 1998.

[152] L. R. V. Pato, S. Vandenberghe, K. Van Audenhaege, and R. Van Holen, "Design and simulation of a stationary SPECT imaging system based on axially varying tilted parallel-hole collimation," in *IEEE NSS/MIC Abstract*, 2014.

List of Publications

A1 Journal Papers

1. L. R. V. Pato, S. Vandenberghe, T. Zedda, and R. Van Holen, "Parallel-hole collimator concept for stationary SPECT imaging," *Physics in Medicine and Biology*, vol. 60, no. 22, pp. 8791–8807, Nov. 2015.
2. L. R. V. Pato, S. Vandenberghe, B. Vandeghinste, and R. Van Holen, "Evaluation of Fisher information matrix approximation-based methods for fast assessment of image quality in pinhole SPECT," *IEEE Transactions on Medical Imaging*, vol. 34, no. 9, pp. 1830–1842, Sept. 2015.
3. K. Deprez, L. R. V. Pato, S. Vandenberghe, and R. Van Holen, "Characterization of a SPECT pinhole collimator for optimal detector usage (the lofthole)," *Physics in Medicine and Biology*, vol. 58, no. 4, pp. 859–885, Jan. 2013.

Patent Applications

1. L. R. V. Pato, S. Vandenberghe, and R. Van Holen, "Stationary SPECT imaging," filing date July 22nd 2015, App. nr. PCT/EP2015/066710.

Book Chapters

1. L. R. V. Pato, B. Vandeghinste, S. Vandenberghe, and R. Van Holen, "Fast Evaluation of Image Quality and Bed Position Optimization in Small-Animal Multi-Pinhole SPECT," in *Small-*

Animal SPECT Imaging (in press), M. Kupinski and L. Furenlid (Eds.), Springer Science + Business Media, New York, NY.

Conference Proceedings

1. L. R. V. Pato, S. Vandenberghe, P. L. Esquinas, and R. Van Holen, “Analytical modeling of collimator response for a compact stationary parallel-hole SPECT system,” in *Proceedings of the 13th International Meeting on Fully Three-Dimensional Image Reconstruction in Radiology and Nuclear Medicine*, 2015.
2. L. R. V. Pato, S. Vandenberghe, B. Vandeghinste, and R. Van Holen, “Evaluation of the local shift-invariance approximation in pinhole SPECT,” in *IEEE NSS/MIC Conference Record*, 2013.
3. L. R. V. Pato, S. Vandenberghe, and R. Van Holen, “Efficient optimization based on local shift-invariance for adaptive SPECT systems,” in *IEEE NSS/MIC Conference Record*, 2012.

Conference Abstracts

1. L. R. V. Pato, S. Vandenberghe, K. Van Audenhaege, and R. Van Holen, “Design and simulation of a stationary SPECT imaging system based on axially varying tilted parallel-hole collimation,” in *IEEE NSS/MIC Conference Abstracts*, 2014.
2. L. R. V. Pato, S. Vandenberghe, and R. Van Holen, “Efficient optimization based on local shift-invariance for adaptive SPECT systems,” in *Workshop on Small-Animal SPECT Imaging*, 2012.
3. L. R. V. Pato, R. Van Holen, K. Deprez, and S. Vandenberghe, “Geometric sensitivity in the Penumbra region of a pinhole: analytic calculation,” in *Journal of Nuclear Medicine*, vol. 53, suppl. 1, 2012.
4. L. R. V. Pato, R. Van Holen, and S. Vandenberghe, “Adaptive SPECT: personalizing medical imaging,” in *13th FEA PhD Symposium*, 2012.
5. L. R. V. Pato, R. Van Holen, and S. Vandenberghe, “Adaptive SPECT: personalizing medical imaging,” in *11th National Day on Biomedical Engineering*, 2012.